

1 **The Mars Science Laboratory *Curiosity* Rover Mast Camera**
2 **(Mastcam) Instruments: Pre-Flight and In-Flight**
3 **Calibration, Validation, and Data Archiving**

4
5 **J.F. Bell III¹, A. Godber¹, S. McNair², M.A. Caplinger², J.N. Maki³,**
6 **M.T. Lemmon⁴, J. Van Beek², M.C. Malin², D. Wellington¹, K.M. Kinch⁵,**
7 **M.B. Madsen⁵, C. Hardgrove¹, M.A. Ravine², E. Jensen², D. Harker²,**
8 **R.B. Anderson⁶, K.E. Herkenhoff⁶, R.V. Morris⁷, E. Cisneros¹, and R.G. Deen³**

9
10 ¹School of Earth and Space Exploration, Arizona State University, Tempe AZ

11 ²Malin Space Science Systems, Inc., San Diego, CA

12 ³Jet Propulsion Laboratory, California Institute of Technology, Pasadena, CA

13 ⁴Texas A&M University, College Station, TX

14 ⁵Niels Bohr Institute, Univ. of Copenhagen, Copenhagen, Denmark

15 ⁶USGS Astrogeology Science Center, Flagstaff, AZ

16 ⁷NASA/Johnson Space Center, Houston, TX

17

18 Submitted to the AGU journal *Earth and Space Science*, 23 September 2016.

19 Revised 21 May 2017.

20

21 Keywords: Mars; Multispectral imaging; Calibration; Curiosity rover; Gale crater

ABSTRACT

22
23

24 The NASA *Curiosity* rover Mastcam system is a pair of fixed-focal length, multispectral,
25 color CCD imagers mounted ~2 m above the surface on the rover's remote sensing mast, along
26 with associated electronics and an onboard calibration target. The left Mastcam (M-34) has a 34-
27 mm focal length, an IFOV of 0.22 mrad, and a FOV of $20^\circ \times 15^\circ$ over the full 1648×1200 pixel
28 span of its Kodak KAI-2020 CCD. The right Mastcam (M-100) has a 100-mm focal length, an
29 IFOV of 0.074 mrad, and a FOV of $6.8^\circ \times 5.1^\circ$ using the same detector. The cameras are
30 separated by 24.2 cm on the mast, allowing stereo images to be obtained at the resolution of the
31 M-34 camera. Each camera has an 8-position filter wheel, enabling it to take Bayer pattern RGB
32 "true color" images, multispectral images in nine additional bands spanning ~400-1100 nm, and
33 images of the Sun in two colors through neutral-density-coated filters. An associated Digital
34 Electronics Assembly provides command and data interfaces to the rover, 8 GBytes of image
35 storage per camera, 11-bit to 8-bit companding, JPEG compression, and acquisition of high-
36 definition video. Here we describe the pre-flight and in-flight calibration of Mastcam images, the
37 ways that they are being archived in the NASA Planetary Data System, and the ways that
38 calibration refinements are being developed as the investigation progresses on Mars. We also
39 provide some examples of data sets and analyses that help to validate the accuracy and precision
40 of the calibration.

41

42 **Table of Contents**

43	ABSTRACT	2
44	1. Introduction	5
45	2. Brief Instrument Description	6
46	2.1. Cameras	6
47	2.2. Mastcam Calibration Target	8
48	2.3. Integration with the Rover	8
49	3. Pre-flight Camera Testing and Calibration: Methods, Data Sets, and Results.....	9
50	3.1. Introduction and Philosophy	9
51	3.2. Pre-flight Instrument-Level Testing	10
52	3.2.1. CCD Characterization	10
53	3.2.2. Bias and Dark Current Characterization.....	10
54	3.2.3. Electronic Shutter Smear.....	12
55	3.2.4. System Spectral Throughput.....	13
56	3.2.5. Pixel-to-Pixel Responsivity ("Flatfield") Characterization	15
57	3.2.6. Radiometric Responsivity	16
58	3.2.7. Pre-flight Focus Calibration.....	18
59	3.2.8. Geometric performance and resolution	18
60	3.2.9. Stray and scattered light testing.....	20
61	3.2.10. Bad Pixels and/or Particulates on the Detectors.....	20
62	3.2.11. Geologic Samples and Color/Reflectance Standards Imaging	21
63	3.3. Pre-flight Geometric/Camera Model Testing and Validation	21
64	3.3.1. Four-vector MSSS-produced CAHV camera model	22
65	3.3.2. JPL-produced CAHVOR camera model	25
66	3.3.3. Pointing the JPL camera model.....	26
67	4. In-Flight/Surface Calibration and Validation: Methods, Data Sets, and Results.....	27
68	4.1. Cruise	27
69	4.2. Special In-Flight Calibration and Testing on Mars.....	27
70	4.2.1. In-Flight Bias and Dark Current Testing.....	27
71	4.2.2. In-Flight Electronic Shutter Smear Characterization.....	28
72	4.2.3. Improved Flatfields from In-Flight Sky Measurements	29
73	4.2.4. Validation & Improvement of Radiance Calibration from In-Flight Sky Measurements..	32
74	4.2.5. Focus Testing/Performance.....	34
75	4.2.6. Compression Testing/Performance.....	36
76	4.2.7. In-Flight Scattered Light Testing.....	37
77	4.3. Mastcam Calibration Target Imaging	38
78	5. Data Reduction, Validation, and Archiving.....	39
79	5.1. Introduction and Methodology.....	39
80	5.2. Initial (Tactical) Data Reduction and Calibration Pipeline	40
81	5.2.1. Decompression	40
82	5.2.2. Companding and Decompanding	41
83	5.2.3. Dark Current Modeling and Removal.....	42
84	5.2.4. Electronic Shutter Removal.....	44
85	5.2.5. Flatfielding	44
86	5.2.6. Correction of Dead/Bad Pixels.....	45
87	5.2.7. Initial Radiometric Calibration	45

88	5.2.8. Color Correction.....	46
89	5.2.9. Geometric Linearization for Mosaicking and Map Projection.....	47
90	5.3. Enhancements to the Initial Mastcam Data Reduction and Calibration Pipeline.	48
91	5.3.1. Improved Bayer pattern decompression/interpolation methods.....	48
92	5.3.2. Correction of Saturated or Hot/Bad Pixels.....	49
93	5.3.3. Improved Electronic Shutter Smear Removal.....	50
94	5.3.4. Improved Flatfielding.....	51
95	5.3.5. Improved Radiance Calibration.....	51
96	5.3.6. Enhanced Radiance Factor (I/F) Calibration using the Mastcam Calibration Target.....	51
97	5.4. Examples: Accuracy and Precision of the Calibration.	54
98	5.4.1. Example Morphologic Observations: Effects of Focus and Compression.....	54
99	5.4.2. Example Stereo Products.....	55
100	5.4.3. Sky/Astronomical Imaging Examples.....	55
101	5.4.4. Quantitative Radiance Factor Multispectral Observations.....	56
102	5.5. Data Products and PDS Archiving.....	57
103	6. Future Work and Lessons Learned.....	58
104	7. Summary	59
105	8. Acknowledgements.....	60
106	9. Appendix A: Camera Model Transformations	61
107	10. Appendix B: MSL/Mastcam Standard Companding (11 to 8 bit DN) and	
108	Decompanying (8 to 11 bit DN) "Lookup Table 0".	64
109	11. Appendix C: Committee on Data Management and Computation (CODMAC, 1982)	
110	Processing Levels, and their traditional NASA equivalents.....	65
111	12. Appendix D: Mastcam Archived PDS Data File Names.....	66
112	13. References.....	67
113	14. Tables.....	76
114	15. Figures and Captions.	86
115		
116		

117 **1. Introduction**

118 The Mast Camera (Mastcam) instrument on the NASA Mars Science Laboratory (MSL) rover
119 *Curiosity* consists of a pair of focusable digital CCD cameras (detectors, optics, and filter
120 wheels) that can acquire multispectral (400-1000 nm), stereoscopic images of the Martian
121 surface and atmosphere at two specific fixed focal lengths. An externally-mounted calibration
122 target enables the relative reflectance calibration of the images and two electronics boards in the
123 rover body enable data processing and transmission of images to the rover's central computer.
124 The cameras are mounted atop a 2-meter tall mast that enables them to be rotated 360° in
125 azimuth and ±90° in elevation.

126 The primary objective of the Mastcam investigation is to characterize and determine details of
127 the history and processes recorded in geologic material at the MSL landing site within Gale
128 crater, particularly as they pertain to habitability. Gale is a ~154 km diameter ancient impact
129 crater centered near 5.4°S, 137.8°E, along the topographic dichotomy between the heavily
130 cratered southern highlands and the lower, younger northern plains. A major goal of the mission
131 is to explore evidence for past habitability within Aeolis Mons, the ~5 km tall central mound of
132 layered sedimentary rocks (informally called "Mt. Sharp") within Gale.

133 Mastcam instrument characteristics and observational strategies have been designed to
134 address the following six specific objectives: (1) Observe Landscape Physiography and
135 Processes; (2) Examine the Properties of Rocks; (3) Study the Properties of Fines; (4) View Frost,
136 Ice, and Related Processes; (5) Document Atmospheric and Meteorologic Events and Processes;
137 and (6) Support/Facilitate Rover Operations, Analytical Laboratory Sampling, Contact
138 Instrument Science, and Other MSL Science. *Curiosity* was launched in November 2011 and
139 landed in Gale on 6 August, 2012. As of this writing, the rover has traversed more than 15 km
140 from the landing site to the base of Mt. Sharp over ~1500 Martian days (sols), and Mastcam
141 images have played an important role in actively enabling the MSL team to make exciting
142 discoveries about the habitability of ancient Mars (*e.g.*, Williams *et al.*, 2013; Grotzinger *et al.*,
143 2014).

144 Here we describe the series of pre-flight component-level, standalone camera-level, and
145 integrated rover-level tests and calibration activities and analyses that were performed with the
146 Mastcams in order to enable raw Mars images to be geometrically and radiometrically calibrated
147 after being downlinked to Earth. We also describe standard procedures and special

148 tests/observations that have been performed with the cameras on Mars in order to validate the
149 pre-flight calibrations, to monitor for potential changes in the calibrations over time, and to
150 enable additional calibration of the data to relative reflectance, for more direct comparisons to
151 laboratory reflectance spectra of rocks and minerals. More details about the Mastcam instrument,
152 and the Mastcam science investigation in general, can be found in Malin *et al.* (2010, 2017) and
153 Bell *et al.* (2012, 2013), and more details about the general goals of the *Curiosity* mission, plus
154 the goals of other payload instruments also carried by the rover, can be found in Grotzinger *et al.*
155 (2012).

156 **2. Brief Instrument Description**

157 **2.1. Cameras.**

158 Mastcam (Figure 1; Malin *et al.*, 2017) consists of two focusable color cameras mounted on
159 the rover's Remote Sensing Mast (RSM). The two cameras have different focal lengths and
160 different sets of narrowband science filters (Tables 1 and 2). The cameras use the Kodak KAI-
161 2020 CCD (7.4 μm square pixel pitch, with a microlens on each pixel) to acquire images of up to
162 1648 \times 1200 pixels (including dark columns), and are capable of relatively high frame rate
163 acquisitions ("video" up to about 4 frames/sec). The cameras acquire color via Bayer pattern
164 filters on the CCD (Figure 2), but also have selectable science filters that image through the
165 Bayer-pattern filters (Figure 3). Characteristics of the Mastcam optics useful in the calibration
166 and analysis of data products are described in Table 1.

167 Each Mastcam camera images through an 8-position filter wheel, actuated by an Aeroflex
168 (now Cobham) stepper motor. One of the positions in each filter wheel (Table 2) is a broadband
169 infrared cutoff filter for use with the Bayer broadband RGB color capability of the CCD, at filter
170 position "0". Bayer RGB imaging across the entire sensor was included in order to provide a
171 simple way to include color information as an additional component of assessing the general
172 geologic context of the scene. Twelve of the sixteen other filter positions provide multispectral
173 imaging capability at nine unique additional wavelengths spanning \sim 400 to 1100 nm, and
174 including 3 filters shared by each camera (Table 2). Most multispectral images are acquired
175 using the central 1200 \times 1200 pixel "science imaging" area of the CCD (Figure 2). Additionally,
176 two filters (one on each camera) with neutral density coatings provide direct solar imaging
177 capability in two colors. The spectral bandwidths described in Table 2 are based on the system-

178 level monochromator measurements described in §3.2.4 below.

179 The left "eye" of the Mastcam uses an 8-element, focusable, 34-mm effective focal length
180 (EFL) lens that provides images with an angular instantaneous field of view (IFOV) of 218
181 $\mu\text{rad}/\text{pixel}$. The right "eye" uses a 9-element focusable 100-mm EFL lens that provides an IFOV
182 of 74 $\mu\text{rad}/\text{pixel}$. Both cameras have an outer sapphire window that provides protection from
183 dust. Using internal lens triplets that can be actuated over a small range of motion ($\sim \pm 1$ mm,
184 also using Aeroflex stepper motors), the M-34 and M-100 cameras can acquire in-focus images
185 from a range of ~ 0.4 and ~ 1.6 meters from the sapphire window to infinity, respectively.
186 Additional details about the Mastcam optics design, fabrication, and performance can be found
187 in Ghaemi (2009).

188 Each camera also relies on a Digital Electronics Assembly (DEA) which contains DC-DC
189 converters, DRAM memory for temporary image storage and flash memory (8 GBytes/camera)
190 for non-volatile storage, communications interfaces, and a Field Programmable Gate Array
191 (FPGA) with an embedded processor that runs the flight software which implements Mastcam
192 commands. The DEA provides power and data interfaces to the camera's CCD image sensor and
193 its support circuitry, and includes motor drivers for the optomechanical system (focus and filter
194 wheel motion).

195 The Mastcam DEAs provide a high level of flexibility for operational acquisition and return to
196 Earth of raw, compressed, or small "thumbnail" images. Compression can be performed within
197 the DEA to process data using both lossless predictive difference and lossy discrete cosine
198 transform (JPEG) compression, the latter using either 4:2:2 or 4:4:4 chroma subsampling or
199 grayscale sampling of luminance only (*e.g.*, Malin *et al.*, 2013). The DEA's large flash memories
200 permit each camera to acquire and store many images and internal flight software and hardware
201 permit images to be processed both into and out of the flash memory. Although generalized
202 down-sampling, sometimes also called sub-sampling or pixel summing, cannot be performed
203 (*e.g.*, the Mastcams cannot acquire summed images, which would be lower resolution but
204 smaller in size), small thumbnails that are 1/8th the linear dimensions and 1/64th the data volume
205 can be generated from the initial, full-sized images. The various types of "raw" and processed
206 images that can be generated by the Mastcams are described in Table 3. For additional details on
207 the processing of full size and thumbnail JPEG images as well as factors concerning their
208 operational use, see Malin *et al.* (2013, 2017).

209 **2.2. Mastcam Calibration Target.**

210 Mastcam includes an 8×8 cm wide, 6 cm tall, external color calibration target, mounted on the
211 top of the Rover Pyro Firing Assembly (RPFA) box on the rover's deck, designed to enable
212 imaging of a reference set of color and grayscale materials of known spectral reflectances and
213 photometric properties (Figure 4). The target provides a way to validate the instrument's
214 radiometric calibration, as well as a way to enable tactical-timescale calibration of the radiance
215 images to relative reflectance or Lambert albedo. The shadow cast by a central post (gnomon)
216 provides a way to assess the direct versus diffuse components of solar and sky irradiance
217 incident on the target.

218 The target flown on MSL is a modified flight spare of the Pancam calibration target flown on
219 the Mars Exploration Rovers (MER) *Spirit* and *Opportunity* (Bell *et al.*, 2003; 2006). One
220 science-related modification to the Mastcam cal target was to embed six "sweep magnets"
221 (Madsen *et al.*, 2003; Bertelsen *et al.*, 2004) approximately 1 mm under the surface of the color
222 chips and two of the grayscale rings, to enable small parts of the target to remain relatively dust-
223 free. A second set of modifications included changes in the target's function as an education and
224 public outreach sundial (*e.g.*, Bell & Sullivan, 2004). Specifically, the dial's motto, fabrication
225 date, and side-panel message were all modified for MSL compared to MER (Figure 4). Other
226 E/PO aspects of the target's design remain the same as for MER. Details of the reflectance and
227 photometric properties of the target materials can be found in Bell *et al.* (2003; 2006).

228 **2.3. Integration with the Rover.**

229 The Mastcam cameras are mounted on the RSM at a height of 1.97 m above the Martian
230 surface. The left and right cameras are separated by 24.2 cm, and they are positioned
231 symmetrically relative to an azimuth actuation axis that is located on the front right corner of the
232 rover, 559 mm starboard of the vehicle's center line. Elevation actuation of both cameras occurs
233 along an axis that is located 64.6 mm below the camera boresights, or 1.91 m above the surface.

234 When the cameras are pointed at the Mastcam calibration target (rover frame azimuth of
235 189.2° and 176.2° for the M-34 and M-100 cameras, respectively, with 0° azimuth corresponding
236 to straight in front of the rover; rover frame elevation of -32.4° downward from horizontal), the
237 base of the gnomon is ~1.2 m from the front sapphire windows of the Mastcam optics. This
238 placement is too close to be in good focus for the M-100 camera, but the larger number of pixels
239 on the target's calibration surfaces adequately compensates for the blurred nature of those images

240 and does not compromise the use of the target as a relative calibration source for M-100 images.
241

242 **3. Pre-flight Camera Testing and Calibration: Methods, Data** 243 **Sets, and Results**

244 **3.1. Introduction and Philosophy.**

245 The primary goals of Mastcam pre-flight testing and calibration were to develop a detailed
246 understanding of the performance of the cameras under a range of environmental conditions
247 relevant to Mars; to validate pre-assembly predictions of instrument performance so that models
248 could be constructed to interpolate or extrapolate expected performance on Mars to conditions
249 where pre-flight testing was not possible; and to acquire data sufficient to enable the conversion
250 of measured Data Number (DN) values on Mars to an accurate estimate of radiance-on-sensor, in
251 physical units such as $W/m^2/nm/sr$.

252 To that end, a series of tests were run at the instrument level (standalone assembled 34-mm
253 and 100-mm flight camera systems driven by Ground Support Equipment (GSE) designed to
254 simulate their respective DEAs), as well as some tests at the system level (cameras mounted to
255 the rover in their flight configuration), to characterize the cameras' radiometric and geometric
256 properties. These tests included characterization of the electronic and noise properties of each
257 CCD detector, the spectral throughput of the system, the level of pixel-to-pixel responsivity
258 ("flatfield") variations, the absolute radiometric responsivity, focus performance, geometric
259 performance and image quality, and stray and scattered light assessment. Where appropriate,
260 data were obtained through all of the wide- and narrow-band multispectral filters in both cameras.
261 Here we describe the detailed nature of those pre-flight tests as well as the results derived from
262 them. Those results, along with additional results from tests conducted in flight (§4), are then
263 used as part of the Mastcam data reduction and calibration pipeline discussed in §5.

264 Raw Mastcam Experiment Data Records (EDRs) and radiance-calibrated Reduced Data
265 Records (RDRs) have been being archived to the NASA Planetary Data System (PDS) since the
266 beginning of the MSL mission in August 2012 (see <http://pds-imaging.jpl.nasa.gov/data/msl> and
267 §5.5). Those currently-archived RDRs, created using the data sets and methods described here
268 and in the PDS archive itself (Caplinger, 2013), should be considered to be "Version 1" Mastcam
269 RDR data products, produced primarily for tactical decision-making and quicklook science

270 analyses. Refinements to the Version 1 Mastcam calibration, many of which are described here,
271 can in many cases improve the fidelity of the radiance calibration and/or allow the data to be
272 further calibrated to greater accuracy to radiance factor or to estimated Lambert albedo. We are
273 working to archive in the PDS all of these further-refined "Version 2" Mastcam RDR data
274 products. However, the information, data, and algorithms presented here are intended to allow
275 individual Mastcam data users to perform these and other higher-fidelity calibrations themselves
276 starting from the original PDS-archived EDRs, should that be necessary for their particular
277 scientific goals.

278 **3.2. Pre-flight Instrument-Level Testing.**

279 **3.2.1. CCD Characterization.**

280 We characterized the gain (electrons, e^- , per DN), read noise (e^-), and full well capacity (e^-) of
281 the Mastcam signal chain by imaging a diffuse illuminated integrating sphere target and by
282 subsequent analysis of photon transfer curves using the technique described by Janesick *et al.*
283 (1987). Like many CCD imaging systems, the Mastcams use correlated double sampling to
284 measure the small difference in voltage between a reference ("reset") and scene ("video") signal.
285 Reset and video signals are read separately as 12-bit data values which are then subtracted. The
286 resulting difference is encoded as an 11-bit (DN = 0-2047) output signal. Uncompressed 11-bit
287 image data were acquired at room temperature in a cleanroom laboratory setting on 30 July 2009.
288 We obtained pairs of images at exposure durations of 0, 5, 10, 20, and 50 msec at sphere lamp
289 currents of 0, 6, 7, and 8 amps. The photon transfer curve is shown in Figure 5, and the results
290 for gain, read noise, and full well are listed in Table 1. Figure 6 demonstrates the linear response
291 of the Mastcam detectors, over the range from zero signal up to ~90% full well, based on images
292 of a diffusely-illuminated constant radiance integrating sphere target acquired at room
293 temperature in a cleanroom laboratory setting on 17 August 2009. Operationally, manual and/or
294 automatic exposure times (the latter using the autoexposure algorithm described in Maki *et al.*,
295 2003, which is the same algorithm as used on the Mars Hand Lens Imager (MAHLI) camera; see
296 §7.3.2 in Edgett *et al.*, 2012) are selected to avoid signal levels above the known linear range. In
297 post-processing of Version 2 calibrated RDRs, raw EDR signal levels above ~1800 DN (240 DN
298 when companded to 8-bit data; see §5.3.2) are flagged as having a non-linear response.

299 **3.2.2. Bias and Dark Current Characterization.**

300 We characterized the rate of accumulation of dark current (charge generated in the CCD from

301 thermal background effects) as a function of temperature during pre-flight testing. The Mastcam
 302 camera heads were designed to operate on Mars over an allowable flight temperature (AFT)
 303 range of -55°C to +50°C, and the Mastcam DEAs over an AFT range of -40°C to +50°C. Figure
 304 7 shows the actual range of flight temperatures experienced by the M-34 Mastcam during the
 305 first ~1000 sols of Curiosity's mission on Mars. Maximum CCD temperatures experienced in
 306 flight are around +12°C and maximum DEA temperatures are around +40°C.

307 Thermal vacuum tests were conducted during pre-flight testing in July 2009 to characterize
 308 the bias signal (from the DEAs) and dark current signal (from the CCDs) over a range of
 309 approximately -60°C to +60°C. Figure 8 shows the pre-flight data that were collected and
 310 analyzed to create the following models for the background bias + dark current levels for each of
 311 the cameras:

312

$$313 \quad M-34: DN_{back} = [t_{exp} \cdot 2.9e^{0.08T}] + 121.5 \quad (1) \text{ and}$$

$$314 \quad M-100: DN_{back} = [t_{exp} \cdot 2.5e^{0.08T}] + 122.0 \quad (2),$$

315

316 where T is the reported or inferred focal plane array (CCD) temperature for each camera,
 317 in °C, and t_{exp} is the exposure time of the image, in sec.

318 The bias level alone, estimated from zero second exposure images, exhibits only a slowly-
 319 varying DC offset of about 120±5 DN over the range of temperatures relevant to Mastcam
 320 operations (Figure 8). Inside the camera electronics, the value of this background signal is a
 321 commandable parameter, and is subtracted from all pixels in the image during the 11-bit to 8-bit
 322 companding process. The commanded background level is reported in the
 323 DARK_LEVEL_CORRECTION processing parameter keyword in the PDS archived image
 324 label for each Mastcam image, and is usually set to 117 DN during flight operations on Mars.

325 Additionally, Figure 8 shows that dark current is not significant at the tested exposure time of
 326 1000 msec below about 20°C. Since Mastcam FPA temperatures in flight have not exceeded
 327 +12°C, and exposure times rarely exceed 1000 msec (most exceptions being longer exposures
 328 specifically designed to characterize dark current in flight or for long and very cold night-time
 329 exposures; see §5.4.3), dark current accumulation can almost always effectively be ignored in
 330 processing and calibration of Mastcam images.

331 3.2.3. Electronic Shutter Smear.

332 The Mastcam CCD sensor is a progressive scan, interline transfer device (*e.g.*, Howell, 2000;
333 Truesense, 2012). Charge from the photosensitive area of each pixel is transferred into an
334 adjacent vertical (aligned along CCD columns) light-shielded shift register. Those charges are
335 then clocked down, one CCD line (row) at a time, into a horizontal shift register, from which
336 each pixel is then clocked out of the device horizontally for subsequent digitization. While the
337 shift of charge from the photosensitive pixels into the vertical shift registers is essentially
338 instantaneous (μ secs) and simultaneous for all pixels, clocking of the measured charges down
339 into the horizontal register and out of the device takes significantly more time.

340 For the Mastcam CCDs, the system clock rate is typically set to 20 MHz, and the readout time
341 for a full frame 1648 \times 1200 pixel image is about 420 msec. Mastcam does not have a mechanical
342 shutter, and thus during the readout a small amount of incident light leakage into the vertical
343 shift registers can occur. However, the sensitivity of the vertical registers is between 5,600 to
344 10,000 times (75-80 dB) lower than the sensitivity of each pixel's photosites (Eastman Kodak,
345 2009; ON Semiconductor, 2014; 2015), and thus the leaked signal is very small. Regardless, this
346 light leakage still introduces an excess signal into the data, called electronic shutter smear
347 because the excess charge is "smeared" down the array as it is being clocked out, producing dim
348 vertical bands extending below bright features in the scene. The magnitude of this smear is
349 proportional to the scene intensity in each pixel, and thus the smear image mimics the scene
350 image, but at a much fainter level and with a superimposed linear ramp of charge added, since
351 photosensitive pixels farthest from the horizontal shift register (which is at the "bottom" of the
352 array) accumulate charge during the readout longer than those at the top (*e.g.*, Bell *et al.*, 2003).
353 A complication in cameras like the Mastcams is that the sensitivity of each pixel in each line
354 varies because the Bayer filters impose an additional wavelength-dependent pattern onto each
355 image (*e.g.*, Figure 2; see also discussion in Edgett *et al.*, 2015).

356 The amount of smear signal in a given image is proportional to the ratio of the frame readout
357 time to the exposure time. For example, for typical Mastcam exposure times of 10 msec and for
358 scenes without signal levels over the sensor's full well, the worst-case electronic shutter smear
359 level for pixels farthest from the horizontal register (which take the full 420 msec to read out)
360 and with vertical shift registers 75 dB less sensitive than the pixel's photosites would be $[(420$
361 msec / 10 msec) / 5,600] = 0.75% of the scene signal, or at most about 15 DN for a signal near

362 full well. Given that most Mastcam images are commanded to have average signal levels only
363 near half to three-fourths full well, electronic shutter smear is not expected to be a significant
364 effect. The smear percentage increases, however, as the exposure time becomes shorter or if the
365 scene contains very bright features (such as the sun glinting off rover structure). In such
366 instances it might be desirable to remove the smear signature. For a static scene, this can easily
367 be done by computing a running sum of the signal level across each column and subtracting the
368 appropriate fraction of it from each pixel.

369 It should be noted that shutter smear in the Mastcam interline transfer CCDs is different from
370 the shutter smear observed in frame transfer CCD imagers like the MER/Pancam system. As
371 described in Bell *et al.* (2003), frame transfer in the Pancams is a much simpler situation (and a
372 much larger effect). In-flight testing and other aspects of electronic shutter smear assessment and
373 potential removal for the Mastcams are discussed in §4.2.2 and §5.3.3 below.

374 3.2.4. System Spectral Throughput.

375 Each Mastcam camera is equipped with an 8-position filter wheel, positioned close to each
376 camera's CCD (Figure 1; Table 2). Filter 0 (wide band near-IR cutoff filter) on each camera is
377 used for direct Bayer RGB imaging, and Filter 7 is equipped with a neutral density coating that
378 enables direct solar imaging in one of two colors (near-IR 880 nm for the M-34, and blue 440 nm
379 for the M-100). During pre-flight calibration on 17-19 August 2009, the system-level throughput
380 (CCD + Bayer filter + optics + filter wheel filter) was characterized for each filter wheel and
381 Bayer filter combination by acquiring images of the output slit of a monochromator operated
382 under ambient room temperature conditions at Malin Space Science Systems (MSSS) in San
383 Diego. For both the M-100 and M-34 cameras, calibration runs consisted of monochromator
384 sweeps from 300-1100 nm at 10 nm steps, and subsequent 100 nm sweeps at 5 nm steps centered
385 around each filter's effective center wavelength. For Filters L0 and R0, the 5 nm sweeps covered
386 400 nm of wavelength space from 400-800 nm. Monochromator test data were not acquired for
387 Filters L7 and R7 because it was not possible to create a bright enough monochromatic source to
388 detect through the neutral density 5 coatings on those solar filters. Instead, estimates for the
389 system-level passbands of those filters were derived from component-level and/or vendor-
390 supplied test data. Each output image contains a 1648×96 pixel array subsampled from near the
391 center of the full array, and the image of the monochromator slit was consistently centered in the
392 array for each calibration run.

393 Post-processing of the data was conducted to characterize each filter's bandpass, estimating
394 the effective center wavelength and filter width from the peak-normalized average of the
395 monochromator slit image signal as a function of wavelength. Effective center wavelength is
396 defined as the wavelength where the total integral under the bandpass curve (defined as the area
397 of the curve above the level of 1% of the peak maximum value) gets to half its total value. Filter
398 width is defined as half the width of the bandpass curve at half of the normalized peak maximum
399 value (Half-Width at Half-Maximum; HWHM). Data were extracted from sets of individual Red
400 (R), Green1 (G1), Green2 (G2), and Blue (B) Bayer pixels (Figure 2) in each monochromator slit
401 image. For Filters L0 and R0, the R, G1, G2, and B curves were analyzed separately, treating
402 them effectively as separate filters (although parameters for the G1 and G2 pixels were
403 statistically the same, and so the average parameters for the two green pixels are plotted and
404 reported here). For filters L5-L7 and R4-R6 (all of which have effective band centers > 800 nm),
405 the Bayer filter pattern is effectively transparent (Figure 3), and so all pixels were included in the
406 calculation statistics. For filters where the narrowband filter partially or completely blocks one or
407 more of the Bayer responses (shaded cells in Table 2), only one specific Bayer pixel was used for
408 the statistics: R for filters L3, L4, and R3; the average of G1 and G2 for filters L1 and R1, and B
409 for filters L2, R2, and R7. A similar process is employed with Mastcam images in filters L1-L4
410 and R1, R2, and R7 in lossy-compressed images downlinked from Mars: kernels are applied
411 within the flight software that completely discard pixels whose Bayer peak is outside the
412 narrowband filter bandpass, using only the same specific Bayer pixels listed above (see §5.2.1).
413 Derived normalized bandpass profiles for the Mastcam filters using these methods are plotted in
414 Figure 3, and bandpass characteristics are listed in Table 2.

415 Monochromator scan images acquired through the narrowband blue filters L2 and R2 (band
416 centers near 445 nm) suffered from low signal to noise ratio (SNR) compared to the other filters
417 because of the relatively weak signal level of the calibrated light source at that wavelength, and
418 thus the long integration times (and thus higher background levels) required. The acquired data
419 for the narrowband blue filters also revealed a much higher level of relatively constant 500-1100
420 nm rejection band "leakage" for these filters – up to 21% and 9% of the in-band response levels
421 for L2 and R2, respectively (compared to rejection band responses of 1-4% for the other filters).
422 The low SNR of the L2 and R2 data, however, yield high uncertainties on those out-of-band

423 leakage levels. The end result, as discussed in §3.2.6 below, is a much higher level of
424 radiometric uncertainty for the L2 and R2 filters compared to the other filters.

425 We did not perform any corrections for the spectral radiance of the monochromator's
426 illumination source, nor did we calculate an "expected correction" for the shape of the Sun's
427 radiance spectrum, which is the illumination source on Mars. Given the relatively narrow
428 passbands of most of the Mastcam filters, these spectral corrections could be expected to
429 introduce only small (several percent) shifts in the effective band centers estimated here. Given
430 the fact that most of the mineralogic spectral features reasonably expected to be encountered
431 with Mastcam at Gale crater are broad, solid state absorptions (*e.g.*, Bell *et al.*, 2003; Rice *et al.*,
432 2010), such small potential shifts in estimated effective center wavelengths or band widths are
433 not expected to have any significant effect on scientific analyses.

434 3.2.5. Pixel-to-Pixel Responsivity ("Flatfield") Characterization.

435 Variations in pixel-to-pixel responsivity in imaging systems can be characterized by acquiring
436 images of so-called "flat" (uniformly illuminated) targets. Observed non-uniformities in the
437 resulting images result from variations induced by optics, filters, dust, and/or intrinsic variations
438 in the radiometric responses of individual pixels. Normalized "flatfield" images quantitatively
439 characterize the combined magnitude of these non-uniformities and can be used to remove most
440 of their effects on imaging data.

441 During pre-flight camera testing at MSSS on 31 July and 6 and 8 August 2009, both
442 Mastcams imaged the uniformly-illuminated exit port of a Spectralon-coated integrating sphere
443 under ambient room temperature and pressure conditions. Images were acquired through all of
444 the Mastcam filters except the L7 and R7 solar filters (which could not be adequately
445 illuminated). Dark images were also obtained with the sphere exit port blocked, in order to
446 characterize background signal levels in the sphere image data. To avoid any potential
447 nonuniformity effects associated with the edges of the sphere's exit port, both cameras acquired
448 1648×512 pixel images at three elevation positions that enabled the bottom, middle, and top third
449 of the field of view to be centered in the sphere's exit port. The images were later combined into
450 single full-field 1600×1200 pixel flatfield images. Example flatfield image for filter R0 in both
451 cameras are shown in Figure 9.

452 Post-processing of the flat-field calibration data included visual and quantitative inspection to
453 assess data quality, subtraction of the background dark images, combination of the images from

454 the top, middle, and bottoms of the fields of view, de-Bayering the data to work with separate R,
455 G1, G2, and B channel data, and calculating image statistics from the central region of each
456 image to normalize each final flatfield image to a mean value of 1.0. Maximum flatfield
457 variations detected in the images were approximately $\pm 10\%$, dominated by variations near the
458 edges of the field where the circular Mastcam filters begin to vignette the CCD's rectangular
459 field of view (Figure 9). Typical variations near the center of the fields of view, and especially
460 within the 1200x1200 pixel region defined as the nominal science imaging area of each Mastcam,
461 are less than $\pm 1\%$. This is why multispectral imaging sequences, which require more robust
462 quantitative calibration than geologically-focused RGB imaging, are typically restricted to the
463 science imaging area of the CCD.

464 Initial flatfield files currently being used for the rapid tactical calibration of images and initial
465 PDS release versions of the data are archived with the PDS (see §5.2.5). Further refined and
466 processed versions of the normalized Mastcam flatfield images for both cameras and all filters
467 except the Solar ND filters (filter #7 in each camera) are being developed from in-flight
468 calibration measurements (see §4.2.3 and §5.3.4).

469 3.2.6. Radiometric Responsivity.

470 To produce spectral or true-color data products we need to characterize how the camera, filter,
471 and optics encode the scene radiance into the digital output for each possible camera and filter
472 combination. The combination of these properties can be represented by a single coefficient,
473 often known as the radiometric calibration coefficient (Table 4). Initial estimates of the
474 radiometric calibration coefficients (see Caplinger, 2013), which are being used currently in the
475 tactical "Version 1" calibration of images and initial PDS release versions of the data, were based
476 on a component-level model of the CCD quantum efficiency (QE), filter bandpass response, and
477 optics transmissivity, based on piece-part testing and vendor data. These initial estimates agree
478 very well with the more detailed estimates based on "Version 2" calibrated images obtained with
479 the actual flight cameras and the data processing methods described here.

480 During the summer of 2009, we imaged the exit port of the same integrating sphere described
481 in §3.2.5, after acquiring a NIST-certified radiometric calibration of the sphere's radiance as a
482 function of wavelength and input current. Using the sphere's 8 Amp setting, we acquired
483 multiple images of the radiance from the sphere in both Mastcams, under ambient room
484 temperature and pressure conditions. Each image was a 1648x512 pixel subframe taken from the

485 center of each camera's field of view at various exposure settings.

486 Post-processing included de-Bayering the input images into separate R, G1, G2, and B
487 images; calculating the mean value from a relatively uniform region within the image of the
488 sphere's exit port; subtracting the mean of a dark, unexposed region of each image in order to
489 remove any background bias + dark current signal; dividing the resulting background-corrected
490 DN values by the exposure time to arrive at an estimate of DN/sec; and then dividing the DN/sec
491 by the estimated radiance of the integrating sphere in each filter, derived by convolving the
492 NIST-certified sphere radiance with the system spectral response functions calculated in §3.2.4
493 (Figure 10). The standard deviation of the mean DN values extracted from the sphere images was
494 propagated through the calculations and combined with a conservative estimate of $\pm 10\%$
495 uncertainty on the sphere's calibrated radiance, based on NIST calibration of the monitoring
496 diode. The final radiometric coefficients, in units of $[(W/m^2/nm/sr) / (DN/s)]$, along with their
497 estimated uncertainties, are listed in Table 4. In almost all cases, the $\pm 10\%$ uncertainty in the
498 estimate of the sphere radiance dominates the radiometric uncertainty. However, for the
499 narrowband blue (L2 and R2) filters, additional uncertainties in the characterization of their
500 spectral throughput, discussed below, lead to much higher absolute calibration uncertainties than
501 for the other Mastcam filters (Table 4).

502 An estimate of the relative filter-to-filter uncertainty (a measure of the precision of normalized
503 "spectra" ultimately derived from Mastcam multispectral measurements) can be made by
504 dividing out the assumed absolute radiance spectrum of the calibration lamp in Figure 10, and
505 assessing the levels of the resulting filter-to-filter deviations. These relative filter precision
506 estimates are also listed in Table 2. The close similarity of typical Mastcam Mars surface relative
507 reflectance spectra derived from this calibration (*e.g.*, §5.4.4) to spectra acquired from previous
508 Mars surface missions over the same wavelengths indicates that these relative precision estimates
509 are likely to be overly conservative (especially for the narrowband blue filters L2 and R2).

510 Because of schedule constraints, it was not possible to acquire data to estimate the Mastcam
511 responsivity coefficients at more flight-like temperatures and pressures. However, we did
512 perform limited responsivity tests of a sample of KAI-2020 CCD sensors from the same lot as
513 the flight sensors, over temperatures down to -105°C . We did not notice any significant
514 variations that would be consistent with a large change in QE over that temperature range, which
515 is much wider than the range experienced by the CCDs on Mars (Figure 7). In addition,

516 experience with other Mars surface CCD imaging systems (*e.g.*, MER/Pancam; Bell *et al.*, 2003;
517 2006) as well as in-flight Mastcam radiance factor validation measurements (*e.g.*, §5.2.7, §5.4.4),
518 show that the effects of varying QE over temperature are likely small, and within the ~10%
519 overall estimated uncertainty of the Mastcam radiance estimates. The radiometric responsivities
520 of the G1 and G2 filters are the same within the uncertainties, and can be averaged in practice to
521 estimate an overall green responsivity. Filters with bandpasses common to both cameras also
522 exhibit comparable radiometric response coefficients (within $\pm 1\%$ to $\pm 7\%$, or within the
523 estimated $\pm 10\%$ typical absolute radiance uncertainties) after compensating for the cameras'
524 difference in focal ratios $[(f/8)^2 / (f/10)^2 = 0.64]$. As a further check on the relative accuracy of
525 these derived coefficients, we also found that the Mastcam coefficients in Table 4 for near-IR
526 wavelengths greater than 800 nm that are comparable to the wavelengths used for the
527 MER/Pancam filters (Bell *et al.*, 2003), are essentially the same as those derived for the Pancams
528 at room temperature, after compensating for differences in the focal ratios and CCD quantum
529 efficiencies among these imaging systems.

530 3.2.7. Pre-flight Focus Calibration.

531 While the M-34 and M-100 Mastcams are each fixed focal length cameras, they are *focusable*,
532 over a relatively wide range of focus distances (Table 1). Analysis of pre-flight Mastcam images
533 of a geometric calibration target (*e.g.*, Figure 11) were used to derive an initial calibration of the
534 focus of each camera as a function of distance. Those calibrations (Table 5; Caplinger, 2013) can
535 be used to make an initial estimate of distances to targets of interest (and thus the sizes of those
536 targets, using the known IFOV of each pixel; Table 1) and the FOCUS_POSITION_COUNT
537 keyword in the PDS labels of archived Mastcam images. That initial calibration has been
538 subsequently refined in flight to also include the effects of temperature on the focusing of the
539 cameras, as described in §4.2.5 below.

540 3.2.8. Geometric performance and resolution.

541 We acquired a small set of images of a standard geometric calibration target (the "SVG
542 Squares and Wedges pattern" target from Imatest, 2015; Figure 12) over several focus positions
543 and under ambient laboratory conditions at MSSS using the M-34 and M-100 flight cameras on
544 2009 August 17 and 20. We calculated the Modulation Transfer Function (MTF; also known as
545 the Spatial Frequency Response or SFR) using the freely-available Matlab code `sformat3` (Burns,
546 2015) on the images that appeared to be visually in best focus. The algorithm used in this

547 software follows the International Organization for Standardization (ISO) 12233 procedure for
548 measuring the resolution of electronic still cameras using the slanted edge method (Burns, 2000).
549 We defined rectangular regions of interest spanning five suitable slanted bright-dark edges on the
550 test chart (Imatest, 2015), primarily near the center half of the field of view. The raw images of
551 the targets were interpolated to remove the Bayer pattern, converting each image into separate
552 images of the red, green (Figure 12), and blue channels. Each single-band image was used as
553 input to the `sformat3` code to determine the MTF for each band separately. The MTFs for each of
554 the five regions were within about 10% of each other, and so they were averaged to obtain a
555 single, averaged MTF for each band in each camera. The detector pixel scale (7.4 μm per pixel)
556 was used to convert the MTF from units of line pairs per pixel (lp/pix) to line pairs per mm
557 (lp/mm).

558 Our analysis (Figure 13) reveals that the average (over the Bayer R, G, and B bands) MTF at
559 50% contrast occurs at a spatial frequency of 0.185 lp/pix for the M-34 camera, and 0.155 lp/pix
560 for the M-100 camera, corresponding to image scales of 5.4 and 6.4 pixels, respectively, for
561 these cameras. Differences between the R, G, and B Bayer bands are generally small and within
562 the noise of the analysis. For reference, Figure 13 also shows that the values of the MTF at
563 Nyquist for the M-34 and M-100 cameras are $\sim 6\%$ to $\sim 10\%$ and $\sim 4\%$ to $\sim 7\%$, respectively,
564 assuming "Nyquist" for a color Bayer imaging system is defined not as the standard 0.5 lp/pix of
565 monochrome imaging systems, but as $0.5(\sqrt{2}/2) = 0.35$ lp/pix (*e.g.*, Lensation, 2013). No
566 aliasing was observed.

567 Several important caveats apply to this analysis. First, because of strict time limits on the
568 testing of the flight Mastcams, imaging of the target at a large number of fine-scale focus
569 positions was not possible, and thus the particular images analyzed here, while visibly having the
570 best focus of the available data set, might not be at the absolute best possible focus. Second,
571 resolution is known to vary as a function of radial distance from the optic axis in these cameras,
572 a fact apparent even from visual inspection of the images, but this effect has not been included in
573 this analysis. For example, the corners of the M-100 rectangular field of view are slightly blurry
574 relative to the central regions; since these areas are outside the nominally-designed 1200 \times 1200
575 science imaging area of the field of view (Figure 2). However, this effect generally has not
576 impacted the quality of the science returned from Mars, as imaging requiring the highest
577 calibration fidelity (or for mosaicking purposes) includes only the central 1200 \times 1200 science

578 imaging area.

579 The MTF and resolution values derived above are likely to be conservative estimates of the
580 cameras' quantitative imaging performance. Indeed, the MTF and resolution performance may
581 seem poor compared to other imaging systems; this is at least partly a result of the effect of the
582 Bayer pattern color filter array bonded on top of the Mastcam CCDs. Bayer pattern filters like
583 this have been shown to create a significant decrease (a factor of 2 or more) in imaging system
584 MTF compared to monochrome systems (*e.g.*, Yotam *et al.*, 2007).

585 3.2.9. Stray and scattered light testing.

586 A qualitative assessment of the level of stray (from out of field sources) and scattered (from
587 in-field sources) light susceptibility for both Mastcams was conducted during ambient pressure
588 and temperature testing at MSSS on 31 August 2009 (for the M-100) and 30 September 2009
589 (for the M-34). Images were collected while a bright fiber optic point source was manually
590 moved just inside and outside of each camera's field of view. While the exact stray and scattered
591 light levels cannot be quantified from these test images, visual inspection of the data did not
592 reveal any obvious levels of stray light from bright sources just outside the fields of view of the
593 cameras, or obvious ghosts or glints from scattered light within the camera itself. Stray or
594 scattered light has also not proven to be a significant concern in flight data acquired on Mars,
595 although weak and offset ghost images of the Sun can be detected in solar filter imaging (see
596 §4.2.7).

597 3.2.10. Bad Pixels and/or Particulates on the Detectors.

598 CCD image sensors often have individual or groups of pixels that are either "dead" (non-
599 responsive), "gray" (responsive but either slightly more or less than average), or "hot" (saturated)
600 compared to their typical neighbors, regardless of the exposure time or incident light level. Gray
601 pixels that are somewhat less responsive than average are often caused by dust or other small
602 semi-opaque particulates adhering to the detector. CCD images, especially long-exposure images,
603 also often include an additional population of hot or gray pixels created via cosmic ray or other
604 high-energy particle interactions during the image exposure. Collectively, these kinds of
605 anomalous pixels are often referred to as bad pixels. The effects of bad pixels sometimes
606 propagate to their surrounding neighbors (± 3 -5 pixels in all directions) because of, for example,
607 charge bleeding, electronic shutter smear, Bayer pattern interpolation, or 8×8 pixel JPEG
608 compression. Dead and hot pixels (and potentially their contaminated neighbors) are typically

609 not correctable via calibration, while gray pixels sometimes are.

610 The Mastcam detectors exhibit a small fixed number of dead and gray pixels per camera, and
611 a variable number of hot pixels that depends on the exposure time of the images and the vagaries
612 of the solar cycle and cosmic ray flux activity. Hot pixels are not corrected in any way as part of
613 the Mastcam calibration pipeline, although they can be easily filtered and replaced for cosmetic
614 purposes using a standard low-pass or "dust and scratches" kind of filter found in many
615 commercial image processing applications. Gray pixels can be corrected by flatfielding, if their
616 responsivity is not substantially higher or lower than average and they have not changed since
617 the last time flatfield calibration images were acquired. Table 6 provides a list of the relatively
618 few currently-known and consistently dead, gray, or hot pixels for each of the Mastcam cameras,
619 based on pre-flight calibration measurements and in-flight performance on Mars. A few
620 additional pixels on both CCDs exhibited hot or gray behavior for a limited period of time, and
621 then went back to normal behavior (perhaps having self-annealed with continued operation).
622 Interpretation of morphologic or compositional variations in regions near and even around any of
623 these bad pixels (especially in the same column) should be avoided.

624 **3.2.11. Geologic Samples and Color/Reflectance Standards Imaging.**

625 In order to qualitatively assess the Mastcam system's abilities to resolve fine-scale detail and
626 color/multispectral variations within natural geologic materials, we also conducted a series of
627 ambient temperature and pressure multispectral imaging tests of a variety of diverse geologic
628 samples, as well as a set of reflectance, geometric, and colorimetric standards. Our test target
629 (Figure 14) is similar to targets that had been used for the same kind of "natural validation"
630 imaging by the Mars Exploration Rover Pancam instruments during their pre-flight calibration
631 and testing (*e.g.*, Morris & Graff, 2002; Bell *et al.*, 2003). Analysis of images of this target with
632 both the M-34 and M-100 multispectral filters demonstrated that relative reflectance (relative to
633 standards on the target) could be derived to better than 10% accuracy even at room temperature,
634 and that spectral variations in natural geologic samples could be detected and spatially mapped
635 using our narrow multispectral passband filters, even though the signal had also passed through
636 the overlying RGB Bayer filter pattern (*e.g.*, Figure 15).

637 **3.3. Pre-flight Geometric/Camera Model Testing and Validation.**

638 The Mastcam lenses exhibit almost no distortion (Ghaemi, 2009). One can observe the
639 undistorted nature of Mastcam images by examining pictures of dot targets like that shown in

640 Figure 11. These kinds of images show visually that the dot spacing and shape do not change
 641 visibly anywhere in the field of view, for either camera. However, a more accurate approach to
 642 geometric characterization involves determination of the instrument's camera model.

643 A geometric camera model is a set of equations that transform a 3D point in space to a 2D
 644 position in an image (pixel location). The model can also be inverted to transform a pixel in the
 645 image to a set of points in space that would map to that pixel (the imaging locus). The model
 646 contains the camera position and pointing vector, and it also models lens distortion and the
 647 interior geometry of the instrument. A camera model facilitates accurate monoscopic and
 648 stereoscopic measurement of points in an image or images, precise mosaicking of images, and
 649 creation of "linearized" (*i.e.*, geometrically corrected) image products (§5.2.9) for which lens
 650 distortion has been removed. To accommodate multiple kinds of existing end user software for
 651 geometric analyses, two kinds of initial, mathematically equivalent camera models have been
 652 developed for Mastcam and are described here.

653 3.3.1. Four-vector MSSS-produced CAHV camera model.

654 The first is a 4-vector "CAHV" photogrammetric model produced at MSSS that is routinely
 655 used by the Mastcam team in the creation of geometrically corrected Mastcam PDS archival data
 656 products (see §5.2.9). The CAHV camera model acronym refers to the vectors which permit
 657 transformation from object to image coordinates (*e.g.*, Yakimovsky & Cunningham, 1978;
 658 Gennery, 2001; Di & Li, 2004; see also the inset to Table 8 below). The one-letter CAHV model
 659 term definitions are:

- 660 • C: camera center vector from the ground coordinate system origin to the camera
 661 perspective center
- 662 • A: camera axis unit vector perpendicular to the image plane
- 663 • H, V: horizontal and vertical information vectors.

664 The CAHV model can be losslessly constructed from a pinhole camera model. Specifically,
 665 via the CAHV model, if P is a point in the scene, then the corresponding image location x, y
 666 (column, row) can be computed as follows:

$$667 \quad x = ((P - C) H) / ((P - C) A), \quad \text{and} \quad y = ((P - C) V) / ((P - C) A). \quad (3)$$

669
 670 To fit a photogrammetric camera model to the MSL Mastcams, we acquired a small set of

671 Assembly, Test, and Launch Operations (ATLO) geometric calibration target images at JPL on
 672 6-7 December 2010. For this activity, both Mastcam camera heads were viewing the same
 673 collection of JPL-provided dot targets (*e.g.*, Figure 11). The images have known (measured via
 674 laser metrology) object space (3D) coordinates for a set of points captured in the images. The 2D
 675 image space coordinates corresponding to the points were measured as accurately as possible
 676 using standard centroiding methods, and we used a nonlinear weighted least squares algorithm
 677 (also known as bundle adjustment; *e.g.*, Brown, 1958) to determine the set of parameters that
 678 minimize the difference between the 3D points projected into the image using the camera model
 679 and the points measured from the image.

680 We determined and correlated the center pixel location (to sub-pixel accuracy) for each dot in
 681 the available dot target images with the position of that point in the rover reference frame
 682 (determined by JPL-Caltech engineers, who surveyed the location of the four corners of each
 683 target). Following the bundle adjustment procedures described by Brown (1958) and Mikhail *et*
 684 *al.* (2001), we determined the exterior parameters (target positions and orientations), interior
 685 parameters (focal length and detector geometry), and lens distortion coefficients. The position for
 686 the farthest target was not adjusted so as to fix the scale of the system. We ran a single
 687 optimization that used data from all calibration images to model the effect of focus motor count
 688 where needed.

689 In our analysis, the term *focal length* refers to the value of a theoretical, ideal camera without
 690 distortion; this differs from the physical, effective focal length determined by lens design.
 691 Mastcam focal length (f_m) was modeled as a linear function dependent on each camera's focus
 692 motor count. The linear effect of motor count on focal length is referred to as the focus factor (f_f)
 693 and has units of millimeters of focal length per focus motor count. The function is:

694

$$695 \quad f_m = f_{nom} + f_f (m_{nom} - 2800) \quad (4),$$

696

697 where f_m is the modeled focal length at motor count m , and f_{nom} is a reference focal length at a
 698 nominal focus motor count of $m_{nom} = 2800$. The value of 2800 is somewhat arbitrary; we selected
 699 it because it is between the minimum and maximum focus positions for the M-100 camera. For
 700 the M-100 camera, the NLS procedure yielded $f_{nom} = 100.446803$ and $f_f = -2.547113e-03$,
 701 yielding M-100 focal lengths ranging from 104.329 mm to 99.170 mm for focus motor counts

702 ranging from 1276 to 3301, corresponding to distances of ~ 1.7 m to infinity, respectively. For
 703 the M-34 camera, focal length did not exhibit a statistically significant change with focus motor
 704 count in our NLS modeling; instead, a constant focal length of 34.367 mm was derived, as was
 705 expected from the theoretical design of the optics.

706 The origin of the image focal plane coordinate system (x, y) is at the principal point; that is,
 707 the location at which the optical axis intersects the focal plane. This is defined in millimeters,
 708 with the x direction to the right (increasing columns) and the y direction up (decreasing rows).
 709 The boresight is the same point, but defined in pixels (i, j) . Relative to the upper left Mastcam
 710 CCD pixel, defined as pixel $(0, 0)$ the M-34 boresight is located at column $i_0 = 834.62$, row
 711 $j_0 = 588.41$ and the M-100 boresight is located at column $i_0 = 836.11$, row $j_0 = 608.81$.

712 Radial distortion is measured in the focal plane relative to a point in the focal plane called the
 713 *center of distortion*. Here we assumed that the center of distortion is equal to the principal point.
 714 Given that r , the distance in millimeters of a point (x, y) in the focal plane from the principal
 715 point (x_0, y_0) for an ideal camera with no distortion is

$$716 \quad r = ((x-x_0)^2 + (y-y_0)^2)^{0.5} \quad (5),$$

718 then the radius for the actual camera with distortion is calculated as
 719

$$720 \quad r' = r (1 + k_1 r^2 + k_2 r^4) \quad (6).$$

722 Values for the distortion coefficients k_1 and k_2 are reported in Table 7. The value of k_2 for the
 723 M-100 camera was found to be statistically insignificant and thus set to zero. Higher order
 724 distortion terms were not needed to accurately model either camera's distortion.
 725

726 The mapping of points from the focal plane coordinate system (x, y) , in millimeters, to the
 727 image coordinate system (i, j) , in pixels, is defined as an affine transformation in which

$$728 \quad i = i_0 + a_{11}x + a_{12}y \quad (7),$$

$$730 \quad j = j_0 - a_{12}x - a_{11}y \quad (8),$$

732

733 and for which (i_0, j_0) is the boresight pixel. Because the focal length can be confounded with
734 pixel pitch, the value of a_{11} was set to the number of pixels on the array per millimeter and was
735 not adjusted during the analysis. Note that this indicates that the pixels may be slightly non-
736 square or that there may be a slight non-orthogonality of the focal plane axes. The affine
737 coefficients (in pixels per millimeter) determined by our analysis are listed in Table 7.

738 This initially-derived Mastcam camera model has some important limitations. For example,
739 (a) the movement of the principal point and the camera center due to focus motor count have not
740 been modeled; (b) the center of distortion might be offset from the principal point, (c) the change
741 in lens distortion parameters due to motor count/working distance has not been modeled; (d) the
742 effect of Martian environment temperatures on camera model parameters has not been modeled;
743 and (e) how well the linear model applies to focal lengths at minimum working distance and at
744 infinity has not been investigated. Uncertainties associated with those limitations could be
745 decreased with additional analysis of pre-flight or flight calibration data.

746 3.3.2. JPL-produced CAHVOR camera model.

747 The second Mastcam camera model is a six-vector CAHVOR model produced at JPL-Caltech
748 to support rover operations. The CAHVOR camera model parameters are reported with all of the
749 Mastcam images archived with the PDS *except* the geometrically corrected products, which use
750 the 4-vector model described in §3.3.1 above (see also §5.2.9). The CAHVOR model is an
751 extension of the CAHV that includes additional vector terms for optical ("O") and radial ("R")
752 distortion (*e.g.*, Yakimovsky & Cunningham, 1978; Gennery, 2001; Di & Li, 2004). As with the
753 MSL Navcam and Hazcam instruments (Maki *et al.*, 2012), a CAHVOR camera model was
754 produced for Mastcam at JPL-Caltech to support Curiosity rover operations. The calibration
755 effort followed the procedure described by Yakimovsky & Cunningham (1978), as modified by
756 Gennery (2001, 2006), and used the same targets that were set up in December 2010 for the MSL
757 Navcam and Hazcam calibration effort (Maki *et al.*, 2012; *e.g.*, Figure 11). The data analyzed
758 were based on the same six Mastcam image pairs acquired on 7 December 2010 that were
759 examined for the 4-vector model described above. The derived M-34 and M-100 CAHVOR
760 camera model coefficients are listed in Table 8, and are also listed within the data product label's
761 "GEOMETRIC_CAMERA_MODEL_PARMS" section for each of the PDS archived Mastcam
762 data products (EDR "_XXXX" images as well as RDR "_DRXX" and "_DRCX" products); see
763 §5.2.7), except for geometrically corrected (linearized) Mastcam archive RDR data products

764 ("DRLX" and "DRCL" products; see Table 13 below), which use the geometric camera model
765 parameters described in Table 7 and §3.3.1 above (see also §5.2.9).

766 Unlike the model in §3.3.1, the center of distortion in the JPL CAHVOR model is not
767 constrained to the principal point, as evidenced by the difference in the O and A vectors in Table
768 8, and that the radial distortion (R) includes higher-order terms. However, these are very slight
769 differences that are unlikely to have significant impact when using the models. More significant
770 is that the JPL model is not currently adjusted for focus, even for the M-100. Rather, it is a single
771 compromise model derived for an “average” focus (specifically, focus motor counts of 2315 for
772 the M-34, and 2702 for the M-100, although the models are a compromise at all focus values).
773 Incorporating focus into the JPL CAHVOR model is a task for future model improvements.

774 3.3.3. Pointing the JPL camera model.

775 The CAHVOR camera model combines both intrinsic parameters (camera internal geometry,
776 focal length, lens distortion, etc.) and extrinsic parameters (camera position and pointing vector)
777 into a single model. That means a given CAHVOR model can only be used at one specific
778 pointing. In order to use it at a different pointing, say as the mast is slewed around, the model
779 must be transformed to reflect the new extrinsic parameters. This section discusses the process
780 used by the JPL operations ground software (by MIPL, the Multimission Image Processing Lab),
781 which in turn mimics what is done onboard the rover. Thus, the camera models present in the
782 (non-linearized) PDS labels (see §5.2.9) can be re-created given the mast azimuth/elevation that
783 is also in the label. Alternatively, adjusted models can be created with refined pointing using
784 methods such as the mosaic bundle adjustment process described in Deen (2015).

785 Details of the algorithm, and an example showing its use, are in Appendix A. In summary, a
786 model of the mast head kinematics is used to derive the camera position (an arbitrary point that
787 moves with the head), and a quaternion expressing mast head rotation. The calibration camera
788 models similarly have a point and a quaternion attached (derived in the same way, representing
789 the extrinsic parameters of the camera pose during calibration). The calibration camera model is
790 then rotated by the inverse of the calibration quaternion and translated to the origin, effectively
791 removing the extrinsic parameters. The model is then rotated and translated to the desired
792 pointing, which results in a final model for a full-frame image. Most Mastcam images are
793 subframed, in order to return only the science portion of the image. Additionally, thumbnail
794 images are downsampled. These factors are applied to the full-frame camera model in order to

795 get the final model.

796 It should be noted that the same algorithm is also used to create pointed camera models for the
797 Navcam and Chemcam-RMI instruments. The parameters in [[[Table 9]]] are identical; only the
798 calibration models themselves differ. Note that a different treatment of MSL camera mast head
799 kinematics is presented in Peters (2016).

800 **4. In-Flight/Surface Calibration and Validation: Methods, Data** 801 **Sets, and Results**

802 **4.1. Cruise.**

803 Curiosity was launched on 26 November 2011. For instrument checkout purposes, three sets
804 of Mastcam bias/dark current images were obtained during the cruise to Mars, on 13 March, 20
805 April, and 14 June 2012. The cameras and RSM were stowed against the rover deck within the
806 completely dark confines of the sealed cruise stage spacecraft configuration. For each set of
807 images, two 1-second and two 10-second exposures were acquired from each camera. No
808 significant dark current was detected in the data sets, consistent with the cold temperatures of the
809 CCDs during these imaging sessions (0.8°C, -7.6°C, and -8.9°C, respectively), and the pre-flight
810 predictions of the dark current behavior (§3.2.2; Figure 8). Bias levels were also low, as expected.
811 Differencing of subsequent exposures did not reveal any anomalous noise behavior in the
812 cameras.

813 **4.2. Special In-Flight Calibration and Testing on Mars.**

814 **4.2.1. In-Flight Bias and Dark Current Testing.**

815 On Curiosity mission sols 320 and 321 (30 June and 1 July, 2013) and again on sols 1350 and
816 1351 (24 and 25 May, 2016), specific sets of Mastcam imaging sequences were commanded to
817 characterize the in-flight dark current performance of the cameras at different temperatures by
818 acquiring a series of images of the ground through the L7 and R7 solar ND filters (Table 10).
819 CCD temperatures for the M-100 camera are not routinely returned in telemetry as part of the
820 MSL telemetry architecture. However, we observed a strong correlation ($r^2 > 0.98$) between the
821 optics heater temperature (HTR1 in the PDS labels) of the M-34 camera when its heater is off,
822 and its routinely-reported CCD temperature (FPA temperature in the PDS labels). Thus, we used
823 that information to estimate a relationship between the routinely-reported M-100 HTR1

824 temperature and its rarely-reported FPA temperature. Specifically, we found that an estimate for
825 the M-100 CCD temperature can be made by assuming that CCD temperature in $^{\circ}\text{C} = 1.1 \times$
826 $\text{HTR1} + 3.0$, for times when HTR1 is off.

827 A background level of 117 DN (the DARK_LEVEL_CORRECTION value stored in the PDS
828 labels for these data files) was subtracted from all of the images by the DEA prior to downlink.
829 Table 10 shows that the background levels observed on Mars for the M-34 and M-100 cameras
830 are small at the typical operating temperatures of the CCDs, and consistent with the predictions
831 of the pre-flight background model described in §3.2.2 to within 2.5 DN at the warmest
832 operating temperatures of the CCD and electronics, and typically within ± 1 DN of the model for
833 typical operating temperatures.

834 4.2.2. In-Flight Electronic Shutter Smear Characterization.

835 For the small fraction ($< 10\%$) of Mastcam images acquired with very short exposure times
836 (typically < 6 msec), §3.2.3 showed that electronic shutter smear might need to be corrected in
837 order to achieve adequate radiometric and/or photometric accuracy, depending on the goals of
838 the observation in question. To enable assessment of the effects of shutter smear in real flight
839 data, as well as possible eventual higher-fidelity modeling and removal of the effects in
840 calibrated images, we acquired two observations on Mars.

841 The shutter smear test data were acquired on *Curiosity* sols 36 (sequence mcam00155) and 38
842 (mcam00169), and consisted of M-34 and M-100 images of the Mastcam calibration target and
843 bright rover deck surroundings acquired using very short exposure times (2.3 or 4.3 msec) and
844 immediately followed by identical images acquired at a commanded exposure time of 0.0 msec.
845 An example of the M-100 images from sol 38 are shown in Figure 16. The 4.3 msec image looks
846 normal, and does not reveal any obvious evidence of shutter smear (indeed, the analysis in
847 §3.2.3 showed that the worst-case effect in such an image would be only a 1.7% effect for pixels
848 near the bottom of the image). The zero-second image has an average signal level of about 7% of
849 the brightness of the 4.3 msec image and shows several interesting effects. First, the zero
850 exposure image exhibits a noticeable "smear" pattern in the direction towards the bottom of the
851 image (towards the horizontal shift register). But second, there is a faint residual or "ghost"
852 image of the original 4.3 msec scene superimposed upon the smear signal. The former is
853 expected based on the nature of electronic shutter smear in this CCD (§3.2.3). The latter,
854 however, is a manifestation of a different effect in the Mastcam images, related to the way

855 exposures are implemented in the FPGA logic of the Mastcam DEAs.

856 Essentially, if a zero-second exposure is commanded for the Mastcams, the resulting exposure
857 time is not actually zero. This is because even if a zero-second exposure is commanded, the CCD
858 still transfers charge from the photosites to the vertical register, it just does so a very short but
859 non-zero amount of time after the photosites have been cleared of charge by the electronic
860 shutter. In the Mastcam DEA FPGA logic, the commanded vertical transfer pulse duration for
861 each pixel is programmed to be about 106 μ sec wide, from start to finish (see Truesense, 2012
862 for electronic shutter timing details). While that time interval between the end of the commanded
863 "zero-second" exposure and the charge transfer into the vertical registers is very short, it is still
864 apparently long enough for observable signal to accumulate in the photosites from conventional
865 photocharge, and is thus not smear signal, *per se*. The fact that the ghost image is a faint mimic
866 of the non-zero exposure image supports this explanation. This explanation can be tested
867 empirically, using the sol 36 and 38 shutter smear test images. Scaling the nonzero exposure time
868 by the ratio of the average DN values in the zero-exposure to non-zero exposure images implies
869 an effective actual "zero-second" exposure time of around 90 μ sec. This is indeed comparable to
870 the stable duration of the vertical transfer pulse width.

871 This kind of ghost image, therefore, occurs in all Mastcam images after each exposure is
872 complete, but is amplified in the unusual (and unrealistic to implement) circumstance of
873 commanding a zero-second image. Both the ghost signal and the shutter smear are small,
874 however, and not apparent in most normal Mastcam images. The most noticeable effects of
875 shutter smear occur when there is a bright object near or past saturation in a surrounding darker
876 field (such as the calibration target scene in Figure 16). Shutter smear has also been observed in
877 MAHLI "self-portrait" images when looking at white rover structures, and in the Mars Descent
878 Imager (MARDI) descent sequence with the bright heat shield against the darker Martian surface,
879 as both of those cameras use the same CCD and timing logic.

880 [4.2.3. Improved Flatfields from In-Flight Sky Measurements.](#)

881 For the purpose of creating a flat-field image, sky images were taken on sols 36-38 (sequences
882 mcam00153, mcam00164, and mcam00173). The images were taken with the Sun low in the
883 west near 1600 LMST, and pointed towards the anti-Sun azimuth. During this time, there were
884 no expected or observed discrete clouds and the dust optical depth was about 0.79 (Lemmon,
885 2014). The concept was to acquire, in each filter, a 2 \times 2 mosaic centered on a fifth image. To

886 manage data volume, the mosaic underwent lossy compression and was used to characterize
887 large-scale radiance variations; the central image was losslessly compressed for use as a sky flat.
888 Due to operational time constraints, M-34 and M-100 images were acquired simultaneously. The
889 2×2 mosaic was designed such that the image centers overlapped the corners of the central image.

890 M-34 images were processed first, taking advantage of the complete overlap of the flat-field
891 image and the mosaic. We first describe the processing for filters 5 and 6, which have essentially
892 equal response from each component of the Bayer unit cell and can be considered a
893 monochromatic array. All images were read in; an inverse look-up table was used to derive
894 detector counts; mean bias and dark counts were derived from masked portions of the full frame
895 images and were subtracted from the whole image; cosmic ray strikes and hot pixels were
896 rejected with a selective median filter; a shutter image was calculated and subtracted; and the
897 images (which had been auto-exposed) were divided by exposure time and scaled by cosine of
898 the solar zenith angle to match the illumination of the central image. The initial flat field was
899 taken to be the central image (*i.e.*, the initial assumption was that the sky had uniform brightness).
900 A mapping between detector coordinates and sky coordinates (elevation and azimuth relative to
901 the Sun) was determined from image header and timing information. The following steps were
902 iterated 10 times: the 2×2 images were each divided by the flat field; they were projected into
903 sky coordinates and sampled at the projected geometry of the central image; a polynomial
904 (second order in azimuth and elevation) was fit to the sky mosaic to form a new sky radiance
905 model; the central image was divided by the sky radiance model to produce a new flat-field
906 image; and the result was normalized to the mean of the sky model radiance for the 128×128
907 pixels around the optical axis (adjusted due to Bayer and JPEG constraints to detector lines 528-
908 655 and samples 768-895). For inspection, a final mosaic was created, with the central image on
909 top of the other sky images; the result was then verified to be free of significant artifacts from
910 variations in sky brightness, such as seams or discrete cloud features. The resulting flat field was
911 stored as an image of the detector (*i.e.*, a 1648×1200 monochrome image).

912 M-34 images from filters 1-4 were processed similarly, but the analysis had to account for the
913 Bayer sampling. For each, one or more elements in the Bayer unit cell had significant response to
914 light through the filter, and one or more elements had substantially less response. The losslessly
915 compressed central image returned all elements and showed their relative response. The JPEG
916 compressed 2×2 mosaic images had been (on board) sampled only in their responsive cells

917 (green for L1, blue for L2, and red for L3-L4 and R3) and interpolated for the other cells. A
918 mask was created such that interpolated cells were not used in the analysis, but the above process
919 was otherwise followed. For these filters, two flat-field images were created. The first is for
920 lossless images, and shows the relative response differences in the Bayer unit cell that come from
921 dividing the losslessly-compressed image by the sky model. The second is for JPEG images, and
922 samples the flat field at responsive elements of the unit cell, with bilinear interpolation over the
923 other elements.

924 M-34 images from filter 0 contain color information. The processing was similar, except that
925 the 3 bands (red, green, blue) were done separately, allowing for different sky models. This also
926 resulted in two distinct flat-field images. The first, for losslessly compressed images, is 2-
927 dimensional. Unlike the lossless flat fields discussed above, the mean effect of the Bayer pattern
928 has been divided out due to the normalization by three independent sky models. Thus, use of this
929 flat field does not affect the relative signal in red, green, and blue. The flat-field image for JPEG-
930 compressed images is 3-dimensional, with each band's flat-field image calculated from the raw
931 image using constant-hue based interpolation.

932 M-100 images were originally intended to undergo the same procedure, but accomplishing
933 that would have required a separate grid with $\sim 5^\circ$ between mosaic images rather than $\sim 15^\circ$. For
934 efficient use of time, the images for each camera were taken in parallel. As a result, the spacing
935 of the M-100 images is not ideal for the above procedure. However, for filters R0 (RGB), R1, R2,
936 and R6, the above process produced detail sky radiance information for the appropriate time and
937 wavelength from M-34 images. In these cases, the M-100 central image, after the input and
938 preprocessing steps, was divided by the M-34 sky model to produce a flat-field image. For filters
939 R3, R4, and R5, the same process was used except that the model was a linear interpolation
940 between M-34 models adjacent in wavelength (751, 867, and 1012 nm for M-34, 805, 908, and
941 937 nm for M-100). The resulting flat field was normalized to the mean of the sky model
942 radiance for the 128x128 pixels around the optical axis (adjusted due to Bayer and JPEG
943 constraints to detector lines 600-727 and samples 696-823). This resulted in monochromatic flat-
944 field images for R4, R5, and R6; separate lossless and JPEG monochromatic flat-field images for
945 R1, R2, and R3; and a monochrome and 3-band flat-field image for R0.

946 During the acquisition of these sequences, the focus was set to be typical of mid-field imaging.
947 Vignetting around the edges of the field (Figure 9) is focus-dependent, so masking of the borders

948 of the flat field is recommended (areas where a responsive Bayer channel's flat field value is >
949 0.75 are acceptable; those that are $0.25 \leq \text{flat-field} \leq 0.75$ may be useful for mid-field distances;
950 those that are < 0.25 are not expected to be reliable). The flat-field images account for variations
951 in detector response. However, there are some pixels that are insufficiently responsive; these
952 may be identified using the same criteria as for vignetting. Use of a look-up table to compress all
953 images to 8 bits per pixel (prior to JPEG or lossless predictive compression) limits the accuracy
954 of the flat field to $\sim 1\%$ per pixel for the primary Bayer channels for each filter and $\sim 2\%$ or worse
955 for the other channels.

956 4.2.4. Validation and Improvement of Radiance Calibration from In-Flight Sky Measurements

957 Several sky-crossing Mastcam imaging surveys have been obtained at different times during
958 the mission, partly for atmospheric science purposes and partly to provide an independent
959 validation (via modeling) of the Mastcam absolute radiometric calibration (§3.2.6). For example,
960 on sol 1645, sequences mcam008516 and mcam008517 were designed and run to constrain the
961 absolute radiometric calibration of each Mastcam filter. Specifically, 94 images were obtained
962 through all left eye (M-34) filters (Table 2), as well as right eye (M-100) filters R3, R4, and R5
963 (805, 908, and 937 nm). Images including scattering angles of 5° - 150° were obtained through M-
964 34 filters L1, L2, and L4 (527, 445, and 676 nm). The data were acquired at an FPA temperature
965 of approximately -7°C .

966 The images were calibrated to radiance using the Version 2 pipeline described in this paper,
967 and the radiance calibration coefficients in Table 4, and were then modeled with a retrieval code
968 based on DISORT (Stamnes *et al.*, 1988). For initial parameters, the aerosol model of Tomasko
969 *et al.* (1999) was used for aerosol mean radius, a ; variance of the size distribution, b ; slope of
970 internally scattered light, G ; and angle of minimum internally scattered light, θ_{min} . These
971 parameters describe the shape of an arbitrary phase function, with the first two parameters
972 controlling forward-scattering, and the last two parameters controlling side and back scattering.
973 Initial single scattering albedo as a function of wavelength was updated to values from Wolff *et al.*
974 *et al.* (2009), obtained from orbit under global dust storm conditions. The L1, L2, and L4 filters
975 (527, 445, and 676 nm) were modeled, allowing an arbitrary adjustment to radiance to achieve a
976 best fit. The model fits were all based on the shape of the radiance profile across the sky, with
977 the absolute calibration normalized out. An implied calibration parameter (radiance per DN/s)
978 was extracted from the fits (Table 11), and errors between the best-fit model radiances and as-

979 calibrated original radiances were observed to be less than 1%. Values of $a=1.25 \mu\text{m}$ and $b=0.22$
980 were used for all models, based on results from these three filters. Each of the remaining filters
981 were fit without adjusting the size distribution; left eye modeled radiance fits were generally also
982 sub-percent accuracy, while right eye fits had 1-2% errors relative to the original as-calibrated
983 radiances. Table 11 compares the laboratory-derived radiance calibration coefficients (Table 4)
984 to the coefficients derived from this sky modeling work. The sky model is considered to have a
985 10% uncertainty for the purposes of this comparison.

986 Right-eye (M-100) versions of filters in common between the two cameras were not included
987 in the above analysis, because of the preferentially-larger larger left eye (M-34) field of view and
988 the desire to acquire sky images spanning a wide range of azimuths and elevations as close
989 together in time as possible. Instead, sky flat images (*e.g.*, §5.3.4) in which the left and right eyes
990 were commanded as stereo pairs, were used to derive an in-flight left/right eye response ratio.
991 Table 11 shows that ratio for each right-eye filter that has a left-eye counterpart. The radiometric
992 calibration for the sky model has been derived from the left eye value and the left/right ratio.

993 We note that despite the difference in temperature between the input data sets (ambient pre-
994 flight data vs. -7°C in-flight data), in general the laboratory calibration and sky model calibration
995 match closely (Table 11). There was no bias toward this: the normalization removed any input
996 from the laboratory absolute radiance calibration, and the process was done "blind" to the
997 normalization constant. This modeling work thus provides an independent validation of the
998 required better than $\pm 10\%$ accuracy of most of the Version 2 radiance calibration coefficients
999 listed in Table 4. The exceptions are (a) several near-IR filters (L6, R3, R4) for which the
1000 differences between the pre-flight and sky model coefficients are consistent with better than
1001 $\pm 10\%$ to $\pm 15\%$ accuracy; and (b) the narrowband blue filters, L2 and R2 (near 445 nm), which
1002 exhibit significantly larger differences in derived radiance coefficients. The larger L2 and R2
1003 uncertainties are consistent with the significantly higher uncertainties in their laboratory radiance
1004 calibration coefficients (Table 4), because of their relatively poorer fit to the calibration lamp
1005 spectrum (Figure 10) and the lower SNR of the data acquired for their spectral throughput
1006 characterization (see §3.2.4). Therefore, because of the much better agreement between the
1007 laboratory pre-flight and independent in-flight sky model derived radiometric calibration
1008 coefficients for all of the other Mastcam filters, the sky model-derived radiometric calibration
1009 coefficients for the L2 and R2 filters in Table 11 are most likely better values to use than those in

1010 Table 4 to estimate the absolute radiances of images acquired through those two specific filters.

1011 4.2.5. Focus Testing/Performance.

1012 Two sets of tests were conducted to characterize and validate the focus calibration of the
1013 Mastcams in flight. First, a series of measurements taken in coordination with the MSL
1014 ChemCam instrument were used to refine the pre-flight calibration of focus motor count versus
1015 distance to target (§3.2.7) over the range of temperatures and other environmental conditions
1016 actually experienced on Mars. Then, a series of additional Mastcam images of the same targets
1017 over a variety of temperatures typical of flight operations was obtained in order to characterize
1018 small deviations in the geometric (camera model) parameters of the cameras over that range of
1019 conditions.

1020 *4.2.5.1. Focus vs. Motor Count Validation.* In order to validate the pre-flight calibration of
1021 Mastcam focus motor count versus distance under Mars conditions, as well as to provide end
1022 users a way to estimate distance to imaged targets (and thus their spatial scale), analysis was
1023 conducted on 271 sets of M-100 images and 93 sets of M-34 images for which nearly-concurrent
1024 distance data were obtained by the ChemCam instrument's laser range finder (Wiens *et al.*, 2012).
1025 For the M-100 camera, we found a strong linear fit ($R^2 > 0.993$) between best focus position
1026 identified by the camera's onboard autofocus algorithm and $1/\text{distance}$ as determined by
1027 ChemCam [the few cm difference in distance to the scene between the ChemCam optics and the
1028 Mastcam optics (Figure 4) is a small and relatively insignificant fraction of the total distance].
1029 While the difference between observed and predicted focus motor counts in this fit is within ± 15
1030 focus motor counts (2% of the typical focus count range) for more than half the data analyzed,
1031 deviations in the fit of up to ± 60 focus motor counts were noted for the rest of the images. Those
1032 deviations were found to have a good linear correlation ($R^2 > 0.790$) with the temperature of the
1033 M-100 camera (as recorded in the OPTICS_TEMP keyword value in the PDS archive labels).
1034 Thus, a temperature-dependent correction was generated for the M-100 camera. For the M-34
1035 camera, the linear fit between best focus and $1/\text{distance}$ were also highly correlated ($R^2 > 0.982$).
1036 Deviations with temperature for the M-34 focus calibration were found to span about ± 15 focus
1037 motor counts for all of the images, but were not observed to correlate with the temperature of the
1038 camera (consistent with the wider-angle M-34 camera having a substantially lesser sensitivity to
1039 focus than the narrow-angle M-100).

1040 The resulting refined in-flight calibrations for the relationship between focus motor count and

1041 distance to target were found to be:

1042

1043 $M-34: \quad D = 363.64 / (2427.50 - F_{34}) \quad (9) \text{ and}$

1044 $M-100: \quad D = 3322.3 / (3491.9 - 2.58T - F_{100}) \quad (10),$

1045

1046 where D is the distance to the focused image target in meters, T is temperature of the camera
1047 in degrees C, and F_{34} and F_{100} are the focus motor counts commanded to the M-34 and M-100
1048 cameras, respectively (and stored in the FOCUS_POSITION_COUNT keyword in the archived
1049 PDS labels).

1050 These models do an excellent job of matching the "true" distance to the target scene in more
1051 than 90% of the cases examined to date. Most of the cases where the model is not giving as good
1052 a fit are for the M-100, where the actual temperature of the camera could potentially be more
1053 than $\pm 5^\circ\text{C}$ different from the reported optics temperature, especially during active heating (the
1054 M-100 temperature sensor is on an external heater; see §4.2.1). Another possible cause of
1055 distance discrepancies is that many of the targets were rocks that do not fill the field of view.
1056 Experience using the cameras on Mars shows that the combination of partial field-filing rocks
1057 and surrounding materials creates additional scene entropy that can cause the autofocus
1058 algorithm (the same as used on the MAHLI camera; see §7.2.2 and §7.2.3 in Edgett *et al.*, 2012
1059 for details) to "pull" back to lower focus motor counts relative to other kinds of scenes.

1060 Finally, chromatic aberration in the Mastcam optics in the near-IR could also cause some
1061 discrepancies in estimated distances to imaged targets. Typically, autofocus is performed on
1062 images through the L0 and R0 filters (at visible R, G, and B wavelengths; Table 2) and not at
1063 other wavelengths that might be acquired in the same imaging sequence. Specific in-flight tests
1064 of autofocus at other wavelengths, however, performed on sols 468, 475, 488, and 493
1065 (sequences mcam01864, mcam01888, mcam01934, and mcam01960) of targets 70, 60, 2.4, and
1066 10 m away, respectively, showed that best focus was achieved 25 focus motor counts lower in
1067 the M-34 L6 filter (1012 nm) and 52 motor counts lower in the M-100 R6 filter (1013 nm) than
1068 for RGB images acquired in the same sequence. While the slightly defocused nature of the near-
1069 IR images in Mastcam multispectral data sets has not proven to be an impediment to scientific
1070 analyses (mostly because spectra are typically extracted from groups of tens to hundreds of
1071 pixels, rather than single pixels; see §5.4.4), users interested in quickly estimating

1072 distances/spatial scales of targets in multispectral sequences should default to using Equations 9
1073 and 10 with the recorded FOCUS_POSITION_COUNT values from the associated RGB filter
1074 L0 or R0 images also always acquired in such sequences.

1075 [4.2.5.2. Thermal Focus Test.](#) So-called "thermal focus test" images were obtained in flight
1076 on Mars during Curiosity sols 917 and 918 (6 and 7 March 2015) to characterize the effects of
1077 temperature on the position of the focus mechanism for focused Mastcam images. The test was
1078 motivated by slight differences between the laboratory calibrated focus motor count values and
1079 the in-flight focus motor count values for any given distance. The proposed hypothesis was that
1080 the differences in motor positions were correlated to differences in the temperature of the camera
1081 head, and that thermal contraction of the camera head at the colder temperatures in flight was
1082 causing the focus position to shift slightly.

1083 The image observations consisted of a 3×3 raster of losslessly-compressed images acquired
1084 with both the M-34 and M-100 cameras of the same target region (identical RSM pointing
1085 angles) at several different times of day, refocused using autofocus for each image in the mosaic.
1086 The rationale behind the 3×3 raster was that it allowed statistical testing of the results. The
1087 different times of day were chosen to capture a range of diurnal temperatures at roughly 10°C
1088 intervals between about -30°C to 0°C. A high-entropy scene was selected for the test, located
1089 ~15 m (±2 m) due south of the rover so that the shadows were symmetric across the day. The
1090 motor count values from each of the autofocus images were used to characterize the change in
1091 focus as a function of temperature (Figure 17). The results show that the focus changes by ~0.8
1092 motor counts/°C for the M-34 and ~2.5 motor counts/°C for the M-100.

1093 [4.2.6. Compression Testing/Performance.](#)

1094 Most Mastcam images have been returned from Mars using some level of lossy JPEG
1095 compression (for details, see both of Appendix E and §4.4.5.4 in Malin *et al.*, 2013). Several
1096 studies have been conducted by the Mastcam operations team using flight Mastcam data to
1097 assess the performance of the compressor, and its influence on the returned science data. For
1098 example, one study determined the average compressed data volume of JPEG-compressed M-34
1099 and M-100 images of hundreds of representative Martian scenes as a function of JPEG quality
1100 factor (ranging from 0-100; see Pennebaker & Mitchell, 1992). Scene activity, image dimensions
1101 (depth of field), and focus quality were all found to influence compression efficiency to different
1102 degrees. The results (Figure 18, which also shows compression study results from the MAHLI

1103 and MARDI cameras) show that images from the M-100 camera generally compress better than
1104 those from the M-34 camera for images commanded to the same JPEG quality factor. The 0.5 to
1105 1.0 bit per pixel increase in compressibility of M-100 images compared to M-34 is likely due to
1106 the much larger depth of field of the M-34 camera. An important operational implication from
1107 Figure 18 is that JPEG compression of M-34 or M-100 images using high quality factors (*e.g.*, \geq
1108 90) can reduce downlinked data volume by up to a factor of two compared to lossless
1109 compression. And as shown in §5.4.1 below, the difference in image quality between losslessly-
1110 compressed images and those JPEG compressed to high quality factors is usually imperceptible
1111 to the human eye.

1112 Another compression test examined the influence of JPEG quality factor on the extraction of
1113 12-color Mastcam "spectra" of various regions of interest. For example, lossless Mastcam
1114 multispectral images from the sol 281 drill hole imaging campaign in "Yellowknife Bay"
1115 (Grotzinger *et al.*, 2014) were re-compressed after downlink using a copy of the onboard JPEG
1116 compression algorithm and converted to compressed images at JPEG quality factors of 85 and 45.
1117 Mastcam data from bright reddish dusty surfaces, darker reddish sandy surfaces, and gray drill
1118 tailings were extracted from the same multi-pixel regions of interest (ROIs) at all compression
1119 levels. The averages and standard deviations of the resulting 12-color Mastcam "spectra" of the
1120 regions are virtually identical in the lossless and quality 85 and 45 data sets. This is perhaps not
1121 surprising, as typical ROIs were extracted from large pixel regions compared to the 8×8 pixel
1122 compression block of the JPEG algorithm. While large differences in pixel-to-pixel brightnesses
1123 can easily be visually detected within small (comparable to the 8×8 pixel compression blocks)
1124 groups of pixels when images of different JPEG quality factors are examined at high zoom, the
1125 JPEG compressor does a very good job of preserving the overall average signal level of the scene
1126 when integrated over larger pixel regions. Thus, in practice, care should always be used to
1127 extract Mastcam spectra from ROIs that are large compared to the 8×8 pixel JPEG compression
1128 blocks, to avoid incorrect interpretation of smaller-scale compression artifacts.

1129 4.2.7. In-Flight Scattered Light Testing.

1130 Scattered (from in-field sources) light within the Mastcams is generally difficult to quantify
1131 during Mars surface operations. However, imaging of the solar disk using the neutral density
1132 solar filters provides a special opportunity to characterize scattered light effects, at least for solar
1133 imaging data sets. For example, on *Curiosity* sol 33, a series of images of the Sun's disk were

1134 taken through both the M-34 and M-100 cameras (sequences mcam00008 and mcam00009).
1135 Images of the Sun through the M-100 camera's filter R7 (10^{-5} neutral density filter plus 440 ± 20
1136 nm narrowband filter) show several low-level ($\leq 5\%$ intensity) ghost images of the Sun, as well
1137 as a very high-level (100% to 300% of the primary solar image's signal level) ghost image
1138 associated with a pinhole filter leak at the bottom of the field of view. Fortunately, all of the
1139 ghost/leak images are offset substantially (many hundreds of pixels) from the primary image of
1140 the Sun, and their signals show no influence on the signal levels of the direct solar image itself.
1141 Images through the M-34 camera's filter L7 (10^{-5} neutral density filter plus 880 ± 10 nm
1142 narrowband filter) do not show any similar ghosts or apparent filter leaks, but they do reveal a
1143 small "halo" of scattered light surrounding the Sun's disk, at an intensity of $\sim 1\%$ of the Sun's DN
1144 level. Because of their relatively low signal levels and/or their wide spatial separation from the
1145 direct images of the Sun, however, neither this level of scattered light in the M-34 solar images
1146 nor the large ghost images and apparent filter leaks seen in the M-100 solar image data have
1147 impeded the ability to derive accurate estimates of the Martian atmospheric opacity using the
1148 Mastcams (*e.g.*, Lemmon, 2014).

1149 4.3. Mastcam Calibration Target Imaging.

1150 As described in §2.2, Mastcam includes an external calibration target mounted on the top of
1151 the RPFA box on the rover deck (Figure 4). Imaging of the target enables a way to quickly
1152 calibrate other sequences to a quantitative estimate of radiance factor (I/F , see §5.2.7), a quantity
1153 directly comparable to laboratory reflectance spectra of rocks and minerals. Perhaps most
1154 importantly, because the target is being illuminated by both direct sunlight as well as indirect
1155 diffuse (and significantly reddened) sky radiance, calibration of the scenery around the rover
1156 relative to the calibration target can effectively remove almost all of the spectral reddening
1157 effects of the diffuse illumination in the scene, for scenes that are observed at comparable solar
1158 incidence angles as the calibration target (*e.g.*, Bell *et al.*, 2006). This enables tactical-timescale
1159 quick-look assessment of the reflectance properties of the scene without having to perform
1160 detailed (and time-consuming) radiative transfer modeling of the atmospheric component of the
1161 observed scene radiance. A comparison of in-flight Mastcam "spectra" of the calibration target to
1162 pre-flight high-spectral resolution laboratory spectra of the calibration materials by Wellington *et al.*
1163 (*et al.* (2016) shows that the multispectral data calibration pipeline described below (§5.3.6) can
1164 reproduce very well the actual spectral properties of the target materials, increasing our

1165 confidence in the pipeline's ability to accurately represent the spectral properties of Martian
1166 scenes being imaged.

1167 The Mastcam calibration target is not usually imaged when other sequences are only being
1168 acquired through the RGB Bayer filters (filter position 0 in both cameras), because quantitative
1169 reflectance assessment of the scene is typically not the goal of RGB-only imaging. Conversely,
1170 the calibration target is almost always imaged close in time to multispectral sequences that
1171 observe the scene using the narrowband science filters (Table 2) in addition to the RGB Bayer
1172 filters. As a general rule, the calibration target is imaged at the same approximate Local True
1173 Solar Time (LTST; within about an hour before or after) and with the same filter set as the to-be-
1174 calibrated multispectral sequence with which it is associated. If time, power, or data volume are
1175 heavily constrained, however, a new calibration target sequence may not have been taken if one
1176 already exists from a previous recent sol (within about 5 sols) that was taken at a similar LTST
1177 (again, within about one hour of that time). To save data volume and avoid imaging of
1178 unnecessary other parts of the rover deck, downlinked images of the calibration target since
1179 *Curiosity* sol 66 (sequence mcam00297) have been sub-framed to 384×320 pixels for the M-34
1180 camera (starting at CCD row 721 and column 625) and 1152×944 pixels for the M-100 (starting
1181 at CCD row 33 and column 305).

1182 Starting on *Curiosity* sol 3 and extending to sol 1159 (the most recent PDS data release as of
1183 this writing), 223 Mastcam imaging sequences of the calibration target were obtained,
1184 corresponding to imaging of the target approximately every 5 sols. The total downlinked
1185 Mastcam data volume dedicated to calibration target imaging has been less than 0.5% of the total
1186 downlinked Mastcam data volume overall. Over time, airfall dust has slowly settled onto the
1187 target (Figure 4), decreasing its contrast and necessitating the development of a dust correction
1188 model to compensate for the influence of a thin but still semi-transparent layer of dust on the
1189 color and photometric properties of the calibration standard materials. Section 5.3.6 describes
1190 this dust model, as well as the general use of the calibration target in the enhanced Mastcam data
1191 calibration pipeline.

1192 **5. Data Reduction, Validation, and Archiving**

1193 **5.1. Introduction and Methodology.**

1194 Figure 19 provides a simplified overview of the basic steps in the current MSL/Mastcam data

1195 reduction and calibration pipeline. Full-frame or sub-framed (but not thumbnail) images (Table
1196 3) are calibrated to radiance factor (I/F ; see §5.2.7) using a variety of pre-flight and in-flight
1197 ancillary data files and images. Section 5.2 describes the initial tactical calibration pipeline being
1198 used to generate current PDS-released EDR and RDR archive products from the Mastcam
1199 investigation. Section 5.3 describes further planned enhancements to these initial calibrations, in
1200 works for future PDS archive releases of the Mastcam data. Section 5.4 describes some examples
1201 useful for the validation of the accuracy and precision of the Mastcam calibration. Finally, §5.5
1202 provides a summary of Mastcam Data Products and PDS Archive products.

1203 **5.2. Initial (Tactical) Data Reduction and Calibration Pipeline.**

1204 An initial version of the calibration pipeline steps in Figure 19 is being used to generate rapid-
1205 timescale (approximately daily) versions of calibrated Mastcam RDRs for tactical use by the
1206 MSL Science Team, as well as initial Version 1 PDS archive versions of calibrated Mastcam
1207 RDRs for use by the broader community. This section describes those initial calibration steps in
1208 detail.

1209 **5.2.1. Decompression.**

1210 If the raw EDRs (*.dat files in the PDS archive) were compressed for downlink, then the first
1211 step is to decompress the data into the proper spatial domain format. For example, if the data
1212 were JPEG color compressed, then the YCrCb coefficients of the 8x8 pixel frequency domain
1213 JPEG Minimum Coded Units (MCUs) are transformed back into 8x8 spatial MCUs and
1214 reordered into image arrays for each of the three RGB output color bands, and the output is a 24-
1215 bit (3 band sequential channels) color image. For JPEG grayscale compressed data, just the
1216 luminance (Y) channel is transformed back into a single channel 8-bit grayscale output image.
1217 For losslessly-compressed data, the Huffman decoding process described in Appendix C of
1218 Malin *et al.* (2013) is used to create the decoded images.

1219 An important part of the decompression process for Mastcam images that have been JPEG
1220 compressed is performing a Bayer pattern interpolation (also known as "debayering" or in some
1221 contexts "demosaicing") to create the separate full-sized RGB channels of the output
1222 decompressed JPEG. A raw image from a sensor with a Bayer filter often results in what looks
1223 like high frequency noise in a zoomed out image, and while zoomed in may look like a
1224 discontinuous checkerboard-like pattern (Figure 20). This appearance is due to the interleaving
1225 of the red, green and blue channels in the Bayer pattern (*e.g.*, Figure 2). For typical viewing, this

1226 raw sensor data are passed through an interpolation algorithm that computes the missing Bayer
1227 colors for each given pixel of the R, G, and B channels of the image. For instance, where the
1228 sensor has a red filter, the interpolation algorithm will compute the data for the same pixel in the
1229 corresponding green and blue channels using information from neighboring pixels. All Mastcam
1230 images are acquired through the Bayer color filter array pattern, but that pattern can be
1231 (optionally) interpolated either within the camera electronics, or using ground processing after
1232 downlink. For normal RGB imaging through the broadband Filter 0 (Table 2; Figure 3), the
1233 interpolation method employed within the instrument to produce color JPEG products is a
1234 hardware implementation of the algorithm developed by Malvar *et al.* (2004). Section 5.3.1
1235 below compares the default debayering algorithm for Mastcam data to several alternatives.

1236 Mastcam supports losslessly-compressed (first-difference Huffman encoding) image
1237 acquisition modes that return raw or near-raw image data that contain the Bayer pattern. Lossless
1238 or completely uncompressed non-thumbnail EDR product types A, B, C, J, and K (Table 3)
1239 contain the Bayer color filter array pattern and can be interpolated using ground processing. Data
1240 compressed with lossy (JPEG) compression modes return images that have been interpolated
1241 onboard the rover, prior to downlink. Lossy JPEG-compressed images (EDR product types D, E,
1242 and F; Table 3) are interpolated based on how well the bandpass of the commanded science filter
1243 (Filters 1-7, if used) overlaps the red, green or blue Bayer filter bandpasses. Specifically, kernels
1244 are applied to the science filter data prior to compression to either discard two of the three Bayer
1245 colors that are outside the science filter bandpass, or to enable the use of all three Bayer colors
1246 for science filter wavelengths beyond which the Bayer filters are transparent (see §3.2.4, Figure
1247 3, and Table 2). Table 12 describes which interpolation scheme is used for which camera and
1248 filter combination when lossy JPEG compression is used to downlink images from Mars.

1249 Bayer interpolation of uncompressed or losslessly-compressed images (EDR product types A,
1250 B, and C; Table 3) is accomplished after downlink either real-time in analysis tools used by the
1251 MSL Science Team, or as the first step ("Decompression") in the generation of calibrated RDR
1252 and PDS archive products (Figure 19).

1253 5.2.2. Compadding and Decompadding.

1254 "Compadding" is a portmanteau word blend of the words "compressing" and "expanding," and
1255 refers to the process of compressing the original 11-bit (0-2047) DN values of each raw Mastcam
1256 pixel down to 8 bits (0-255) of dynamic range. The process is sometimes also referred to as

1257 resampling (*e.g.*, Bell *et al.*, 2006). Companding is performed because it is usually desirable to
1258 scale the data down to a smaller number of bits per pixel so that Poisson (shot) noise is not
1259 encoded or downlinked in the telemetry. Because Poisson noise in detectors like CCDs is
1260 proportional to the square root of the number of electrons detected, using a square-root-based
1261 lookup table (LUT) to scale the original 11-bit data down to 8-bits of dynamic range provides a
1262 way to decrease the number of bits downlinked without incurring a statistically significant loss of
1263 information (*i.e.*, the noise is not quantized). For example, an original 11-bit Mastcam DN value
1264 of 1700 corresponds to a signal of $\sim 27,200 e^-$ (Table 1), which has a Poisson (counting) noise of
1265 $\sqrt{27,200}$ or $\sim 165 e^-$, or ~ 10.3 DN. Thus, there is no statistical difference (within the noise of the
1266 measurement) between Mastcam DN values of 1695, 1700, or 1705 DN. We therefore
1267 "compand" the original DN value of 1700 DN into the 8-bit value of 232. After downlink, the 8-
1268 bit value of 232 is "decompanded" back to the 11-bit value of 1698, which is statistically
1269 identical to the original measured 11-bit value of 1700 DN. Because of the square root nature of
1270 Poisson noise, there is an approximately 1-to-1 mapping of 11-bit values to 8-bit values for low
1271 DN values, and a many-to-1 mapping of 11-bit values to 8-bit values for high DN values. Almost
1272 all Mastcam images have been companded on the rover (within the Mastcam DEA) using the
1273 square-root based LUT provided here in Appendix B. Details on the 31 other potential Mastcam
1274 LUTs are provided in Appendix B of Malin *et al.*, 2013. The opposite process, expanding the
1275 downlinked 8-bit data back to an estimate of their original 11-bit value, is referred to here as
1276 "decompanding," and is essentially part of the decompression process in the pipeline processing
1277 of Mastcam images.

1278 5.2.3. Dark Current Modeling and Removal.

1279 Under normal conditions, the Mastcam cameras generate only a small amount of dark current.
1280 A temperature-dependent model of dark current was generated during thermal vacuum testing,
1281 and this model can be applied routinely (§3.2.2, Figure 8). A biased offset is also built in to the
1282 Mastcam signal chain, to provide room to accommodate variations in electronic behavior of the
1283 detector. Estimates of the bias and dark current can be made by using masked (dark) columns on
1284 the detector (Figure 2) to extract dark current values, or by special bias and dark current full-
1285 frame images acquired occasionally in flight (§4.2.1). There are three ways currently
1286 implemented in the Mastcam calibration pipeline to remove the effects of bias and dark current:
1287 (a) using masked (dark) pixels, if they were downlinked with the images to be calibrated; (b)

1288 using the pre-flight model of bias and dark current versus FPA temperature; or (c) "manual" bias
1289 and dark current correction using analogous measurements from images acquired under similar
1290 circumstances.

1291 *5.2.3.1. Using Dark Columns.* Some rows columns of pixels along the edges of the detector are
1292 masked (Figure 2), specifically corresponding to columns 0-22 and 1631-1647 in full-width 1648
1293 pixel Mastcam images. These pixels have the same bias level, and accumulate dark current
1294 during an image exposure in the same manner, as photoactive pixels. The detailed layout of the
1295 first 24 columns of full-width Mastcam images is provided in Figure 21. Note that JPEG
1296 Minimum Coded Units (MCU) for lossy compressed data occur in blocks of 8×8 pixels. For
1297 images compressed as JPEGs, the dark pixel in column 7 is compressed with non-dark pixels
1298 from MCU 0. For this reason, only dark columns 8 – 15, corresponding to JPEG MCU 1, are
1299 used by Mastcam RDR processing. Thumbnail processing also takes into account the
1300 compression applied. Specifically, thumbnails effectively average all 8 of the JPEG MCU 1
1301 pixels into a single thumbnail pixel. Thus, only the second thumbnail pixel column is used for
1302 bias and dark current subtraction, for thumbnails generated from full-frame Mastcam images.

1303 For consistency, all images, even if not JPEG compressed, use the same group of 8 pixels,
1304 from dark columns 8-15 in full-frame Mastcam images, or column 1 (2nd column) in full-frame
1305 thumbnail image, for dark correction. The average of these 8 pixels (or just the 2nd column, if
1306 the image is a thumbnail) along the entire height of the image are used to estimate the combined
1307 bias and dark current signal, and this average (recorded in the DARK_LEVEL_CORRECTION
1308 processing parameter keyword in the archived PDS labels) is then subtracted from all pixels in
1309 the original image. If the image is a full-height (1200 rows) image or a thumbnail, the first two
1310 and last two lines (rows) of the data are not included in the average. Sub-framed images might
1311 not have dark columns included if the first column is > 15 in the original full-frame image
1312 coordinates.

1313 *5.2.3.2. Using Pre-flight Bias and Dark Current Model.* Pre-flight calibration data measured
1314 and modeled both bias and dark current charge accumulation as a function of temperature
1315 (§3.2.2; Figure 8). By dividing by the exposure time of the image to be calibrated, and using the
1316 known or inferred temperature of the CCD at the time of image acquisition and the model
1317 described in §3.2.2 and Figure 8, the dark current accumulation in DN/sec can be estimated and
1318 subtracted. The bias or DC offset component of the signal is assumed to be constant based on

1319 pre-flight data analysis and the typical temperatures of operation of the focal plane on Mars
1320 (Figures 7 and 8). The bias level is recorded in the DARK_LEVEL_CORRECTION keyword in
1321 the archived Mastcam PDS data label (§5.5), and has a typical value of 117 DN in Mastcam
1322 flight images acquired on Mars. This (commandable) bias level is usually subtracted from the
1323 data automatically by the DEA prior to companding, JPEG compression, and downlink of the
1324 data.

1325 **5.2.3.3. Manual Bias and Dark Current Subtraction.** Bias, at least, can always be subtracted
1326 using the value of the DARK_LEVEL_CORRECTION keyword in the archived Mastcam PDS
1327 data labels. If the dark current level cannot be estimated, however, either because dark pixels or
1328 focal plane array temperature data are not available for the specific image in question, then a
1329 more manual approach to dark current removal is attempted by the data reduction pipeline. This
1330 involves using the dark current estimated from either an image close in time from the other
1331 Mastcam camera (if that other camera was also active simultaneously or close in time, and the
1332 images from that camera contain the required dark pixel or temperature data); or from an image
1333 close in time from the same camera that *does* contain the required dark pixel or temperature data.
1334 "Close in time" is rather subjective, but a general metric, based on analysis of data in flight, is
1335 that it should be less than about 30 minutes so that the temperature of the analogous observation
1336 is likely to be close to that of the observation that it is designed to calibrate. If dark current
1337 cannot be estimated manually, then only bias is subtracted from the image.

1338 **5.2.4. Electronic Shutter Removal.**

1339 The effects of CCD electronic shutter smear (§3.2.3) are not currently being removed from
1340 any of the initial PDS archived Mastcam images. Future enhancements to the pipeline that could
1341 accommodate an *a posteriori* smear correction in the flight data are described in §5.3.3.

1342 **5.2.5 Flatfielding.**

1343 As described in §3.2.5, the brightness response recorded by the Mastcam detectors is not
1344 uniform as a function of position within the fields of view. In addition to pixel-to-pixel
1345 responsivity variations of the CCD, there are several geometric effects that influence the
1346 responsivity across the scene. For example, the Mastcam full fields of view are vignetted in their
1347 corners by a filter wheel mask (Figure 9; the intention of the design was to utilize just the central
1348 1200×1200 pixel science imaging field of the array (Figure 2), although in practice many times
1349 the full 1648×1200 span of the array is employed when a more rigorous quantitative radiance

1350 calibration is not required, in order to cover more of the scene in fewer mast pointing positions),
1351 and the Mastcams also display some structure under uniform illumination resulting from small
1352 internal reflections (*e.g.*, §3.2.5; Figure 9). Laboratory measurements during calibration (§3.2.5)
1353 provide measures of the non-uniformity of the cameras' responses. These calibrations are used to
1354 smooth out brightness variations in areas of lower or higher response. Normalized flatfield
1355 reference images for every Bayer filter and Science Filter combination (except for the solar/ND
1356 filters L7 and R7, for which no flatfield calibration data exist) were derived from pre-flight
1357 calibration data (§3.2.5) and are being used for current PDS-archived calibrated Mastcam images.
1358 These flatfield files are also archived in the PDS (for example, at [http://pds-](http://pds-imaging.jpl.nasa.gov/data/msl/MSLMST_0001/CALIB)
1359 [imaging.jpl.nasa.gov/data/msl/MSLMST_0001/CALIB](http://pds-imaging.jpl.nasa.gov/data/msl/MSLMST_0001/CALIB)). Mathematically, the flatfield files are
1360 stored as 1/flat, so correction is multiplicative during processing in the data reduction pipeline. If
1361 the image is a sensor subset, then the flatfield reference file is subframed accordingly, and if the
1362 image is a thumbnail, then a downsampled flatfield that is 1/64th of the full-resolution flatfield is
1363 used instead.

1364 5.2.6. Correction of Dead/Bad Pixels.

1365 The initial Mastcam data reduction and calibration pipeline for PDS archive products does not
1366 perform any corrections for known anomalous (dead or otherwise bad) pixels on the CCDs
1367 (§3.2.10), as the correction provided by the multiplicative flat field is deemed adequate, and the
1368 number of bad pixels is so small. Future enhancements to the pipeline that will accommodate
1369 these cases are described in §5.3.2.

1370 5.2.7. Initial Radiometric Calibration.

1371 Decompanded, bias and dark current subtracted, and flatfielded Mastcam images are
1372 converted to an initial estimate of radiance factor or I/F , where I is equal to the measured scene
1373 radiance, and πF is equal to the solar irradiance at the top of the Martian atmosphere at the time
1374 of the observation, convolved to the particular Mastcam bandpass being calibrated.
1375 Mathematically, the calibration to I/F in the initial PDS-archived "DRXX" format RDRs (Table
1376 12; Appendix D) is defined as the ratio of the observed calibrated DN level (DN_{obs}) to the
1377 expected DN level (DN_{exp}) that would be produced by imaging a perfectly diffuse white surface,
1378 illuminated by sunlight, at the heliocentric distance of Mars, with no atmospheric attenuation, at
1379 zero incidence angle, and with a reference exposure time of 10 msec. Reference solar DN levels
1380 (F_{ref}) at the perihelion distance of Mars (1.38 AU) are listed in Table 2. Note that the narrowband

1381 signal levels are computed for the dominant Bayer filter color in cases where the Bayer filters are
 1382 not uniformly transmitting (Figure 3; Table 2). For example, for the L1 and R1 527 nm filters,
 1383 the green Bayer position is used. To compute DN_{exp} for an image with an exposure time of t_{exp}
 1384 msec and acquired at a solar distance of d_{Sun} AU, we use the following expression:

$$1385 \quad 1386 \quad 1387 \quad DN_{exp} = F_{ref} \cdot (t_{exp} / 10) \cdot (1.38 / d_{Sun})^2 \quad (11).$$

1388 The derived I/F values archived in the DRXX format Mastcam RDRs are then simply
 1389 calculated as DN_{obs} / DN_{exp} . Archived Mastcam I/F calibrated data are stored in the PDS as 16-bit
 1390 integers in the "DRXX" format files (Table 13); conversion to floating point I/F values can be
 1391 performed by multiplying the stored 16-bit values by the constants in the PDS Label keyword
 1392 "RADIANCE_SCALING_FACTOR" and then adding the constants in the PDS label keyword
 1393 "RADIANCE_OFFSET."

1394 Users who want to derive an estimate of the absolute spectral radiance of the Version 1
 1395 calibrated Mastcam images (I_{obs} , for example in $W/m^2/nm/sr$) can simply multiply the I/F values
 1396 archived in the PDS calibrated images $[(I/F)_{PDS}]$ by the weighted value of the solar spectral
 1397 irradiance in that bandpass at the top of the Martian atmosphere at Mars perihelion (F_{Sun}), scaled
 1398 for the heliocentric distance d_{Sun} in AU at the time of the observation, and then dividing by π :

$$1399 \quad 1400 \quad 1401 \quad I_{obs} = (I/F)_{PDS} \cdot F_{Sun} \cdot [(1.38 / d_{Sun})^2] / \pi \quad (12).$$

1402 Reference solar spectral irradiance values (F_{Sun}) at the perihelion distance of Mars for each
 1403 Mastcam bandpass are also listed in Table 2.

1404 5.2.8. Color Correction.

1405 To approximate a "white balanced" color view of calibrated RGB Mastcam images, they are
 1406 linearly scaled by a set of coefficients developed from pre-flight testing. Specifically, the new
 1407 approximately white balanced R'G'B' color space is defined relative to the original calibrated
 1408 RGB color space as:

$$1409 \quad 1410 \quad \begin{matrix} R' \\ G' \\ B' \end{matrix} = \begin{bmatrix} 1.20 & 0 & 0 \\ 0 & 1.00 & 0 \\ 0 & 0 & 1.26 \end{bmatrix} \begin{bmatrix} R \\ G \\ B \end{bmatrix} \quad (13).$$

1411

1412 These coefficients were derived from pre-flight Mastcam imaging of a Macbeth color
1413 calibration target under terrestrial solar illumination at approximately solar noon. The
1414 transformation is performed on the calibrated 11-bit pixel values, which are then companded to 8
1415 bits using the companding lookup table 0 defined in Appendix B, to create the "DRCX" and
1416 "DRCL" format Mastcam RDRs archived in the PDS (Table 13).

1417 [5.2.9. Geometric Linearization for Mosaicking and Map Projection.](#)

1418 A *linearized* image is one from which the effects of lens distortion have been removed and
1419 slight deviations of each pixel from square have been adjusted. The processing involves warping
1420 the image pixels to show how the scene would appear if imaged by an ideal camera that has no
1421 distortion. The resulting image can be modeled using a simple pinhole camera model or,
1422 equivalently, a CAHV or CAHVOR camera model.

1423 The 4-vector Mastcam CAHV camera model described above (§3.3.1) is directly applied to
1424 Mastcam images to produce the geometrically linearized RDR products presently being archived
1425 in the PDS. The distortion is removed by inverting the nonlinear equation using an iterative
1426 procedure such as Newton's method. First, we determine the size of the linearized image by
1427 projecting points along the edge (we use the four corners and four midpoints) onto the focal
1428 plane. The limits of the projection are used to set the frame size for the new image. A detector is
1429 defined having square pixels with the nominal pixel pitch and principal point as the original
1430 image. The value for each pixel in the linearized image is calculated by projecting the center of
1431 each pixel onto the focal plane, applying the radial distortion model, and transferring the position
1432 to a fractional pixel location in the original image. Bi-cubic interpolation is then used to calculate
1433 the actual value. Some of the pixels in the linearized image will project outside of the original
1434 image and must be given a missing data value. This value is defined by the
1435 MISSING_CONSTANT keyword in the archived PDS data product label.

1436 In the associated PDS image label (.LBL) files for linearized "DRLX" and "DRCL" RDR
1437 products (Table 13), the camera model parameters used to linearize the image are reported as a
1438 4-vector CAHV model in the GEOMETRIC_CAMERA_MODEL_PARAMS group within the
1439 PDS label. For calibrated but non-linearized archived Mastcam images (in "DRXX" and
1440 "DRCX" images; Table 13), the full six-vector CAHVOR model parameters described above
1441 (§3.3.2) are reported in the PDS image label so that users can linearize those images themselves

1442 using those parameters, if desired.

1443 **5.3. Enhancements to the Initial Mastcam Data Reduction and Calibration Pipeline.**

1444 Figure 22 describes a modified version of the initial tactical-timescale Mastcam data
1445 calibration flow chart that takes advantage of new test and calibration data acquired in-flight on
1446 Mars, as well as more detailed analyses of pre-flight calibration data sets.

1447 **5.3.1. Improved Bayer pattern decompression/interpolation methods.**

1448 Raw or losslessly-compressed Mastcam images stored in the DEA are not debayered onboard
1449 the rover, and thus they still contain the RGB mosaic pattern generated from the Bayer color
1450 filter array built onto the sensor (Figure 20). This means that for data downlinked in raw or
1451 lossless form, users have the ability to choose which debayering algorithm to use during
1452 calibration and analysis. As described in §5.2.1 above, the default debayering method to produce
1453 interpolated color JPEG products archived in the PDS is the algorithm developed by Malvar *et al.*
1454 (2004), known as Improved Linear Interpolation (ILI), or Malvar-He-Cutler demosaicing. We
1455 have also experimented with simple bilinear interpolation and Directional Linear Minimum
1456 Mean Square-Error Estimation [DLMMSE, also known as Zhang-Wu demosaicing (Zhang &
1457 Wu, 2005)] algorithms. Examples for a typical Mastcam image are shown in Figure 23.

1458 Each demosaicing algorithm has its own benefits as well as its own set of introduced image
1459 artifacts. Bilinear interpolation (Figure 23b) looks the worst due to the reduced sharpness of the
1460 image, but it is exceptionally fast and thus could be the default choice in interactive tools where
1461 demosaicing needs to be done in real time. The default ILI algorithm (Figure 23c) offers
1462 improved sharpness and is a good default choice for non-interactive situations to maintain
1463 consistency with the compressed JPEG images that have been demosaiced onboard the rover.
1464 The ILI algorithm, however, can introduce color related artifacts in some cases. The DLMMSE
1465 algorithm (Figure 23d) was introduced as an alternative to ILI to avoid introducing color related
1466 artifacts, although it can introduce its own pixelated or crosshatch-type artifacts in some cases.
1467 When interpreting fine scale image features (such as stratigraphic layering, or sharp albedo
1468 boundaries) from an imaging sensor with an attached color filter array it is critical to realize that
1469 any demosaicing algorithm can introduce potential artifacts. Evaluating such features with
1470 different algorithms is prudent, then, to produce the highest-quality representation of the original
1471 scene.

1472 5.3.2. Correction of Saturated or Hot/Bad Pixels.

1473 There are many sources of potentially large localized pixel-to-pixel response variations. For
1474 example, some pixels may have saturated in the original image acquisition. We define
1475 "saturation" in the enhanced Mastcam data calibration pipeline as signal levels above the known
1476 linear range, which is ~ 1800 raw DN (240 DN when compacted to 8-bit data; see §3.2.1). When
1477 such high pixel values are encountered in raw Mastcam images, we flag them as saturated and
1478 replace their value in our pipeline processing with the value of the MISSING_CONSTANT
1479 keyword stored in their calibrated file labels. MISSING_CONSTANT is set to a negative value
1480 significantly below the minimum value of the valid data in the calibrated data file. Negative pixel
1481 values of MISSING_CONSTANT result in easy to identify values to ignore in calibrated data, as
1482 negative radiance or *I/F* values otherwise almost never occur within the calibrated Mastcam data
1483 set.

1484 Another source of potentially-large pixel-to-pixel variations are non-uniformities in the
1485 sensitivity of the individual pixel photosites. These were mapped by the detector manufacturer,
1486 and characterized during calibration (§3.2.10; Table 6). These are typically single pixels that are
1487 "hot" (more sensitive, and hence brighter) or "cold" (less sensitive, and darker than their
1488 neighbors). Yet another source of localized pixel response variations is contamination on the
1489 detector or optics. Such contamination occults light, creating umbral or penumbral shadowing
1490 and so-called "gray" pixel regions, usually a few pixels in size. These were also mapped during
1491 calibration (§3.2.10; Table 6), and are monitored to make sure they do not migrate with time.

1492 The final potential source of non-uniform pixel response that we consider here is radiation
1493 damage, from solar and galactic cosmic rays as well as local sources on the vehicle. Specifically,
1494 the MSL spacecraft has two energetic particle sources: the Radioisotope Thermoelectric
1495 Generator (RTG) (a constant source of low flux neutrons), and the Dynamic Albedo of Neutrons
1496 (DAN) experiment that includes an active, pulsed neutron generator. Radiation-induced pixel
1497 responses are both brighter and darker than their neighbors. Some of the problem pixels can self-
1498 heal, while others become long lived. Dark current images in cruise (§4.1) and on Mars (§4.2.1)
1499 provide some insight into the nature of such problematic pixels, which can be monitored over
1500 time.

1501 While the enhanced calibration pipeline flags and effectively removes saturated pixels from
1502 being improperly interpreted in calibrated data, we do not flag or replace hot, cold, or gray pixels.

1503 Rather, we monitor them with time, and attempt to make data users aware of known problematic
1504 pixels in both cameras (Table 6), so as to avoid their improper interpretation. Improvements to
1505 the calibration pipeline could involve proactively replacing these pixels with the median of their
1506 surroundings, for example.

1507 5.3.3. Improved Electronic Shutter Smear Removal.

1508 Currently, the only way to remove the effects of electronic shutter smear from Mastcam
1509 images is to acquire and subtract a near-simultaneous zero-second exposure from the non-zero
1510 exposure to be corrected. Unfortunately, acquiring such accompanying zero-second exposures is
1511 not part of the standard data acquisition sequence for Mastcam imaging (it would double the data
1512 volume of an observation because there is no way to do the zero-second subtraction onboard),
1513 and so this is generally not possible to implement with the flight data from Mars. Fortunately, the
1514 effects of shutter smear represent only a small and often insignificant noise source in most
1515 Mastcam images (§3.2.3). If a zero-second exposure was acquired and downlinked immediately
1516 before or after a non-zero exposure image of the same scene, then that zero-second image is
1517 subtracted from the non-zero image in the enhanced Mastcam data reduction pipeline to
1518 completely remove the effect of electronic shutter smear. If a zero-exposure image is not
1519 available (as is typically the case), and if the exposure time is less than ~6 msec, then an
1520 empirical electronic shutter smear correction algorithm might be needed to estimate and remove
1521 the electronic shutter smear from the image. An *a posteriori* model to remove, or at least to
1522 mitigate, the effect of smear from Mastcam images could be devised using a combination of (a)
1523 pre-flight Mastcam smear test images; (b) pre-flight MAHLI (which uses the same kind of CCD
1524 and readout process as the Mastcams; Edgett *et al.*, 2012; 2015) smear calibration observations,
1525 which are archived in the NASA/PDS with other archived MAHLI calibration data sets (see
1526 Edgett *et al.*, 2015); (c) the in-flight Mastcam shutter smear test images from *Curiosity* sols 36
1527 and 38; and/or (d) a deeper analysis of the specific clocking and physical architecture of the
1528 KAI-2020 CCD (Eastman Kodak, 2009; Truesense, 2012). For example, a typical deterministic
1529 procedure to implement this correction is to linearly subtract a percentage of the scene signal
1530 from rows "downstream" in the readout process, to analytically remove the smear component
1531 (*e.g.*, Bell *et al.*, 2003). That is, the scene itself can be used to estimate the accumulated effect of
1532 shutter smear, and to subtract that accumulation from the final image. Future refinements to the
1533 Mastcam calibration pipeline will explore implementing such a smear correction model for the

1534 small fraction of images that might benefit from this additional correction.

1535 [5.3.4. Improved Flatfielding.](#)

1536 Occasional daytime observations of the Martian sky in the anti-sunward direction have been
1537 used in flight to acquire additional, higher-fidelity data on the flatfield behavior (and its time
1538 variations) of the Mastcam optical system (§4.2.3). These "sky flat" calibration files are
1539 incorporated into the refined Mastcam calibration pipeline (Figure 22), as time-variable updates
1540 to the Mastcam flatfield files. For example, a second sky flat data set was acquired on sol 320
1541 (sequence mcam01052, at 14:30 LMST). The images were acquired with the Sun at 64°
1542 elevation, centered on the anti-Sun azimuth, and at 30° elevation, during a time when the optical
1543 depth was 0.87. The sequence acquired images with the same geometry as the previous sky flat
1544 sequences, yet reveal small differences compared to the sol 36-38 sky flat images, presumably
1545 due to small variations in the pattern and thickness of minor dust deposition on the front window
1546 of the Mastcam optics. Additional sky flat monitoring sequences are being acquired over time
1547 (*e.g.*, mcam06606 on sol 1356), and are being used to continually update the flatfield correction
1548 files in the refined Mastcam calibration pipeline.

1549 [5.3.5. Improved Radiance Calibration.](#)

1550 The initially-archived "Version 1" radiance-calibrated Mastcam RDRs are being calibrated
1551 using radiance coefficients based on a component-level model of the CCD QE, filter bandpass
1552 response, and optics transmissivity (Caplinger, 2013). However, using the radiance coefficients
1553 estimated from the pre-flight testing described in §3.2.6 (Table 4), which have been validated or
1554 amended based on the in-flight sky modeling work described in §4.2.4 and Table 11, a better
1555 "Version 2" estimate of the radiance on sensor can be calculated from decompressed, bias and
1556 dark current subtracted, and flatfielded Mastcam images, since those coefficients are based on
1557 the actual as-built system-level performance of the cameras. Work is under way to archive these
1558 Version 2 high-level Mastcam RDR data products, along with their associated ancillary
1559 calibration files and information, in the PDS.

1560 [5.3.6. Enhanced Radiance Factor \(I/F\) Calibration using the Mastcam Calibration Target.](#)

1561 Mastcam images can be converted from units of radiance to radiance factor (I/F ; equal to π
1562 times the bidirectional reflectance) by comparison with near-simultaneous images of the
1563 Mastcam calibration target (caltarget). The caltarget is mounted on the rover deck behind the
1564 remote sensing mast and on the same (right) side of the rover (Figure 4). The enhanced Mastcam

1565 *I/F* calibration process is generally similar to that used for the *I/F* calibration of the *Spirit* and
1566 *Opportunity* rover Pancam images (Bell *et al.*, 2006). The presence of airfall dust on the caltarget
1567 requires a procedure for dust correction, since caltarget reflectances are no longer perfectly
1568 known once appreciable amounts of dust have accumulated. Fortunately, the dust cover
1569 accumulating on the target has been thin enough during the mission to date to enable the variable
1570 reflectance properties of the different substrate calibration materials to still be visible under
1571 nominal illumination conditions in Mastcam images.

1572 Patches of seven spectrally distinct materials are mounted on the 8×8 cm caltarget base,
1573 organized into three grayscale rings (of approximately 20%, 40%, and 60% reflectance; Bell *et*
1574 *al.*, 2003), and four colored corner chips. Beneath the two brightest grayscale rings and
1575 underneath each of the four corner chips are six small "sweep magnets" (Madsen *et al.*, 2003;
1576 Bertelsen *et al.*, 2004). The magnetic force from each of these magnets produces a small region
1577 of highly reduced dust deposition on the caltarget surfaces just above the magnets.

1578 For each caltarget image, ROIs are selected for analysis by a calibration pipeline operator. The
1579 less dusty centers of the six magnets are selected, as are three regions of the grayscale rings away
1580 from the magnets. The reflectance calibration may be performed either by comparison with the
1581 six small, magnet centers (which offer a reduced dust layer at the cost of higher noise due to the
1582 low number of pixels) or using the three larger, non-magnetic regions of the grayscale rings that
1583 have more dust deposition, but better pixel statistics. Currently the dust correction and
1584 reflectance calibration is performed based on the three "nonmagnetic" regions, but this could
1585 change as dust continues to accumulate on the caltarget.

1586 Figure 24 shows an example of ROIs selected on a caltarget image acquired on sol 514
1587 through the Mastcam's L0 (Bayer-RGB) filter. The ROIs shown are for the three "nonmagnetic"
1588 regions of the caltarget rings. Figure 25 shows a plot of the radiances observed in the L3 (751
1589 nm) filter from the three regions as a function of the known (clean) reflectances (black squares)
1590 of those three materials (Bell *et al.*, 2003). If the reflectance values were good estimates, the
1591 three points would fall on a straight line through the origin, and the slope of this line would
1592 measure the incoming irradiance. The presence of dust reduces the contrast so that pre-flight
1593 measured reflectance values are no longer good estimates of actual caltarget reflectances, and the
1594 three points no longer fall on a line through the origin.

1595 The dust correction procedure fits the three points to an analytical two-layer scattering model
1596 based on the work of Hapke (1993; §9.D.2). The model treats single-scattering events in full
1597 detail and uses a two-stream formalism (*e.g.*, Zdunkowski *et al.*, 2007) to treat multiple-
1598 scattering events. The dust model and procedure follows very closely the one described in full
1599 detail in Kinch *et al.* (2015), the only difference is that we here do not distinguish between
1600 diffuse sky irradiance and solar (directional) irradiance; rather, all irradiance is assumed to come
1601 from the direction of the sun. The utility of this model for analysis of dusty caltarget surfaces
1602 was demonstrated by Johnson *et al.* (2006) in laboratory studies. A similar, but simpler, two-
1603 stream scattering model is currently used for dust correction on the Mars Exploration Rovers'
1604 Pancam (Kinch *et al.*, 2007), but work is ongoing to employ this more sophisticated model on
1605 that mission as well (Kinch *et al.*, 2015). Preliminary work on employing this dust model for the
1606 MSL Mastcam was presented in Kinch *et al.* (2013).

1607 In addition to the unknown incoming irradiance, the dust model as employed here adds one
1608 other free parameter to the fit. This is the extinction optical depth of the dust layer on the
1609 caltarget τ_{cal} , defined in the standard way so that for radiance J normally incident on the dusty
1610 caltarget, the radiance that reaches the underlying caltarget surface without interacting with the
1611 dust is $J \cdot \exp(-\tau_{cal})$. In addition, the dust single-scattering albedo must be specified. The gray
1612 circles in Figure 25 demonstrate the procedure. These points are placed at the best-fit
1613 reflectances of dusty caltarget surfaces as determined by the fit to the dust model. The results
1614 show that the expected linear relation between observed radiance and model reflectance now
1615 holds.

1616 The fit is performed independently for every single caltarget image, and thus the dust model
1617 derives both incoming irradiance and dust optical depth on the caltarget for every image. This
1618 history of dust deposition is shown for the L3 (751 nm) filter in Figure 26 and compared with the
1619 optical depths of dust in the atmosphere as observed through the Mastcam's 880 nm solar filter
1620 (L7). Figure 26 also shows derived incoming solar irradiances. These are shown relative to the
1621 known solar irradiance at the top of the atmosphere. The relative stability of these values is an
1622 indication that the value for dust single-scattering albedo employed in the model is adequate. If
1623 the dust was assumed to be too dark, the derived incoming irradiances would drift to higher
1624 values as the caltarget gets dustier, and vice versa for dust assumed to be too bright.

1625 **5.4. Examples: Accuracy and Precision of the Calibration.**

1626 **5.4.1. Example Morphologic Observations: Effects of Focus and Compression.**

1627 On *Curiosity* Sol 17, a 1-column \times 34-row Mastcam mosaic sequence (mcam00050) was
1628 acquired with very large image overlap (75%) along a near-vertical transect from the surface in
1629 front of the rover out to the slopes of Mt. Sharp on the horizon (Figure 27). These images were
1630 used to characterize the M-100 depth of field in flight; however, they also demonstrate the ability
1631 of Mastcam to acquire a set of images at different pointings that can then be combined (focus-
1632 merge product) via a “best-focus” algorithm to produce a completely in-focus image. The
1633 example images demonstrate how the depth of field increases with distance to the scene target
1634 (the furthest image shows most of Mt. Sharp and the far-field in focus, while the closer images
1635 are most in-focus near the middle of the scene and are less in-focus at the closest and furthest
1636 distances.

1637 On Sol 193, an 8-image M-100 "z-stack" sequence (mcam01026) was commanded on a
1638 laterally extensive outcrop near the region known as "Gillespie." A z-stack is a set of images
1639 acquired at a fixed pointing but with changing focus stepping through the scene's depth of field.
1640 Flight software within the Mastcam DEA processes the images into a resulting focus merge that
1641 preserves the best-focused parts of each original input image (see §7.6 in Edgett *et al.*, 2012 for
1642 details). The full set of 8 images at different focus positions was not downlinked, but the
1643 resulting onboard-calculated focus-merge product was (Figure 28). Only the final merged z-stack
1644 image needs to be downlinked initially, and if individual z-stack images are requested by the
1645 science team they can be downlinked at a later date. This reduces downlinked data, with a
1646 minimal impact to operational time. While only used rarely for Mastcam imaging so far in
1647 *Curiosity's* mission, z-stacking has been used frequently for micro-scale imaging by the MAHLI.

1648 Figure 29 shows a specific qualitative example, from M-34 imaging on *Curiosity* sol 1155, of
1649 the quantitative performance of the Mastcam JPEG compressor described in §4.2.6 and Figure
1650 18. Images at relatively high JPEG quality factors are generally indistinguishable from
1651 losslessly-compressed images for most scenes imaged by Mastcam. However, some scenes with
1652 high-frequency features like layers or lamination show JPEG compression artifacts even at
1653 relatively high JPEG quality factors. The MSL science team and the Mastcam operations team
1654 actively identify images with JPEG artifacts that could negatively impact the robust scientific

1655 analysis of the data. Such images are often flagged for potential lossless retransmission, if and
1656 when downlink resources allow, before the original onboard image is scheduled for deletion.

1657 In an even more extreme example, on Sol 943 several sets of M-34 sky images were acquired
1658 in sequence mcam04146 to search for clouds. This sky imaging was originally downlinked at
1659 compression 35 but was brought back losslessly to discern any thin cloud layers. As seen in
1660 Figure 30, the original (JPEG 35) images show the deleterious effects of heavy compression on
1661 scenes with little variability. This effect is completely removed in the losslessly compressed
1662 version.

1663 5.4.2. Example Stereo Products.

1664 Even though the two Mastcams have a factor of 3 difference in focal length, it is still
1665 straightforward to acquire near-simultaneous stereo pair images. Due to the stereo baseline and
1666 toe-in of the cameras, the area of the M-34 field of view also covered by the narrower M-100
1667 field of view is restricted to a horizontal band in the center 1/3rd of the M-34 sensor. The
1668 simultaneous M-100 field's placement within that horizontal band is dependent on the distance to
1669 the target, with closer M-100 targets appearing on the right side of the M-34 field of view and
1670 distant M-100 targets appearing in the left side (Figure 31). To simplify sequencing when
1671 acquiring stereo mosaics, M-34 images can be subframed vertically to exclude the top 1/3rd and
1672 bottom 1/3rd of the field of view, as well as subframed horizontally to exclude columns outside
1673 of the area covered by M-100 targets at distances from 1.9 m to infinity. The process is
1674 informally known as "shrink-wrap stereo", and the resulting M-34 frame size is 1152 pixels
1675 across by 432 pixels high, roughly centered in the sensor. This reduces the data volume of the M-
1676 34 to ~32% of a normal full frame.

1677 Figure 31 also shows some additional dramatic examples of both near-field and far-field
1678 Mastcam stereo anaglyphs. The near-field view is a color stereo red-blue anaglyph rendering of a
1679 single sol 39 Mastcam left-right stereo pair of the Bradbury Plains conglomerate target named
1680 "Hottah," from sequences mcam00177 and mcam00178. The mid- and far-field view is from a
1681 sol 938 mosaic using Mastcam sequence mcam04119 that covered a mid-field ridge called
1682 "Salsberry Peak" and the far-field lower slopes of Mt. Sharp.

1683 5.4.3. Sky/Astronomical Imaging Examples.

1684 The Mastcams have been used to acquire a variety of daytime and nighttime sky images that
1685 have been designed to achieve specific atmospheric science, meteorological, and astronomical

1686 objectives (Malin *et al.*, 2017). The most common sky imaging observations have been relatively
1687 frequent direct solar images using the Mastcam L7 and R7 solar neutral-density-coated filters
1688 (Lemmon, 2014), timed to characterize the history of atmospheric dust opacity in Gale crater as
1689 compared to the long-term record of opacity derived from similar kinds of direct solar imaging
1690 from other rover and lander sites (Lemmon *et al.*, 2015). Additional sky imaging observations
1691 have included time-lapse observations of sunsets to characterize haze layers in the lower
1692 atmosphere above Gale crater (Figure 32a; NASA, 2015); time-lapse and video mode Mastcam
1693 observations of transits (annular solar eclipses) of Phobos across the Sun's disk (Figure 32c;
1694 NASA, 2013a) and nighttime time-lapse imaging of an occultation of Deimos by Phobos (Figure
1695 32b; NASA, 2013b; Lemmon *et al.*, 2013; Lemmon, 2015), all designed to help refine the
1696 (slowly evolving) orbital parameters of both moons; twilight and nighttime imaging of the Earth
1697 and the Moon, Ceres, Vesta, and Deimos designed to search for evidence of nighttime clouds or
1698 hazes in the atmosphere; daytime imaging of sunspots and a rare transit of Mercury as seen from
1699 Mars (NASA, 2014), partially designed to help monitor sunspot activity in support of other solar
1700 monitoring spacecraft; and nighttime observations of the close encounter of comet C/2013 A1
1701 (Siding Spring) with Mars in October 2014 (Lemmon *et al.*, 2014).

1702 5.4.4. Quantitative Radiance Factor Multispectral Observations.

1703 Mastcam has acquired several hundred multispectral sequences at the time of this writing,
1704 making use of the narrow-band science filters on each camera to characterize the visible to near-
1705 infrared reflectance properties of rocks, soils, and other materials encountered by the rover. Due
1706 to the spectral influence of reddish dust, multispectral observations frequently target relatively
1707 cleaner surfaces, which may be undisturbed materials with less dusty rock faces but also include
1708 surfaces brushed, drilled, or otherwise disturbed by the rover. Example reflectance spectra from
1709 sol 762 (the "Confidence Hills" drill site) which have been calibrated to I/F by the methods
1710 described in §5.3.6 are shown in Figure 33. Spectra from the drill tailings and the surface
1711 brushed by the Dust Removal Tool (DRT) show a strong absorption feature near the 527 nm
1712 filter compared with nearby dust and soil spectra, consistent with an enrichment in hematite. A
1713 variety of different spectral shapes and absorption features have been observed in reflectance
1714 spectra from other multispectral observations acquired along the traverse (*e.g.*, Wellington *et al.*,
1715 2016).

1716 **5.5. Data Products and PDS Archiving.**

1717 The Mastcam cameras and their DEAs create, store, and transmit to the rover's computer
1718 single images or video groups of images that are encoded in five basic formats: raster 8-bit per
1719 pixel, raster 16-bit per pixel, losslessly-compressed (first difference Huffman encoded) 8-bit,
1720 JPEG grayscale, or JPEG color (Table 3). Other kinds of images generated by onboard
1721 processing in the Mastcam DEAs (*i.e.*, focus merges, range maps, and 1/64th sampled thumbnails
1722 of full resolution images) are also encoded in these same formats. Additional details on the
1723 specific nature of these raw data products, which are eventually downlinked to Earth and
1724 archived in the NASA PDS as raw Mastcam EDRs, can be found in the Mastcam Software
1725 Interface Specification (SIS) document (Malin *et al.*, 2013).

1726 Raw and calibrated Mastcam image products are currently being delivered to the PDS
1727 Imaging Node archives in five forms, depending on their level of calibration, if any (Table 13).
1728 Unprocessed image data are in CODMAC Level 2 form (Appendix C). These data are delivered
1729 to the PDS as files suffixed with XXXX.DAT. Details of the raw data records in a .DAT file are
1730 documented in §4.4.3 and §4.4.5 of the Mastcam SIS (Malin *et al.*, 2013). Software to extract
1731 and decompress all 21 Mastcam EDR data products (Table 3) from raw PDS-archived .DAT files
1732 is provided as part of the PDS archive distribution (for example, at [http://pds-
1733 imaging.jpl.nasa.gov/data/msl/MSLMST_0001/SOFTWARE/](http://pds-imaging.jpl.nasa.gov/data/msl/MSLMST_0001/SOFTWARE/)). The four derivative forms of
1734 processed Mastcam data products (Table 13) are archived in a format recognized by the PDS for
1735 representation of image data, and suffixed with ".IMG". These Mastcam images have associated
1736 detached labels in the PDS3 ODL standard, with the same filenames but suffixed with ".LBL".
1737 Details of the file naming scheme used for PDS archived Mastcam images are provided in
1738 Appendix D. There are 21 file types (Table 3) and five kinds of delivery products (Table 13)
1739 possible in the Mastcam PDS archive. Thus, a total of 105 types of archived files is possible.
1740 However, as described in §4.5 of the Mastcam SIS (Malin *et al.*, 2013), only 93 of these 105
1741 possible products are actually being archived in the PDS. Details on the definitions and valid
1742 values of the Mastcam PDS label keywords, as well as example Mastcam PDS label file entries,
1743 are provided in Appendix A of Malin *et al.* (2013).

1744 **6. Future Work and Lessons Learned**

1745 The Mars Science Laboratory Mastcam investigation has been a phenomenal success and has
1746 played an important role in the discoveries made by *Curiosity* to date. Still, significant
1747 improvements to the calibration of the cameras are in the works, and more are being envisioned,
1748 for the future. For example, as described above, opportunities exist to further increase the fidelity
1749 of the calibration by completing the development of a rigorous shutter smear subtraction routine,
1750 which will be especially important for images taken with very short (several msec) exposure
1751 times. Proactively flagging or replacing hot, cold, or gray pixels could be implemented in a
1752 future version of the pipeline, or at least for images where the best possible analysis of small-
1753 scale, high-frequency pixel-to-pixel variations could be deemed important. Finally, additional in-
1754 flight monitoring of the performance of the Mastcams during *Curiosity's* continuing mission will
1755 result in the collection of additional in-flight assessments of CCD bias and dark current, as well
1756 as the flatfield performance of the detectors and optics, over time. Building those occasional
1757 monitoring update files into an evolving time-dependent calibration pipeline is an important part
1758 of any long-duration flight mission.

1759 Many kinds of scientific analyses of Mastcam data require detailed quantitative image
1760 processing and modeling, and thus rely on a robust and reliable calibration. Testing and
1761 calibration of the MSL Mastcam instruments took advantage of previous pre-flight and in-flight
1762 test and calibration programs for other Mars imagers (*e.g.*, Reid *et al.*, 1999; Bell *et al.*, 2003,
1763 2006) as well as the experience gained by MSSS staff and science collaborators in their
1764 successful design, fabrication, and testing of more than a dozen other previous flight cameras. In
1765 a similar vein, the MSL Mastcam design, fabrication, test, calibration, and operations experience
1766 can provide guidance and lessons-learned for similar work to be conducted on other future Mars
1767 and planetary imaging investigations. For example, much of the test equipment, procedures, and
1768 data processing algorithms used for Mastcam calibration will be directly applicable to the testing
1769 and calibration of the closely-related Mastcam-Z imaging system on the NASA Mars 2020 rover
1770 (Bell *et al.*, 2014). Mastcam-Z is a pair of ~3:1 zoom cameras that directly inherit much of the
1771 CCD, electronics, and other mechanisms (filter wheel, focus) from MSL Mastcam, and thus that
1772 team will leverage much of the process and experience described here. For example, the
1773 Mastcam-Z team is already planning to conduct additional pre-flight thermal vacuum testing of
1774 the geometric properties of the cameras over a wide range of expected Mars operating

1775 temperatures, going beyond the testing that was done for the Mastcams based on experience with
1776 thermal variations in the geometric properties of the cameras observed on Mars (*e.g.*, §4.2.5).
1777 Other examples of lessons learned include the intention to perform more robust assessments of
1778 the in-band and out-of-band performance of the multispectral filters (§3.2.4) in order to increase
1779 the accuracy of the radiometric calibration; re-design of the Mastcam calibration target to better
1780 anticipate the effects of airfall (or landing-induced) dust on the target (§4.3; §5.3.6); and closer
1781 coordination with other imagers on the Mars 2020 rover in order to try to arrive at a more
1782 uniform format for file naming, file labels, and archive formats across the vehicle.

1783

1784 **7. Summary**

1785 This paper describes the pre-flight and in-flight calibration of the Mars Science Laboratory
1786 *Curiosity* rover's Mastcam fixed focal length, multispectral, stereoscopic imaging system (Malin
1787 *et al.*, 2017), enabling the conversion of DN values downlinked from Mars into reliable estimates
1788 of physical quantities like absolute radiance and radiance factor, or I/F . Pre-flight and in-flight
1789 corrections and models have been developed to perform corrections for CCD, optics/filters, and
1790 geometric effects, and to validate the calibration by comparing our derived estimates of radiance
1791 or radiance factor with those from known or assumed standards. The absolute radiometric
1792 accuracy and filter-to-filter precision of calibrated images meets or exceeds the $\pm 10\%$ and $\pm 7\%$
1793 requirements, respectively, except for the narrowband blue (445 nm) filters, which were not as
1794 well characterized prior to launch.

1795 We also describe the tactical and strategically-refined Mastcam data reduction and calibration
1796 pipelines. The latter include improvements in Bayer filter interpolation, flatfielding, and radiance
1797 and relative reflectance (I/F) calibrations. As validation of the pipeline processing described here,
1798 we also show some examples of science results related to calibration and processing of scenes
1799 with wide variations in focus and compression parameters, stereo imaging, sky/astronomical
1800 object imaging, and narrowband multispectral data sets. Finally, we describe a variety of details
1801 regarding Mastcam file naming, file formats, headers/labels, and PDS archiving that should
1802 prove useful to end users of the Mastcam images.

1803 **8. Acknowledgements**

1804 We are indebted to the incredibly talented men and women of NASA, JPL/Caltech, and many
1805 other government labs and companies who helped to design, build, and deliver *Curiosity* to Mars,
1806 and thus to enable the success of the Mastcam investigation. We also acknowledge the broader
1807 Mastcam, MAHLI, and MARDI Development and Operations team at Malin Space Science
1808 Systems, Inc., for their skill, perseverance, and outstanding attention to quality and detail in the
1809 pre-flight testing and sol-to-sol operations of the cameras on Mars. We thank Peter Smith,
1810 Rebecca Greenberger, Ken Edmundson, and Janet Richie for patient and thoughtful reviews and
1811 suggestions on an earlier draft of this paper. We acknowledge ASU student helpers Matt Jungers,
1812 Julie Mitchell, and Hannah Kerner for assistance with Mastcam calibration pipeline development
1813 and data processing. This work was funded by grants and contracts from NASA, JPL/Caltech,
1814 and MSSS. The data used here are listed in the references, tables, Appendices, and/or the NASA
1815 Planetary Data System Imaging Node at, for example, [http://pds-
1817 imaging.jpl.nasa.gov/data/msl/MSLMST_0001/CALIB/](http://pds-
1816 imaging.jpl.nasa.gov/data/msl/MSLMST_0001/CALIB/) and
http://pds-imaging.jpl.nasa.gov/data/msl/MSLMST_0001/SOFTWARE/.

1818

1819

1820 9. Appendix A: Camera Model Transformations

1821

1822 Rotations are expressed using unit quaternions, which are 4-tuples in the form:

$$1823 (s, v_x, v_y, v_z) = (s, \vec{V}) = \left(\cos \frac{\theta}{2}, \vec{A}_x \sin \frac{\theta}{2}, \vec{A}_y \sin \frac{\theta}{2}, \vec{A}_z \sin \frac{\theta}{2} \right) \quad (A1)$$

1824 where \vec{A} is the unit-vector axis of rotation, θ is the angle of rotation, and the magnitude
 1825 (square root of the sum of each of the 4 elements squared) is 1. Multiplying two
 1826 quaternions composites their rotations (rotate by Q_2 first and then Q_1):

$$1827 Q_1 \times Q_2 = (s_1 s_2 - \vec{V}_1 \cdot \vec{V}_2, s_1 \vec{V}_2 + s_2 \vec{V}_1 + \vec{V}_1 \times \vec{V}_2) \quad (A2)$$

1828 which uses vector dot and cross products. Rotating a vector by a quaternion is then:

$$1829 Q \times \vec{V} = \text{vector}(Q \times (0, \vec{V}) \times Q') \quad (A3)$$

1830 where the central term builds a quaternion with scalar 0 and vector component V , Q' is the
 1831 quaternion inverse, which negates the vector component, and `vector()` returns the vector
 1832 part \vec{V} of the quaternion (simply discarding the scalar).

1833 The calibration camera models shown in (Table 8) were taken at a specific pose, defined
 1834 by **Pcal**, **Qcal** in (Table 9; which were themselves derived using the algorithm below). To
 1835 construct the new pose P, Q, we extract the ARTICULATION_DEVICE_ANGLE from the
 1836 RSM_ARTICULATION_STATE_PARAMS group in the PDS label. The first two elements are the
 1837 measured joint angles in the azimuth (`az_target`) and elevation (`el_target`) directions. These
 1838 are *not* azimuth and elevation, but are rather angles from the hard stop in the two
 1839 directions, which are nominally at azimuth 181 and elevation -91 degrees. Thus
 1840 `az_target=0` is (approximately) one degree past backward (toward the rear of the rover),
 1841 and `el_target=0` is (approximately) one degree past straight down.

1842 The following pseudocode creates the rotation quaternion using `az_target`, `el_target`, and
 1843 the boldface constants in (Table 9):

1844

```
1845 az_axis = normalize(az_axis) // to unit vector
```

```
1846 el_axis = normalize(el_axis)
```

```
1847 // Rotate around az_axis to align with az_home, el_home
```

```
1848 Quaternion axis_rot = Rotation(az_axis, (az_home - az_elaxis))
```

```
1849 Vector el_axis_rot = axis_rot × el_axis // Rotate a vector
```

```
1850 Vector el_point_rot = axis_rot × (el_point - az_point) + az_point
```

1851

```

1852 // Transform target angles they're 0 at home
1853 double az_angle = az_target - az_home
1854 double el_angle = el_target - el_home
1855
1856 // Compute reference point position Pr at home configuration
1857 Vector tmp1 = az_axis × el_axis_rot // Cross product
1858 Vector Pr = el_point_rot
1859 if (magnitude(tmp1) > epsilon) { // not parallel, safe
1860     double det = el_axis_rot · az_axis // dot product
1861     double alpha = (az_point - el_point_rot) · el_axis_rot +
1862         ((el_point_rot - az_point) · az_axis) * det
1863     alpha = alpha / (1.0 - det*det)
1864     Pr = el_point_rot + el_axis_rot * alpha
1865 }
1866 // Compute final point and rotation as composite of az and el
1867 Quaternion az_rot = Rotation(az_axis, az_angle)
1868 Vector P_rmech = az_rot × (Pr - az_point) + az_point
1869 Vector P = P_rmech + rmech_to_rnav // Final point, RNAV
1870 Quaternion el_rot = Rotation(el_axis_rot, el_angle)
1871 Quaternion Q = az_rot × el_rot // Final quaternion
1872

```

1873 Note that the kinematics algorithm works with the “Rover Mechanical” coordinate frame
1874 throughout, converting to “Rover Navigation” frame at the end. The calibration and final
1875 camera models are expressed in Rover Navigation frame. A more complete treatment of
1876 these and other MSL coordinate frames can be found in Alexander (2015), section 6.3.
1877 Conversion to “Local Level” or “Site” frames (which point north/down instead of relative to
1878 the rover) can be accomplished using the parameters in the
1879 ROVER_COORDINATE_SYSTEM_PARMS group in the PDS label.

1880 Finally, the camera model extrinsics must be transformed from P_{cal} , Q_{cal} to P , Q . To do
1881 this, we compute a composite transform that “un-rotates” by Q_{cal} and then rotates by Q :

$$1882 \quad Q_{rot} = Q \times Q'_{cal} \quad (A4)$$

1883 The CAHVOR vectors are then transformed as follows:

$$1884 \quad C' = Q_{rot} \times (C - P_{cal}) + P \quad (A5)$$

$$1885 \quad A' = Q_{rot} \times A \quad (A6)$$

$$1886 \quad H' = Q_{rot} \times H \quad (A7)$$

$$1887 \quad V' = Q_{rot} \times V \quad (A8)$$

$$1888 \quad O' = Q_{rot} \times O \quad (A9)$$

$$1889 \quad R' = R \quad (A10)$$

$$1890 \quad E' = E \quad (A11)$$

1891 The E vector is a part of CAHVORE models (Gennery, 2006) that are not used by Mastcam
1892 but is included here for completeness.

1893 For full-frame images, this is the final result. However, most Mastcam images are
1894 subframed, often to return only the “science imaging” area, and thumbnail images are
1895 additionally downsampled by a factor of 8. These operations affect the camera model as
1896 follows.

1897 The starting coordinate of a subframe is found in the IMAGE object in the PDS label. The
1898 FIRST_LINE keyword defines the line start (dy) and FIRST_LINE_SAMPLE defines the
1899 sample start (dx). Note that the number of lines or samples does not affect the camera
1900 model. The model is then transformed as follows:

$$1901 \quad H' = H - (dx - 1)A \quad (A12)$$

$$1902 \quad V' = V - (dy - 1)A \quad (A13)$$

1903 The -1 is because the PDS keywords start counting at 1, by definition. If there is no
1904 subframe, dx and dy are 1 and there is no modification. The other vectors are unchanged.

1905 Mastcam thumbnail images are downsampled by a factor of 8. This factor is in the
1906 PIXEL_AVERAGING_HEIGHT ($hscale$) and PIXEL_AVERAGING_WIDTH ($vscale$) keywords in
1907 the IMAGE_PARAMS group (which are always 8 for Mastcam thumbnails). Downsampling is
1908 accomplished via the following:

$$1909 \quad H' = H/hscale \quad (A14)$$

$$1910 \quad V' = V/vscale \quad (A15)$$

1911 which should be done after the subframe shift. To be technically correct, one additional
1912 step is needed to compensate for integer coordinates being in the center of a pixel: the H
1913 and V vectors must be shifted by -0.5 pixel before the scale and +0.5 pixel afterwards,
1914 making the full equations:

$$1915 \quad H' = (H + A/2)/hscale - A/2 \quad (A16)$$

$$1916 \quad V' = (V + A/2)/vscale - A/2 \quad (A17)$$

1917 However, as of this writing, the additional shift is not being performed by the Mastcam
1918 software, so the PDS labels reflect the simple scaling of [Equations A14 and A15](#) instead.

1919 **10. Appendix B: MSL/Mastcam Standard Companding (11 to 8**
 1920 **bit DN) and Decompanding (8 to 11 bit DN) "Lookup Table 0".**

1921
 1922

8 bit	11 bit														
0	0	32	46	64	150	96	316	128	542	160	829	192	1177	224	1586
1	2	33	48	65	154	97	322	129	550	161	839	193	1189	225	1600
2	3	34	50	66	159	98	328	130	558	162	849	194	1201	226	1614
3	3	35	53	67	163	99	334	131	566	163	859	195	1213	227	1628
4	4	36	55	68	168	100	341	132	575	164	869	196	1225	228	1642
5	5	37	58	69	172	101	347	133	583	165	880	197	1237	229	1656
6	5	38	61	70	177	102	354	134	591	166	890	198	1249	230	1670
7	6	39	63	71	181	103	360	135	600	167	900	199	1262	231	1684
8	7	40	66	72	186	104	367	136	608	168	911	200	1274	232	1698
9	8	41	69	73	191	105	373	137	617	169	921	201	1286	233	1712
10	9	42	72	74	196	106	380	138	626	170	932	202	1299	234	1727
11	10	43	75	75	201	107	387	139	634	171	942	203	1311	235	1741
12	11	44	78	76	206	108	394	140	643	172	953	204	1324	236	1755
13	12	45	81	77	211	109	401	141	652	173	964	205	1336	237	1770
14	14	46	84	78	216	110	408	142	661	174	974	206	1349	238	1784
15	15	47	87	79	221	111	415	143	670	175	985	207	1362	239	1799
16	16	48	90	80	226	112	422	144	679	176	996	208	1374	240	1814
17	18	49	94	81	231	113	429	145	688	177	1007	209	1387	241	1828
18	19	50	97	82	236	114	436	146	697	178	1018	210	1400	242	1843
19	20	51	100	83	241	115	443	147	706	179	1029	211	1413	243	1858
20	22	52	104	84	247	116	450	148	715	180	1040	212	1426	244	1873
21	24	53	107	85	252	117	458	149	724	181	1051	213	1439	245	1888
22	25	54	111	86	258	118	465	150	733	182	1062	214	1452	246	1903
23	27	55	115	87	263	119	472	151	743	183	1074	215	1465	247	1918
24	29	56	118	88	269	120	480	152	752	184	1085	216	1479	248	1933
25	31	57	122	89	274	121	487	153	761	185	1096	217	1492	249	1948
26	33	58	126	90	280	122	495	154	771	186	1108	218	1505	250	1963
27	35	59	130	91	286	123	503	155	781	187	1119	219	1519	251	1979
28	37	60	134	92	292	124	510	156	790	188	1131	220	1532	252	1994
29	39	61	138	93	298	125	518	157	800	189	1142	221	1545	253	2009
30	41	62	142	94	304	126	526	158	810	190	1154	222	1559	254	2025
31	43	63	146	95	310	127	534	159	819	191	1166	223	1573	255	2033

1923

1924

1925 **11. Appendix C: Committee on Data Management and**
 1926 **Computation (CODMAC, 1982) Processing Levels, and their**
 1927 **traditional NASA equivalents.**
 1928

CODMAC Level	NASA Level	Type	Description
1	Packet Data	Raw data	Telemetry data stream as received at the ground station, with science and engineering data embedded
2	0	Edited Data	Instrument science data (e.g., raw voltages, counts) at full resolution, time ordered, with duplicates and transmission errors removed
3	1-A	Calibrated Data	Level 0 data that have been located in space and may have been transformed (e.g., calibrated, rearranged) in a reversible manner and packaged with needed ancillary and auxiliary data (e.g., radiances with the calibration equations applied)
4	1-B	Resampled Data	Irreversibly transformed (e.g., resampled, remapped, calibrated) values of the instrument measurements (e.g., radiances, magnetic field strength)
5	2	Derived Data	Geophysical parameters, generally derived from Level 1 data, and located in space and time commensurate with instrument location, pointing, and sampling
5	3	Derived Data	Geophysical parameters mapped onto uniform space-time grids

1929

1930

1931

1932

1933 **12. Appendix D: Mastcam Archived PDS Data File Names**

1934

1935 Mastcam images archived in the NASA Planetary Data System (PDS) follow the file naming
1936 convention described here:

1937

1938 SSSSIIFFFFFFFLLLXXCCCCPGV_DXXX.ZZZ

1939

1940 where:

1941 SSSS: Four digit sol number after landing day (which was defined as sol 0)

1942 II: Two digit camera code: "ML"=Mastcam Left (M-34); "MR"=Mastcam Right (M-100)

1943 FFFFFFFF: Six digit sequence number identifier

1944 LLL: Three digit command number within the sequence that corresponds to this image

1945 XX: Two digit Camera Data Product Identifier (CDPID) counter that records the
1946 number of times this CDPID has been used over the lifetime of the mission

1947 CCCCC: Five digit CDPID value, uniquely assigned by the camera to an image product

1948 P: One letter product type (see Table 3)

1949 G: One letter Group of Pictures (GOP) hexadecimal counter, for video sequences

1950 V: One digit version number

1951 DXXX: Four letter data processing code (See Table 13)

1952 ZZZ: Three letter file extension (typically, "DAT" or "IMG")

1953

1954 The string "FFFFFFLLL" within the filename is also known as the Product Identifier, or a
1955 numerical identifier assigned to images when they are commanded from the ground. Depending
1956 on how the image was commanded, this number contains values related to the sequence used to
1957 command the image.

1958 The product identifier is useful to distinguish among groups of images commanded with the
1959 same imaging sequence, such as for a panorama, video, or multispectral observation.

1960 Additional details and examples of the Mastcam (as well as MAHLI and MARDI) file naming
1961 scheme can be found in §3.4.1 and Table 3.4-1 of Malin *et al.*, 2013.

1962 **13. References**

- 1963 Alexander, D., R. Deen, “Mars Science Laboratory Project Software Interface Specification
1964 (SIS): Camera & LIBS Experiment Data Record (EDR) and Reduced Data Record (RDR)
1965 Data Products”, Version 3.5, December 17, 2015. Online at [http://pds-
imaging.jpl.nasa.gov/data/msl/MSLNAV_0XXX/DOCUMENT/MSL_CAMERA_SIS.PDF](http://pds-
1966 imaging.jpl.nasa.gov/data/msl/MSLNAV_0XXX/DOCUMENT/MSL_CAMERA_SIS.PDF)
- 1967 Bell III, J.F. and W.T. Sullivan, "The MarsDial: A Sundial for the Red Planet," *The Planetary*
1968 *Report*, pp. 6-11, Jan./Feb. 2004.
- 1969 Bell III, J.F., S.W. Squyres, K.E. Herkenhoff, J.N. Maki, H.M. Arneson, D. Brown, S.A. Collins,
1970 A. Dingizian, S.T. Elliot, E.C. Hagerott, A.G. Hayes, M.J. Johnson, J.R. Johnson, J. Joseph, K.
1971 Kinch, M.T. Lemmon, R.V. Morris, L Scherr, M. Schwochert, M.K. Shepard, G.H. Smith, J.N.
1972 Sohl-Dickstein, R. Sullivan, W.T. Sullivan, and M. Wadsworth, The Mars Exploration Rover
1973 Athena Panoramic Camera (Pancam) Investigation, *J. Geophys. Res.*, 108 (E12),
1974 [doi:10.1029/2003JE002070](https://doi.org/10.1029/2003JE002070), 2003.
- 1975 Bell III, J.F., J. Joseph, J.N. Sohl-Dickstein, H.M. Arneson, M.J. Johnson, M.T. Lemmon, and D.
1976 Savransky, In-flight calibration and performance of the Mars Exploration Rover Panoramic
1977 Camera (Pancam) Instruments, *J. Geophys. Res.*, 111, E02S03, [doi:10.1029/2005JE002444](https://doi.org/10.1029/2005JE002444),
1978 2006.
- 1979 Bell III, J.F., M. C. Malin, M. A. Caplinger, M. A. Ravine, A. S. Godber, M. C. Jungers, M. S.
1980 Rice, R. B. Anderson, Mastcam Multispectral Imaging on the Mars Science Laboratory
1981 Rover: Wavelength Coverage and Imaging Strategies at the Gale Crater Field Site, *43rd*
1982 *Lunar & Planetary Science Conf.*, Abstract #2541, 2012.
- 1983 Bell III, J.F., A. Godber, M. S. Rice, A. A. Fraeman, B. L. Ehlmann, W. Goetz, C. J. Hardgrove,
1984 D. E. Harker, J. R. Johnson, K. M. Kinch, M. T. Lemmon, S. McNair, S. Le Mouélic, M. B.
1985 Madsen, M. C. Malin, and the MSL Science Team, Initial Multispectral Imaging Results from
1986 the Mars Science Laboratory Mastcam Investigation at the Gale Crater Field Site, *44th Lunar*
1987 *& Planetary Science Conf.*, Abstract #1417, 2013.
- 1988 Bell III, J.F., J.N. Maki, G.L. Mehall, M.A. Ravine M.A. Caplinger, and the Mastcam-Z Science
1989 Team, Mastcam-Z: A Geologic, Stereoscopic, and Multispectral Investigation on the NASA

- 1990 Mars-2020 Rover, Abstract #1151, Presented at "International Workshop on Instrumentation
1991 for Planetary Missions (IPM-2014)," Greenbelt, Maryland, November 4-7, 2014.
- 1992 Bertelsen, P., W. Goetz, M. B. Madsen, K. M. Kinch, S. F. Hviid, J. M. Knudsen, H. P.
1993 Gunnlaugsson, J. Merrison, P. Nørnberg, S. W. Squyres, J. F. Bell III, K. E. Herkenhoff, S.
1994 Gorevan, A. S. Yen, T. Myrick, G. Klingelhöfer, R. Rieder and R. Gellert, Magnetic
1995 Properties Experiments on the Mars Exploration Rover Spirit at Gusev Crater, *Science*, 305,
1996 827-829 (2004).
- 1997 Brown, D.C., A solution to the general problem of multiple station analytical stereotriangulation.
1998 *RCA Data Reduction Technical Report No. 43*, Radio Corporation of America, 1958.
- 1999 Burns, P.D., sfrmat3: SFR evaluation for digital cameras and scanners,
2000 http://losburns.com/imaging/software/SFRedge/sfrmat3_post/index.html, 2015.
- 2001 Burns, P.D., Slanted-Edge MTF for Digital Camera and Scanner Analysis, Proc. IS&T 2000
2002 PICS Conference, pg. 135-138, 2000.
- 2003 Caplinger, M. A., MSSS MSL Camera Calibration Summary, 9 May 2013; available online from
2004 the NASA Planetary Data System's Imaging Node, at [http://pds-](http://pds-imaging.jpl.nasa.gov/data/msl/MSLMST_0008/CALIB/MSL_MMM_CAL.TXT)
2005 [imaging.jpl.nasa.gov/data/msl/MSLMST_0008/CALIB/MSL_MMM_CAL.TXT](http://pds-imaging.jpl.nasa.gov/data/msl/MSLMST_0008/CALIB/MSL_MMM_CAL.TXT)
- 2006 CODMAC: Committee on Data Management and Computation, "Data Management and
2007 Computation; Volume 1 - Issues and Recommendations", Space Science Board, Assembly of
2008 Mathematical and Physical Processes, National Research Council; National Academy Press;
2009 1982.
- 2010 Colina, L., R.C. Bohlin, and F. Castelli, The 0.12-2.5 micron absolute flux distribution of the
2011 Sun for comparison with solar analog stars, *Astron. J.*, 112, 307-315, 1996.
- 2012 Deen, R., A. Chen, K. Capraro, H. Gengl, S. Algermissen, N. Ruoff, O. Pariser, Pointing
2013 Correction for Mars Surface Mosaics, *2nd Planetary Data Workshop*, poster #7055, Flagstaff,
2014 AZ, June 8-11, 2015.
- 2015 Di, K. and R. Li, CAHVOR camera model and its photogrammetric conversion for planetary
2016 applications, *J. Geophys. Res.*, 109, E04004, [doi:10.1029/2003JE002199](https://doi.org/10.1029/2003JE002199), 2004.

- 2017 Eastman Kodak Company, "Kodak Interline Image Smear," Application note 2.0 MTD/PS-0899,
2018 March 5, 2009.
- 2019 Edgett, K.E., M.A. Caplinger, J.N. Maki, M.A. Ravine, F.T. Ghaemi, S. McNair, K.E.
2020 Herkenhoff, B.M. Duston, R.G. Willson, R.A. Yingst, M.R. Kennedy, M.E. Minitti, A.J.
2021 Sengstacken, K.D. Supulver, L.J. Lipkaman, G.M. Krezoski, M.J. McBride, T.L. Jones, B.E.
2022 Nixon, J.K. Van Beek, D.J. Krysak, and R.L. Kirk, Curiosity's robotic arm-mounted Mars
2023 Hand Lens Imager (MAHLI): Characterization and calibration status, MSL MAHLI Technical
2024 Report 0001, *ResearchGate Technical Reports*, [DOI: 10.13140/RG.2.1.3798.5447](https://doi.org/10.13140/RG.2.1.3798.5447), 2015.
- 2025 Edgett, K. S., Yingst, R. A., Ravine, M. A., Caplinger, M. A., Maki, J. N., Ghaemi, F. T.,
2026 Schaffner, J. A., Bell J. F. III, Edwards, L. J., Herkenhoff, K. E., Heydari, E., Kah, L. C.,
2027 Lemmon, M. T., Minitti, M. E., Olson, T. S., Parker, T. J., Rowland, S. K., Schieber, J.,
2028 Sullivan, R. J., Sumner, D. Y., Thomas, P. C., Jensen, E. H., Simmonds, J. J., Sengstacken, A.
2029 J., Willson, R. G., and Goetz, W., Curiosity's Mars Hand Lens Imager (MAHLI) investigation,
2030 *Space Sci. Rev.* 170, 259–317. [doi:10.1007/s11214-012-9910-4](https://doi.org/10.1007/s11214-012-9910-4), 2012.
- 2031 Gennery, D.B., Least-squares camera calibration including lens distortion and automatic editing
2032 of calibration points (Chap. 5), in *Calibration and Orientation of Cameras in Computer Vision*,
2033 ed. by A. Grun, T. Huang (Springer, Berlin), pp. 123–136. ISBN 3-540-65283-3, 2001.
- 2034 Gennery, D.B., Generalized camera calibration including fish-eye lenses. *Int. J. Comput. Vis.*
2035 68(3), 239–266, [doi:10.1007/s11263-006-5168-1](https://doi.org/10.1007/s11263-006-5168-1), 2006.
- 2036 Ghaemi, F.T., Design and fabrication of lenses for the color science cameras aboard the Mars
2037 Science Laboratory rover, *Opt. Eng.*, 48, pp. 103002-1 to 103002-15, 2009.
- 2038 Grotzinger, J.P.; Crisp, J.; Vasavada, A.R.; Anderson, R.C.; Baker, C.J.; Barry, R.; Blake, D.F.;
2039 Conrad, P.; Edgett, K.S.; Ferdowski, B.; Gellert, R.; Gilbert, J.B.; Golombek, M.; Gómez-
2040 Elvira, J.; Hassler, D.M.; Jandura, L.; Litvak, M.; Mahaffy, P.; Maki, J.; Meyer, M.; Malin,
2041 M.C.; Mitrofanov, I.; Simmonds, J.J.; Vaniman, D.; Welch, R.V.; and Wiens, R.C., Mars
2042 Science Laboratory Mission and Science Investigation, *Space Science Rev.*, 170, 5-56, 2012.
- 2043 Grotzinger, J.P., D. Y. Sumner, L. C. Kah, K. Stack, S. Gupta, L. Edgar, D. Rubin, K. Lewis, J.
2044 Schieber, N. Mangold, R. Milliken, P. G. Conrad, D. DesMarais, J. Farmer, K. Siebach, F.

- 2045 Calef III, J. Hurowitz, S. M. McLennan, D. Ming, D. Vaniman, J. Crisp, A. Vasavada, K. S.
2046 Edgett, M. Malin, D. Blake, R. Gellert, P. Mahaffy, R. C. Wiens, S. Maurice, J. A. Grant, S.
2047 Wilson, R. C. Anderson, L. Beegle, R. Arvidson, B. Hallet, R. S. Sletten, M. Rice, J. Bell III,
2048 J. Griffes, B. Ehlmann, R. B. Anderson, T. F. Bristow, W. E. Dietrich, G. Dromart, J.
2049 Eigenbrode, A. Fraeman, C. Hardgrove, K. Herkenhoff, L. Jandura, G. Kocurek, S. Lee, L. A.
2050 Leshin, R. Leveille, D. Limonadi, J. Maki, S. McCloskey, M. Meyer, M. Minitti, H. Newsom,
2051 D. Oehler, A. Okon, M. Palucis, T. Parker, S. Rowland, M. Schmidt, S. Squyres, A. Steele, E.
2052 Stolper, R. Summons, A. Treiman, R. Williams, A. Yingst, and MSL Science Team, A
2053 Habitable Fluvio-Lacustrine Environment at Yellowknife Bay, Gale Crater, Mars, *Science*,
2054 343 [DOI:10.1126/science.1242777], 2014.
- 2055 Hapke, B., *Theory of reflectance and emittance spectroscopy*, edited by R. E. Arvidson and M. J.
2056 Rycroft, Cambridge University Press, Cambridge, 1993.
- 2057 Howell, S.B., *Handbook of CCD Astronomy*, Cambridge University Press, 2000.
- 2058 Imatest, LLC (2015) SVG Squares and Wedges pattern test chart, online at
2059 http://www.imatest.com/docs/testcharts_sfr_svg/
- 2060 Janesick, J. R., Klaasen, K. P., and T. Elliott, Charge-coupled-device charge-collection
2061 efficiency and the photon-transfer technique, *Opt. Eng.*, 26, 972–980,
2062 doi:10.1117/12.7974183, 1987.
- 2063 Johnson, J. R. *et al.*, Radiative transfer modeling of dust-coated Pancam calibration target
2064 materials: Laboratory visible/near-infrared spectrogoniometry, *J Geophys Res-Planet*,
2065 111(E12S07), doi:10.1029–2005JE002658, 2006.
- 2066 Kinch, K. M., J. Sohl-Dickstein, J. F. I. Bell, J. R. Johnson, W. Goetz, and G. A. Landis, Dust
2067 Deposition on the Mars Exploration Rover Panoramic Camera (Pancam) Calibration Targets,
2068 *J Geophys Res-Planet*, 112, doi:10.1029/2006JE002807, 2007.
- 2069 Kinch, K. M., M. B. Madsen, J. F. Bell III, J. R. Johnson, and W. Goetz (2013), Dust on the
2070 Curiosity Mast Camera Calibration Target, *44th Lunar & Planetary Science Conf., Abstract*
2071 #1061, 2013.

- 2072 Kinch, K. M., Bell, J.F. III, Goetz, W., Johnson, J.R., Joseph, J., Madsen, M.B. and Sohl-
2073 Dickstein, J., Dust deposition on the decks of the Mars Exploration Rovers: 10 years of
2074 dynamics on the panoramic camera calibration targets, *Earth and Space Science*, 2, 144-172,
2075 doi:10.1002/2014EA000073, 2015.
- 2076 Lemmon, M.T., J.F. Bell III, M.C. Malin, K.M. Bean, A. Vasavada, F.J. Martin-Torres, M.-P.
2077 Zorzano-Mier, and the MSL Science Team, Astrometric Observations of Phobos and Deimos
2078 During Solar Transits Imaged by the Curiosity Mastcam, 44th Lunar and Planetary Science
2079 Conference, LPI Contribution No. 1719, p.1787, March 18-22, 2013.
- 2080 Lemmon, M.T., The Mars Science Laboratory optical depth record, Eighth International
2081 Conference on Mars, held July 14-18, 2014 in Pasadena, California, LPI Contribution No.
2082 1791, p.1338, 2014.
- 2083 Lemmon, M.T., J.F. Bell III, M.C. Malin, M.J. Wolff, J.N. Maki, J. Lasue, and S. Le Mouelic,
2084 Imaging of comet C/2013 A1 (Siding Spring) from the Martian surface, American
2085 Geophysical Union, Fall Meeting, abstract #P42A-08, 2014.
- 2086 Lemmon, M.T., Martian upper atmospheric aerosol properties from Phobos eclipse observation,
2087 American Astronomical Society, DPS meeting #47, id.401.09, 2015.
- 2088 Lemmon, M.T., M.J. Wolff, J.F. Bell III, M.D. Smith, B.A. Cantor, and P.H. Smith, Dust aerosol,
2089 clouds, and the atmospheric optical depth record over 5 Mars years of the Mars Exploration
2090 Rover mission, *Icarus*, 251, 96-111, doi:10.1016/j.icarus.2014.03.029, 2015.
- 2091 Lensation GmbH, "How to convert pixel size in line pairs per millimeter," *OptoWiki Knowledge*
2092 *Base*, <http://www.optowiki.info/faq/how-to-convert-pixel-size-in-line-pairs-per-millimeter/>,
2093 2013.
- 2094 Madsen, M.B., P. Bertelsen, W. Goetz, C.S. Binau, M. Olsen, F. Folkmann, H.P. Gunnlaugsson,
2095 K.M. Kinch, J.M. Knudsen, J. Merrison, P. Nørnberg, S.W. Squyres, A.S. Yen, J.
2096 Rademacher, S. Gorevan, T. Myrick, and P. Bartlett, The Magnetic Properties Experiments on
2097 the Mars Exploration Rover mission, *J. Geophys. Res.*, 108 (E12), 8069, 2003.

- 2098 Maki, J. N., J.F. Bell, K.E. Herkenhoff, S.W. Squyres, A. Kiely, M. Klimesh, M. Schwochert, T.
2099 Litwin, R. Willson, A. Johnson, M. Maimone, E. Baumgartner, A. Collins, M. Wadsworth,
2100 S.T. Elliot, A. Dingizian, D. Brown, E.C. Hagerott, L. Scherr, R. Deen, D. Alexander, J. Lorre,
2101 The Mars Exploration Rover Engineering Cameras, *J. Geophys. Res.*, *108*, 8071,
2102 [doi:10.1029/2003JE002077](https://doi.org/10.1029/2003JE002077), 2003.
- 2103 Maki, J., D. Thiessen, A. Pourangi, P. Kobzeff, T. Litwin, L. Scherr, S. Elliott, A. Dingizian, and
2104 M. Maimone, The Mars Science Laboratory Engineering Cameras, *Space Sci. Rev.*, *170*, 77-
2105 93, [doi:10.1007/s11214-012-9882-4](https://doi.org/10.1007/s11214-012-9882-4), 2012.
- 2106 Malin, M.C., Caplinger, M. A.; Edgett, K. S.; Ghaemi, F. T.; Ravine, M. A.; Schaffner, J. A.;
2107 Baker, J. M.; Bardis, J. D.; Dibiase, D. R.; Maki, J. N.; Willson, R. G.; Bell III, J. F.; Dietrich,
2108 W. E.; Edwards, L. J.; Hallet, B.; Herkenhoff, K. E.; Heydari, E.; Kah, L. C.; Lemmon, M. T.;
2109 Minitti, M. E.; Olson, T. S.; Parker, T. J.; Rowland, S. K.; Schieber, J.; Sullivan, R. J.;
2110 Sumner, D. Y.; Thomas, P. C.; Yingst, R. A., The Mars Science Laboratory (MSL) Mast-
2111 mounted Cameras (Mastcams) Flight Instruments, Lunar and Planetary Science Conference
2112 41, Lunar and Planetary Institute, Houston, TX, p. 1123, March 1-5, 2010.
- 2113 Malin, M.C., MA. Ravine, M.A. Caplinger, F.T. Ghaemi, J.A. Schaffner, J.N. Maki, J.F. Bell III,
2114 J.F. Cameron, W.E. Dietrich, K.S. Edgett, L.J. Edwards, J.B. Garvin, B. Hallet, K.E.
2115 Herkenhoff, E. Heydari, L.C. Kah, M.T. Lemmon, M.E. Minitti, T.S. Olson, T.J. Parker, S.K.
2116 Rowland, J. Schieber, R. Sletten, R.J. Sullivan, D.Y. Sumner, R.A. Yingst, B.M. Duston, S.
2117 McNair, and E.H. Jensen, The Mars Science Laboratory (MSL) Mast cameras and Descent
2118 imager: I. Investigation and instrument descriptions, *Earth & Space Science*, in press, 2017.
- 2119 Malin, M.C., K. Edgett, E. Jensen, and L. Lipkaman, "Mars Science Laboratory Project Software
2120 Interface Specification (SIS): Mast Camera (Mastcam), Mars Hand Lens Imager (MAHLI),
2121 and Mars Descent Imager (MARDI) Experiment Data Record (EDR), Reduced Data Record
2122 (RDR), and PDS Data Products," Version 1.2, JPL D-75410, October 29, 2013. Online at
2123 http://pds-imaging.jpl.nasa.gov/data/msl/MSLMST_0001/DOCUMENT/MSL_MMM_EDR_RDR_DPSIS.PDF
- 2124 Malvar, H.S., L. He, and R. Cutler. "High-quality linear interpolation for demosaicing of Bayer-
2125 patterned color images," *Acoustics, Speech, and Signal Processing, 2004. Proceedings, IEEE*

- 2126 *International Conference*, Vol. 3, IEEE, 2004. URL:
2127 http://www.ipol.im/pub/art/2011/g_mhcd/, 2004.
- 2128 Mikhail, E. M., J. S. Bethel, and J. D. McGlone, *Introduction to Modern Photogrammetry*, John
2129 Wiley, New York, 2001.
- 2130 Morris, R. V., and T. G. Graff, Athena instrument validation and data library development for
2131 the Mars Exploration Rover (MER) mission, *Eos Trans. AGU*, 83(47), Fall Meet. Suppl.,
2132 abstract P21C-03, 2002.
- 2133 National Aeronautics and Space Administration (NASA), "*Annular Eclipse of the Sun by Phobos,*
2134 *as Seen by Curiosity*", press release, 28 August 2013a. Online at
2135 <http://mars.nasa.gov/msl/multimedia/images/?ImageID=5536>.
- 2136 National Aeronautics and Space Administration (NASA), "*NASA Rover Gets Movie As A Mars*
2137 *Moon Passes Another*", press release, 15 August 2013b. Online at
2138 <http://mars.nasa.gov/msl/news/whatsnew/index.cfm?FuseAction=ShowNews&NewsID=1509>.
- 2139 National Aeronautics and Space Administration (NASA), "*Mercury Passes in Front of the Sun,*
2140 *as Seen From Mars*", press release, 10 June 2014. Online at
2141 <http://mars.nasa.gov/news/whatsnew/index.cfm?FuseAction=ShowNews&NewsID=1647>.
- 2142 National Aeronautics and Space Administration (NASA), "*Sunset in Mars' Gale Crater*", press
2143 release, 8 May 2015. Online at <http://mars.nasa.gov/msl/multimedia/images/?ImageID=7188>.
- 2144 ON Semiconductor, Inc., "Interline CCD Smear," Application Note AND9184/D, online at
2145 http://www.onsemi.com/pub_link/Collateral/AND9184-D.PDF, 2014.
- 2146 ON Semiconductor, Inc., "KAI-2020 1600 (H) x 1200 (V) Interline CCD Image Sensor," Pub.
2147 Order No. KAI-2020/D, online at <http://www.onsemi.com/pub/Collateral/KAI-2020-D.PDF>,
2148 2015.
- 2149 Pennebaker, W.B. and J.L. Mitchell, "JPEG: Still Image Data Compression Standard," 638 pp.,
2150 (ISBN-13: 978-0442012724, Springer, 1992.

- 2151 Peters, S., “Mars Science Laboratory Pointing, Positioning, Phasing, and Coordinate Systems
2152 (PPPCS) Document, Volume 9: Surface Remote Sensing and Navigation”, Version “Public
2153 Release”, May 13, 2016. Online at [http://pds-
imaging.jpl.nasa.gov/data/msl/MSLNAV_0XXX/DOCUMENT/PPPCS_VOL9_MAY_13_20
16.PDF](http://pds-
2154 imaging.jpl.nasa.gov/data/msl/MSLNAV_0XXX/DOCUMENT/PPPCS_VOL9_MAY_13_20
2155 16.PDF).
- 2156 Reid, R.J., P.H. Smith, M. Lemmon, R. Tanner, M. Burkland, E. Wegryn, J. Weinberg, R.
2157 Marcialis, D.T. Britt, N. Thomas, R. Kramm, A. Dummel, D. Crowe, B.J. Bos, J.F. Bell III, P.
2158 Rueffer, F. Gliem, J.R. Johnson, J.N. Maki, K.E. Herkenhoff, and R.B. Singer, Imager for
2159 Mars Pathfinder (IMP) image calibration, *J. Geophys. Res.*, *104*, 8907-8926, 1999.
- 2160 Rice, M.S., J.F. Bell III, E. A. Cloutis, A. Wang, S. Ruff, M.A. Craig, D.T. Bailey, J.R. Johnson,
2161 P.A. de Souza, Jr., and W.H. Farrand, Silica-rich deposits and hydrated minerals at Gusev
2162 Crater, Mars: Vis-NIR spectral characterization and regional mapping, *Icarus*, *205*, 375-395,
2163 [doi:10.1016/j.icarus.2009.03.035](https://doi.org/10.1016/j.icarus.2009.03.035), 2010.
- 2164 Stamnes, K., Tsay, S. C., Wiscombe, W. J., and Jayaweera, K., Numerically stable
2165 algorithm for discrete-ordinate-method radiative transfer in multiple scattering and emitting
2166 layered media. *Appl. Opt.*, *27*, 2502–2509, 1988.
- 2167 Tomasko, M.G., L.R. Doose, M.T. Lemmon, P.H. Smith, and E. Wegryn. Properties of dust in
2168 the martian atmosphere from the Imager for Mars Pathfinder, *J. Geophys. Res.*, *104*, 8987-
2169 9007, doi: 10.1029/1998JE900016, 1999.
- 2170 Truesense Imaging, Inc., "KAI-2020 Imaging Sensor," Device performance specification
2171 document, Rev. 1.0, PS-0017, June 22, 2012.
- 2172 Wellington, D.F., J.F. Bell III, J.R. Johnson, K.M. Kinch, M.S. Rice, A. Godber, B.L. Ehlmann,
2173 A.A. Fraeman, C. Hardgrove, S. Le Mouélic, and the MSL Science Team, Visible to Near-
2174 Infrared MSL/Mastcam Multispectral Imaging: Initial Results from Select High-Interest
2175 Science Targets within Gale Crater, Mars, submitted to *American Mineralogist*, 2016.
- 2176 Wiens, R.C. *et al.*, The ChemCam Instrument Suite on the Mars Science Laboratory (MSL)
2177 Rover: Body Unit and Combined System Performance, *Space Sci. Rev.*, [doi:10.1007/s11214-
2178 012-9902-4](https://doi.org/10.1007/s11214-012-9902-4), 2012.

- 2179 Williams, R.M.E., J. P. Grotzinger, W. E. Dietrich, S. Gupta, D. Y. Sumner, R. C. Wiens, N.
2180 Mangold, M. C. Malin, K. S. Edgett, S. Maurice, O. Forni, O. Gasnault, A. Ollila, H. E.
2181 Newsom, G. Dromart, M. C. Palucis, R. A. Yingst, R. B. Anderson, K. E. Herkenhoff, S. Le
2182 Mouélic, W. Goetz, M. B. Madsen, A. Koefoed, J. K. Jensen, J. C. Bridges, S. P. Schwenzer,
2183 K. W. Lewis, K. M. Stack, D. Rubin, L. C. Kah, J. F. Bell III, J. D. Farmer, R. Sullivan, T.
2184 Van Beek, D. L. Blaney, O. Pariser, R. G. Deen, and the MSL Science Team, Martian fluvial
2185 conglomerates at Gale crater, *Science*, *340*, 1068-1072, [doi:10.1126/science.1237317](https://doi.org/10.1126/science.1237317), 2013.
- 2186 Wolff, M.J., M. D. Smith, R. T. Clancy, R. Arvidson, M. Kahre, F. Seelos IV, S. Murchie, and H.
2187 Savijaärvi. Wavelength dependence of dust aerosol single scattering albedo as observed by the
2188 Compact Reconnaissance Imaging Spectrometer, *J. Geophys. Res.*, *114*, E00D04,
2189 [doi:10.1029/2009JE003350](https://doi.org/10.1029/2009JE003350), 2009.
- 2190 Yakimovsky, Y. and R. Cunningham, A system for extracting three-dimensional measurements
2191 from a stereo pair of TV cameras, *Computer Graphics and Image Processing*, *7*, 195-210,
2192 ISSN 0146-664X, [http://dx.doi.org/10.1016/0146-664X\(78\)90112-0](http://dx.doi.org/10.1016/0146-664X(78)90112-0), 1978.
- 2193 Yotam, E., P. Ephi, and Y. Ami, MTF for Bayer pattern color detector, in "Signal Processing,
2194 Sensor Fusion, and Target Recognition XVI", edited by I. Kadar, Proc. of SPIE Vol. 6567,
2195 65671M, [doi:10.1117/12.723140](https://doi.org/10.1117/12.723140), 2007.
- 2196 Zdankowski, W., T. Trautmann, and A. Bott, *Radiation in the Atmosphere*, 1st ed., Cambridge
2197 University Press, Cambridge, UK, 2007.
- 2198 Zhang, D., and Xiaolin Wu, "Color demosaicking via directional linear minimum mean square-
2199 error estimation." *Image Processing, IEEE Transactions*, *14.12*, 2167-2178, 2005.
- 2200
- 2201

2202 **14. Tables.**
2203

Table 1. MSL/Mastcam Electronic and Operational Characteristics		
<i>Characteristic</i>	<i>M-34 (Left)</i>	<i>M-100 (Right)</i>
Field of View (FOV)	20° × 15°	6.8° × 5.1°
Baseline Stereo Separation	24.5 cm	
Spatial Scale:	450 μm/pixel at 2 m, 22 cm/pixel at 1 km	150 μm/pixel at 2 m, 7.4 cm/pixel at 1 km
Angular Instantaneous FOV	0.22 mrad/pixel	0.074 mrad/pixel
Focal Length	34 mm	100 mm
<i>f</i> /number	8	10
Focus Range	~0.5 m to infinity	~1.6 m to infinity
Number of Spectral Filters	7 plus RGB Bayer pattern	7 plus RGB Bayer pattern
CCD Detector Gain	16.0 e ⁻ /DN	15.8 e ⁻ /DN
CCD Detector Read Noise	18.0 e ⁻	15.8 e ⁻
CCD Detector Full Well	26150 e ⁻	23288 e ⁻
Linearity (to 90% full well)	r ² > 0.999	r ² > 0.999

2204
2205

2206

2207

<i>M-34 (Left)</i>					<i>M-100 (Right)</i>				
Filter	$\lambda_{\text{eff}} \pm \text{HWHM}$ (nm)	F_{ref} (DN) ^a	F_{Sun} (W/m ² /nm) ^b	Precis. (%) ^c	Filter	$\lambda_{\text{eff}} \pm \text{HWHM}$ (nm)	F_{ref} (DN) ^a	F_{Sun} (W/m ² /nm) ^b	Precis. (%) ^c
L0 ^d	590 ± 88	--	--	--	R0 ^d	575 ± 90	--	--	--
L0R	640 ± 44	9343	0.8620	1.2	R0R	638 ± 44	5980	0.8653	1.9
L0G ^e	554 ± 38	10089	0.9771	0.3	R0G ^e	551 ± 39	6457	0.9802	1.5
L0B	495 ± 37	9802	1.0145	5.7	R0B	493 ± 38	6273	1.0175	2.5
L1	527 ± 7	1796	1.0064	4.3	R1	527 ± 7	1149	1.0064	3.7
L2	445 ± 10	2016	0.9381	51.0	R2	447 ± 10	1290	0.9886	24.5
L3	751 ± 10	1045	0.6654	0.3	R3	805 ± 10	454	0.5913	3.4
L4	676 ± 10	1635	0.7924	0.1	R4	908 ± 11	171	0.4630	0.4
L5	867 ± 10	364	0.5101	0.3	R5	937 ± 11	103	0.4402	0.5
L6	1012 ± 21	104	0.3770	1.0	R6	1013 ± 21	67	0.3769	1.0
L7	880±10, ND5 ^f	--	--	--	R7	440±10, ND5 ^f	--	--	--

Notes:

Shaded cells indicate filters where the narrowband response partially or completely blocks one or more of the Bayer RGB filter responses (see text for details).

^aReference DN level of a perfectly diffuse white sunlit surface at Mars perihelion distance (1.38 AU), with no atmospheric attenuation, at zero incidence angle, at an exposure time of 10 msec, and observed through this filter. See §5.2.7.

^bSolar spectral irradiance at the top of the Martian atmosphere at perihelion (1.38 AU), in W/m²/nm, convolved to each Mastcam filter bandpass. Solar spectral irradiance data at 1 AU from Colina *et al.*, 1996.

^cConservative estimate of the relative (filter to filter) precision for each filter. See §3.2.6.

^dBroadband near-IR cut-off filter used for Bayer filter RGB imaging. Data provided for reference only, as this cutoff filter can only be used in combination with the Bayer RGB filters.

^eThere are two green filters per 2×2 Bayer unit cell (Figure 1), with essentially identical characteristics.

^fND5 means 10⁻⁵ neutral density coating for solar imaging.

2208

2209

2210

2211

2212

2213

2214

2215

2216

2217

2218

2219

2220

2221

2222

2223

2224

2225 **Table 3. Types of "raw" and processed images that can be generated by the Mastcams**

Type	Product	Form	Encoding
A	Image	Image	Raster 16 bit, uncompressed
B			Raster 8 bit, uncompressed but companded
C			Losslessly compressed (Huffman)
D			JPEG grayscale (luminance only)
E			JPEG 4:2:2 YCrCb chrominance subsampling
F			JPEG 4:4:4 YCrCb chrominance subsampling
G		Thumbnail	Raster 8 bit, uncompressed but companded
H			JPEG grayscale (luminance only)
I			JPEG 4:4:4 YCrCb chrominance subsampling
J	Video	Image	Raster 8 bit, uncompressed but companded
K			Losslessly compressed (Huffman)
L			JPEG grayscale (luminance only)
M			JPEG 4:2:2 YCrCb chrominance subsampling
N			JPEG 4:4:4 YCrCb chrominance subsampling
O		Thumbnail	Raster 8 bit, uncompressed but companded
P			JPEG grayscale (luminance only)
Q			JPEG 4:4:4 YCrCb chrominance subsampling
R			ZStack
S	Range map Image	JPEG grayscale (luminance only)	
T	Focus Merge Thumbnail	JPEG 4:4:4 YCrCb chrominance subsampling	
U	Range Map Thumbnail	JPEG grayscale (luminance only)	

2226

2227

2228

2229 **Table 4.** Refined MSL Mastcam Multiplicative Radiometric Calibration Coefficients.

Filter Number	Effective Center Wavelength (nm)	Red	Green1	Green2	Blue
		[W/m ² /nm/sr) / (DN/s)] ± 1σ uncertainty			
<i>M-34 (Left Mastcam)</i>					
L0	590	3.56e-07 ± 3.6e-08	3.39e-07 ± 3.4e-08	3.39e-07 ± 3.4e-08	4.47e-07 ± 4.5e-08
L1	527	5.62e-05 ± 5.7e-06	2.38e-06 ± 2.4e-07	2.38e-06 ± 2.4e-07	8.69e-06 ± 8.7e-07
L2	445	1.60e-04 ± 1.1e-04	4.78e-05 ± 3.2e-05	4.54e-05 ± 3.0e-05	2.81e-06 ± 1.8e-06
L3	751	2.61e-06 ± 2.6e-07	8.96e-06 ± 9.0e-07	8.94e-06 ± 9.0e-07	2.86e-04 ± 3.0e-05
L4	676	2.04e-06 ± 2.0e-07	4.05e-05 ± 4.1e-06	4.28e-05 ± 4.3e-06	1.35e-04 ± 1.4e-05
L5	867	6.29e-06 ± 6.3e-07	6.51e-06 ± 6.5e-07	6.50e-06 ± 6.5e-07	6.51e-06 ± 6.5e-07
L6	1012	1.29e-05 ± 1.3e-06	1.28e-05 ± 1.3e-06	1.28e-05 ± 1.3e-06	1.29e-05 ± 1.3e-06
<i>M-100 (Right Mastcam)</i>					
R0	575	6.36e-07 ± 6.4e-08	6.08e-07 ± 6.1e-08	6.07e-07 ± 6.1e-08	7.98e-07 ± 8.0e-08
R1	527	9.06e-05 ± 9.1e-06	3.83e-06 ± 3.8e-07	3.83e-06 ± 3.8e-07	1.37e-05 ± 1.4e-06
R2	447	2.23e-04 ± 8.7e-05	6.32e-05 ± 2.4e-05	6.23e-05 ± 2.4e-05	4.09e-06 ± 1.6e-06
R3	805	6.96e-06 ± 7.0e-07	9.99e-06 ± 1.0e-06	9.94e-06 ± 9.9e-07	1.14e-05 ± 1.1e-06
R4	908	1.36e-05 ± 1.4e-06	1.38e-05 ± 1.4e-06	1.38e-05 ± 1.4e-06	1.39e-05 ± 1.4e-06
R5	937	1.81e-05 ± 1.8e-06	1.80e-05 ± 1.8e-06	1.80e-05 ± 1.8e-06	1.82e-05 ± 1.8e-06
R6	1013	2.15e-05 ± 2.1e-06	2.14e-05 ± 2.1e-06	2.14e-05 ± 2.1e-06	2.14e-05 ± 2.1e-06

2230

2231

2232

Table 5. Pre-Flight Mastcam Focus Motor Count vs. Distance Data			
<i>Mastcam 34 mm (left)</i>		<i>Mastcam 100 mm (right)</i>	
distance (m)	motor count	distance (m)	motor count
0.502	1802	1.682	1276
0.858	2007	1.827	1610
1.236	2105	2.006	1759
2.050	2224	3.004	2241
2.566	2249	4.196	2549
3.514	2303	4.257	2570
4.15	2310	4.654	2634
5.827	2315	5.051	2648
7.085	2320	6.037	2786
infinity	2404	7.025	2853
		infinity	3301

2233

2234

2235

2236

2237 **Table 6.** Known and Consistently Bad Pixels on the MSL/Mastcam CCDs.

M-34 (x, y) ^a	Kind ^b	M-100 (x, y) ^a	Kind ^b
(140, 167)	gray	(300,198)	gray
(448, 242)	hot	(821, 315) to (822, 319)	dead
(692, 611)	gray	(734, 363)	gray
(755, 612)	gray	(422, 588)	hot
(1034, 634)	gray		
(1446, 800)	gray		
(228, 924)	gray		
(792, 980)	hot		
(1354, 1027) to (1355, 1028)	gray		
(380, 1102)	gray		
(560, 1106)	hot		
(1416, 1193)	gray		

2238 ^aWhere (0,0) is the upper left pixel of each image.2239 ^bSee text for details.

2240

2241

2242

Table 7. MSL/Mastcam Geometric Camera Model Parameters.		
	Mastcam-34 (Left)	Mastcam-100 (Right)
<i>Camera Interior Orientation Parameters</i>		
Focal length f_{nom} , mm (see eq. 4)	34.367205	100.446803
Focus factor, f_f (see eq. 4)	0.0	-2.547113e-03
Boresight row	588.41	608.81
Boresight column	834.63	836.11
a_{11} , pixels per mm (see eqs. 7, 8)	135.153	135.154
a_{12} , pixels per mm (see eqs. 7, 8)	-0.0382	-0.0386
<i>Lens Radial Distortion Parameters</i>		
Lens distortion k_1	-1.118977e-04	1.513695e-04
Lens distortion k_2	-1.023513e-06	0.0
Distortion center row, mm	-0.113876	0.262451
Distortion center column, mm	0.152029	-0.250667

2243

2244

2245

2246

Table 8. MSL/Mastcam CAHVOR Camera Model Vector Parameters ^a			
<i>Mastcam 34 (Left)</i>			
(C)enter	0.767151	0.433709	-1.971648
(A)xis	0.999664	0.025047	0.006727
(H)orizontal	712.373106	4664.465028	33.182389
(V)ertical	570.612488	-14.279011	4648.733195
(O)ptical	0.999627	0.026908	0.004759
(R)adial	-0.000151	-0.139189	-1.250336
<i>Mastcam 100 (Right)</i>			
(C)enter	0.872866	0.677208	-1.970931
(A)xis	0.999741	-0.022668	0.001764
(H)orizontal	1162.600942	13353.11770	-93.448986
(V)ertical	512.731806	83.454058	13371.226140
(O)ptical	0.999495	-0.029483	0.011824
(R)adial	-0.000106	1.436779	-0.685884

The diagram illustrates the camera geometry. It shows a 3D coordinate system with axes X, Y, and Z. A camera center C is located at the origin. A point P is shown in 3D space. The vector from C to P is labeled P-C. An image plane is shown as a rectangle in the XY plane. The projection of P onto the image plane is a point (i, j). The axes of the image plane are labeled i and j. The camera's optical axis is labeled H'. The camera's vertical axis is labeled V'. The camera's horizontal axis is labeled A. The camera's radial axis is labeled C. The camera's axes are also labeled X, Y, and Z.

^ae.g., Yakimovsky & Cunningham, 1978; inset figure defining CAHV vectors is from Di & Li, 2004.

2247

2248

2249

Table 9. MSL Mast Kinematics Parameters		
Name	Value	Meaning
Pcal	0.80436	Calibration position of camera head, ROVER_NAV frame (meters)
	0.55942	
	-1.90608	
Qcal	0.99999	Calibration quaternion of camera head, ROVER_NAV frame (s,V)
	0.00001	
	-0.00325	
	-0.00104	
az_home	3.167345	Azimuth joint angle when head is forward/level (radians)
el_home	1.588171	Elevation joint angle when head is forward/level (radians)
az_point	0.714803	Arbitrary point on azimuth axis, ROVER_MECH frame (meters)
	0.559424	
	-1.109344	
az_axis	-0.001	Elevation axis unit vector, ROVER_MECH frame. Normalized by the pseudocode.
	0.0	
	1.0	
el_point	0.714668	Arbitrary point on elevation axis, ROVER_MECH frame (meters)
	0.561701	
	-0.785576	
el_axis	-0.022	Elevation axis unit vector, ROVER_MECH frame. Normalized by the pseudocode.
	-1.0	
	0.0	
az_elaxis	0.0	Azimuth during elevation axis survey, middle of backlash (radians)
epsilon	1.0e-10	Prevents divide-by-zero
rmech_to_rnav	0.09002	Add this to a ROVER_MECH frame value to convert it to ROVER_NAV (frame orientation is the same) (meters)
	0.0	
	-1.1205	

2250

2251

2252

2253

Table 10. In-Flight Bias and Dark Current Observational Data Compared to Pre-Flight Model

Sol	Sequence	LTST	t_{exp} (sec)	T _{CCD} (°C) ^a	T _{DEA} (°C)	DN Observed ^b		DN Modeled ^c	
						M-34	M-100	M-34	M-100
320	mcam01049	13:37	0.0	-9.5	+20.6	120.0	120.3	121.5	122.0
		13:37	0.1	-9.5	+20.6	--	120.4	--	122.1
		13:37	0.5	-9.5	+21.6	120.7	--	122.2	--
		13:37	1.0	-9.5	+21.6	--	121.7	--	123.1
		13:37	10.0	-9.5	+21.9	132.9	--	135.1	--
320	mcam01050	17:07	0.0	-12.7	+27.8	119.8	120.0	121.5	122.0
		17:08	0.1	-12.7	+27.8	--	120.1	--	122.1
		17:08	0.5	-12.7	+28.1	120.2	--	122.0	--
		17:08	1.0	-12.7	+28.1	--	121.1	--	122.9
		17:08	10.0	-12.7	+28.1	128.1	--	132.0	--
321	mcam01051	10:47	0.0	-26.4	+16.0	121.9	122.6	121.5	122.0
		10:47	0.1	-26.4	+16.0	--	122.6	--	122.0
		10:47	0.5	-26.1	+16.7	122.0	--	121.7	--
		10:47	1.0	-26.1	+16.7	--	122.8	--	122.3
		10:47	10.0	-26.1	+17.0	124.9	--	125.1	--
1350	mcam06485	11:28	0.0	-14.9	+17.0	120.2	122.0	121.5	122.0
		11:28	0.5	-14.6	+17.6	121.4	122.1	122.0	122.4
		11:28	10.0	-14.6	+17.6	129.1	130.5	130.5	129.8
1350	mcam06491	14:36	0.0	-5.7	+25.5	120.0	120.1	121.5	122.0
		14:36	0.5	-5.7	+25.8	120.8	121.9	122.4	122.8
		14:36	10.0	-5.7	+25.8	137.7	138.6	139.9	137.8
1350	mcam06492	16:36	0.0	-8.9	+25.2	120.0	120.3	121.5	122.0
		16:36	0.5	-8.5	+25.2	120.8	122.0	122.2	122.6
		16:36	10.0	-8.5	+25.5	133.8	133.7	136.2	134.7
1351	mcam06495	09:06	0.0	-15.2	+9.8	120.6	122.0	121.5	122.0
		09:06	0.5	-15.6	+10.5	121.8	122.1	121.9	122.4
		09:06	10.0	-15.6	+10.8	128.4	130.8	129.8	129.2

2254

2255

2256

2257

2258

2259

^aFor the M-34 (left) Mastcam CCD. Value for the M-100 (right) Mastcam CCD assumed to be the same.^bAfter adding back the onboard subtracted value of the DARK_LEVEL_CORRECTION label value.^cBased on pre-flight bias+dark current model in §3.2.2 and Figure 8.

2260
2261
2262**Table 11.** Validation and Refinement of MSL Mastcam Radiometric Calibration Coefficients Based on Radiance Modeling of In-Flight Mars Sky Observations.

Filter	Wavelength (nm)	Pre-Flight Coefficient ^a	Sky Model Coefficient ^b	Left/Right ratio ^b	Pre-Flight / Sky Model Coefficient Ratio
		[W/m ² /nm/sr] / (DN/s) ± 1σ uncertainty			
<i>M-34 (Left Mastcam)</i>					
L0R	640	3.56e-07 ± 3.6e-08	3.88e-07 ± 3.9e-08	-	0.92
L0G	554	3.39e-07 ± 3.4e-08	3.56e-07 ± 3.6e-08	-	0.95
L0B	495	4.47e-07 ± 4.5e-08	4.43e-07 ± 4.4e-08	-	1.01
L1	527	2.38e-06 ± 2.4e-07	2.38e-06 ± 2.4e-07	-	1.00
L2	445	2.81e-06 ± 1.8e-06	1.85e-06 ± 1.9e-07	-	1.52 ^c
L3	751	2.61e-06 ± 2.6e-07	2.62e-06 ± 2.6e-07	-	1.00
L4	676	2.04e-06 ± 2.0e-07	2.05e-06 ± 2.1e-07	-	1.00
L5	867	6.45e-06 ± 6.5e-07	6.47e-06 ± 6.5e-07	-	1.00
L6	1012	1.28e-05 ± 1.3e-06	1.50e-05 ± 1.5e-06	-	0.85
<i>M-100 (Right Mastcam)</i>					
R0R	638	6.36e-07 ± 6.4e-08	6.32e-07 ± 6.3e-08	0.615 ± 0.018	1.01
R0G	551	6.08e-07 ± 6.1e-08	5.89e-07 ± 5.9e-08	0.607 ± 0.018	1.03
R0B	493	7.98e-07 ± 8.0e-08	7.43e-06 ± 7.4e-08	0.598 ± 0.018	1.07
R1	527	3.83e-06 ± 3.8e-07	3.66e-06 ± 3.7e-07	0.650 ± 0.020	1.05
R2	447	4.09e-06 ± 1.6e-06	3.11e-06 ± 3.1e-07	0.628 ± 0.019	1.32
R3	805	6.96e-06 ± 7.0e-07	6.02e-06 ± 6.0e-07	n/a	1.16
R4	908	1.38e-05 ± 1.4e-06	1.21e-05 ± 1.2e-06	n/a	1.14
R5	937	1.81e-05 ± 1.8e-06	1.66e-05 ± 1.7e-06	n/a	1.09
R6	1013	2.14e-05 ± 2.1e-06	2.24e-05 ± 2.2e-06	0.668 ± 0.020	0.96

Notes:

^aFrom Table 4, using the dominant red, green, or blue channel as indicated in Table 12, or the average of all such channels for the green or infrared filters (see §3.2.4).^bSee §4.2.4 for details.^cShaded cells for Filters L2 and R2 highlight the fact that the sky model-derived radiometric calibration coefficients for these two filters are likely to be much more accurate than the pre-flight derived coefficients in Table 4. See §4.2.4 for details.2263
2264
2265
2266
2267
2268
2269
2270

2271

2272 **Table 12.** Bayer pattern interpolation scheme used for lossy JPEG-compressed Mastcam data.

Camera	Filter 0	Filter 1	Filter 2	Filter 3	Filter 4	Filter 5	Filter 6	Filter 7
M-34 (left)	Malvar ^a	Green ^b	Blue ^c	Red ^d	Red	Identity ^e	Identity	Identity
M-100 (right)	Malvar	Green	Blue	Red	Identity	Identity	Identity	Blue

2273 ^aMalvar means that interpolation using the algorithms of Malvar *et al.* (2004) is performed.2274 ^bGreen means that bilinear interpolation of green Bayer pixels is performed; red and blue pixels are discarded.2275 ^cBlue means that bilinear interpolation of blue Bayer pixels is performed; red and green pixels are discarded.2276 ^dRed means that bilinear interpolation of red Bayer pixels is performed; blue and green pixels are discarded.2277 ^eIdentity means that no interpolation is performed; image is returned as a monochrome JPEG that was compressed from raw data
2278 with as-is Bayer values (because the Bayer filters are transparent at near-IR wavelengths; see Figure 3).

2279

2280

2281

2282

2283 **Table 13.** Five kinds of Mastcam data products being archived in the NASA PDS.

Processing Code ^a	D = Decompressed?	R = Radiometrically Corrected?	C = Color Corrected?	L = Linearized?	CODMAC Level ^b
XXXX	no	no	no	no	2
DRXX	yes	yes	no	no	4
DRCX	yes	yes	yes	no	4
DRLX	yes	yes	no	yes	4
DRCL	yes	yes	yes	yes	4

2284 ^aEach letter in the code corresponds to the action in the next 4 columns. An "X" in the
2285 processing code corresponds to "no" for that action. See Appendix D.2286 ^bSee Appendix C.

2287

2288

2289

2290 **15. Figures and Captions.**

2291

2292

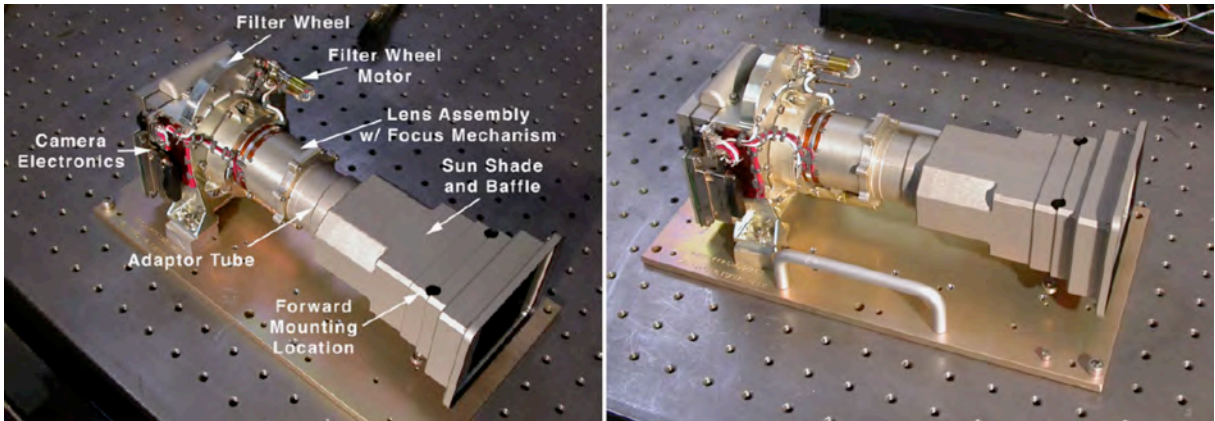


Figure 1. The Mastcam M-34 camera head (left) and M-100 camera head (right). For scale, spacing of the optical table's bolt hole pattern is 1".

2293

2294

2295

2296

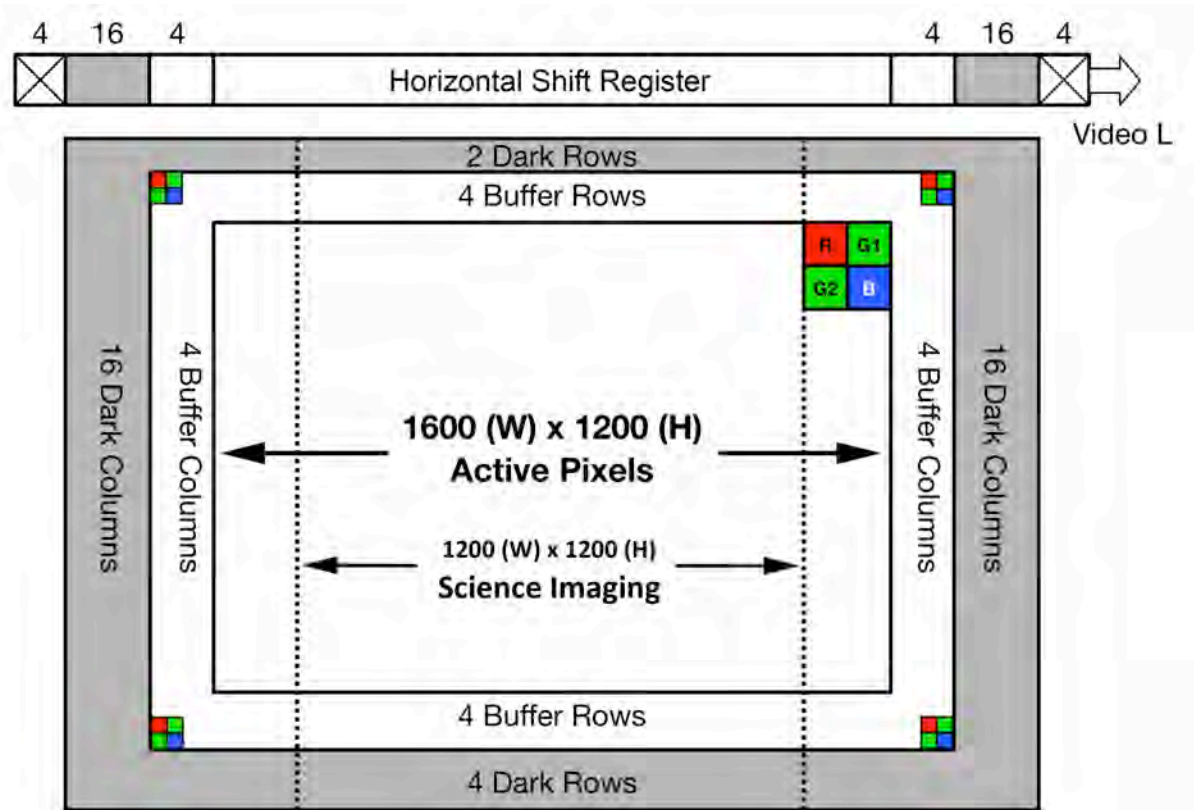


Figure 2. Simplified schematic of the Kodak KAI-2020 interline transfer CCD used in the MSL Mastcams, along with a graphical representation of each of the 2×2 Bayer RGB filter unit cells bonded directly onto the CCD's active pixels. Pixels are not depicted to scale, in order to display all of the relevant RGB unit cell, dark shielded, buffer, science imaging, and horizontal shift register regions described in the text. Pixel clocking is up then to the right in this representation of the image coordinate space, and so the first pixel clocked out is a Green 1. Figure is based on original Kodak vendor data available online at: <http://www.stargazing.net/david/QSI/KAI-2020LongSpec.pdf>.

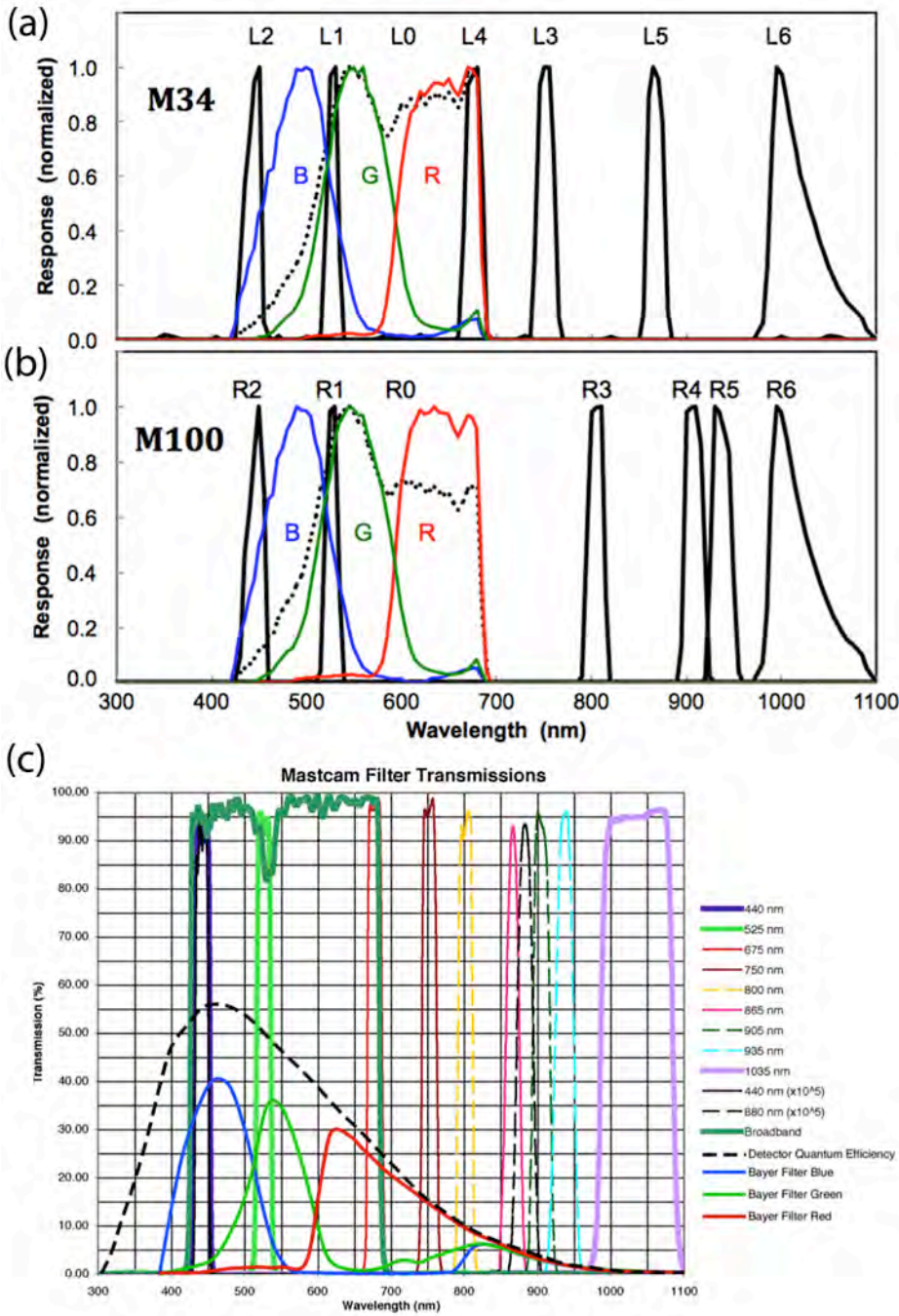
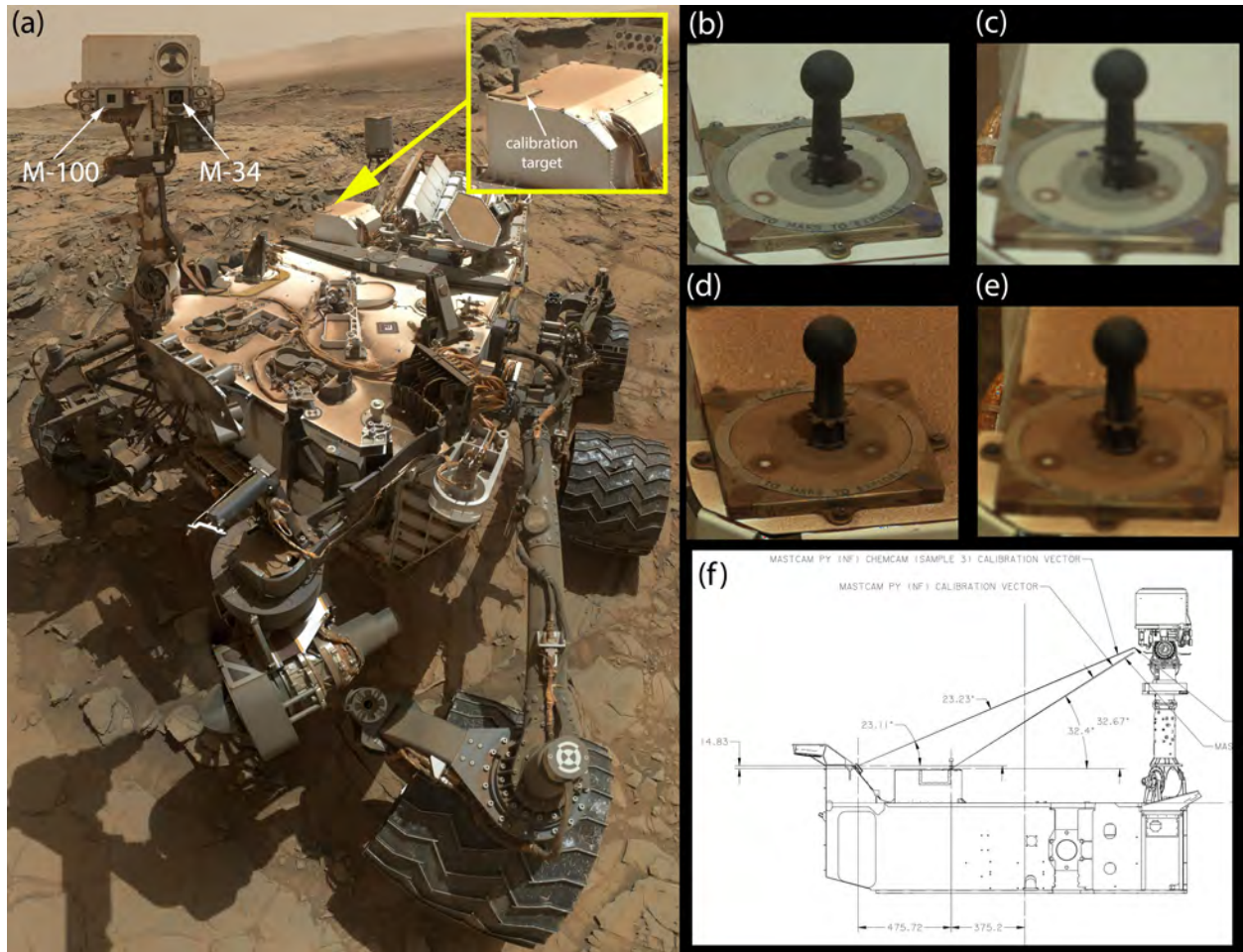


Figure 3. Normalized MSL/Mastcam system-level spectral response profiles for the left eye M-34 camera (a) and the right eye M-100 camera (b). When the filter wheel is set to Filter 0 (broadband IR cutoff; dashed profiles shown here), the resulting Bayer filter RGB response profiles are as shown here in red, green, and blue. (c) When the filter wheel is set to a nonzero number, however, the response profiles of the Bayer filters are as shown here, based on component-level detector QE (%) and filter transmission data provided by the vendor.

2298



2299

2300 **Figure 4.** (a) Locations of the M-34 and M-100 Mastcam cameras as well as the Mastcam calibration
 2301 target (inset) within the sol 1126 MAHLI "selfie" taken at the "Big Sky" drilling site within Gale crater.
 2302 Images (b) and (c) show the M-34 and M-100 views, respectively, of the calibration target on sol 69,
 2303 when they were generally free of airfall dust. Dust deflected by the "sweep magnets" embedded below the
 2304 calibration surface (see §2.2) has been captured into rings in the corners and on the white and gray
 2305 patches of the target. Images (d) and (e) show the M-34 and M-100 views, respectively, of the calibration
 2306 target on sol 807, when they had become appreciably dusty [like much of the rest of the rover deck in (a)].
 2307 Drawing (f) shows the elevation angle from which the calibration target is viewed relative to the
 2308 Mastcams ($\approx 32.4^\circ$ up from horizontal). For reference, the ChemCam calibration target (Wiens *et al.* 2012;
 2309 visible in the upper right of the inset in (a), behind the Mastcam calibration target), is at an angle of
 2310 $\approx 23.1^\circ$ up from horizontal, when viewed by the Mastcams.

2311

2312

2313

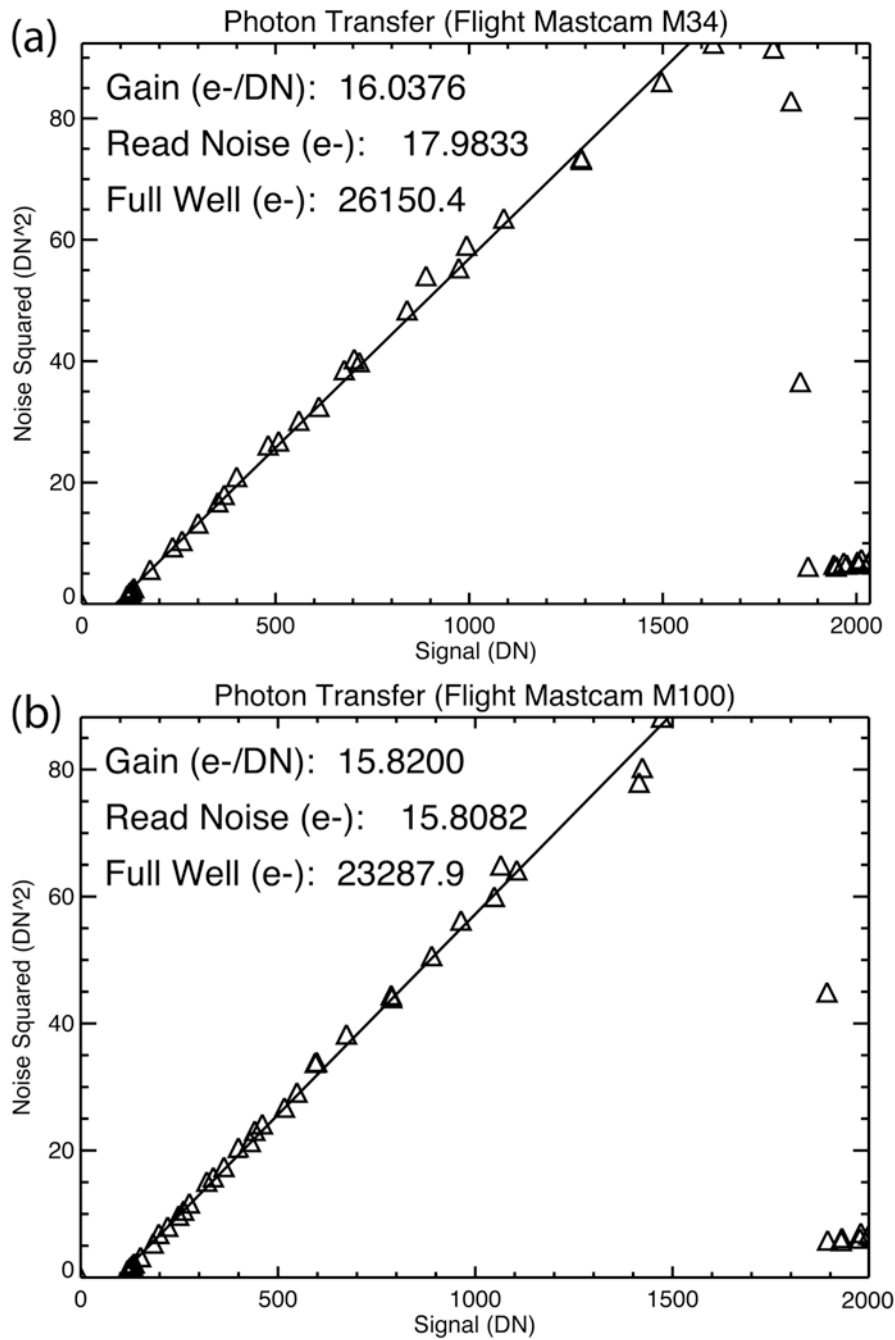


Figure 5. MSL/Mastcam 34-mm (a) and 100-mm (b) pre-flight CCD linearity, gain, and full well photon transfer curve data sets, with resulting CCD parameters derived using the methods of Janesick *et al.* (1987).

2314

2315

2316

2317

2318

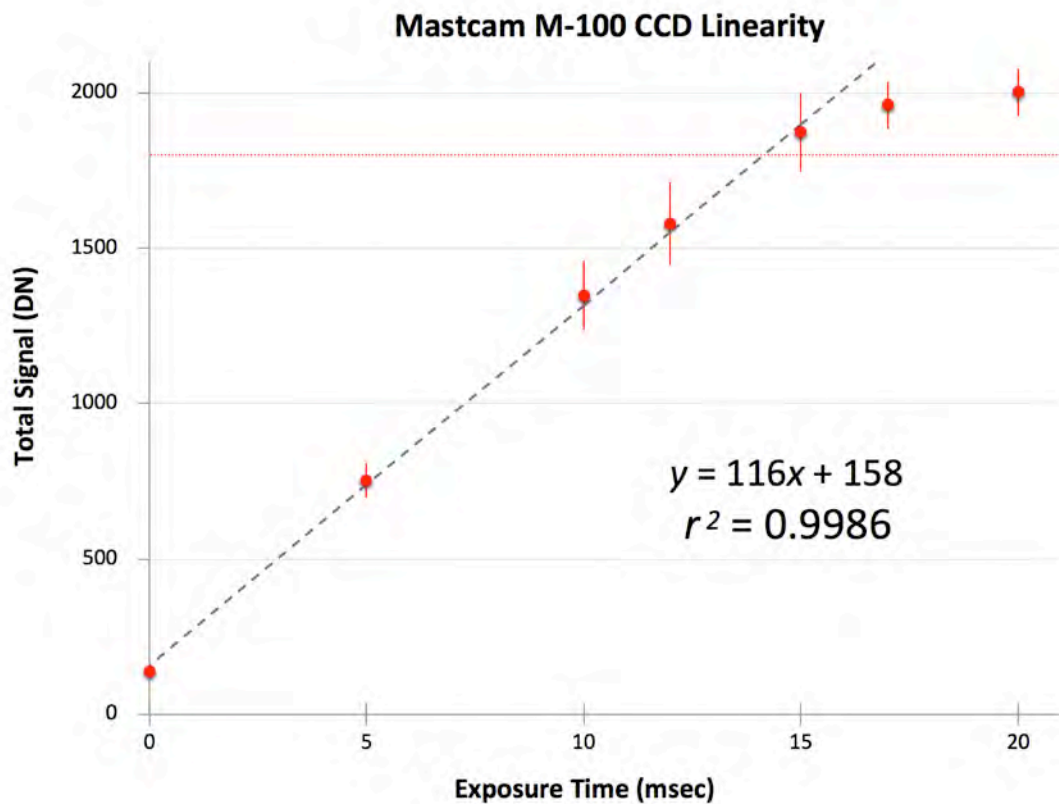


Figure 6. Example MSL/Mastcam CCD linearity test data results from integrating sphere data taken through the Bayer red filter, demonstrating linear performance of the M-100 detector from zero through ~90% full well. Performance is similar for the M-34 CCD. The r^2 value of the linear fit is for the first 4 data points only. In post-processing, signal levels above 1800 DN (red horizontal line) are flagged as nonlinear.

2319

2320

2321

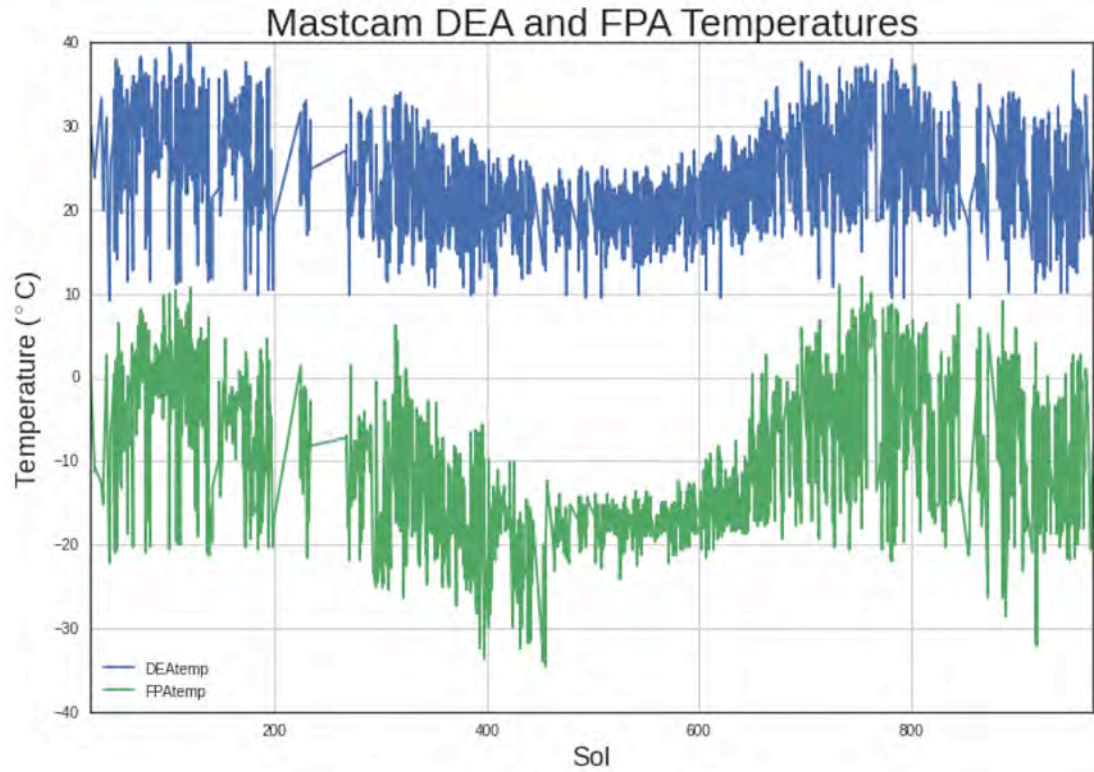


Figure 7. Actual range of flight temperatures experienced by the M-34 Mastcam Focal Plane Array (FPA; green lower data) and Digital Electronics Assembly (DEA; blue upper data) during the first ~1000 sols of Curiosity's mission on Mars. Temperature telemetry for the M-100 Mastcam FPA and DEA are not downlinked as frequently, and so the behavior of the M-100 optics heater temperature sensor (HTR-1 in the PDS archived data labels) or sometimes the M-34 camera's FPA temperature is often used as a proxy for the temperature history of the M-100 (see §4.2.1).

2322

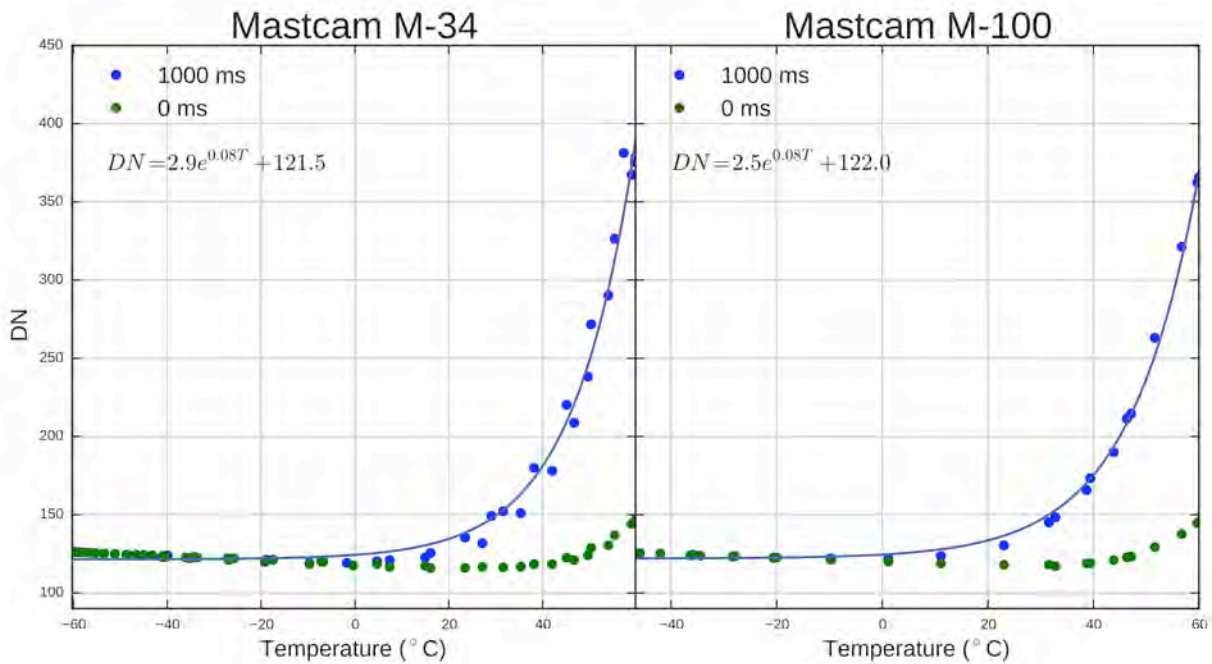


Figure 8. Zero-exposure bias signal (green data points) and 1000 msec dark current (blue data points) data for the M-34 (left) and M-100 (right) Mastcam CCDs, as a function of Focal Plane Array (FPA) temperature. Fits to the dark current data show the functional form of the Mastcam dark current model, in DN/sec.

2323

2324

2325

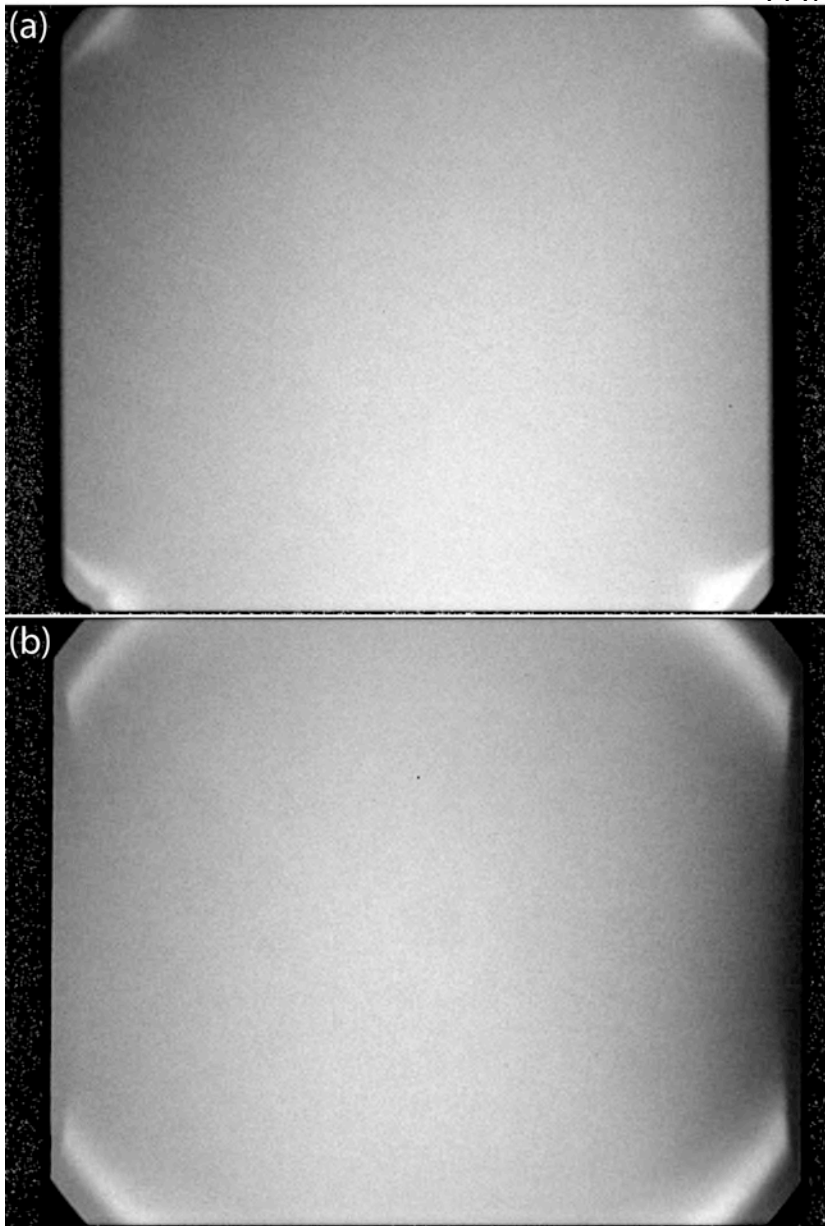


Figure 9. Example 1648×1200 pixel M-34 (a) and M-100 (b) Mastcam Filter 0 flatfield images. These images correspond to the de-Bayered G1 pixels from each camera. Nonuniformities noted in visual inspection include: occasional dead pixels, blurring at left and right edges, brightening near corners, and vignetting in corners. Pixel (0,0) is at the top left of each image. The problematic corner regions are not included in standard 1200×1200 pixel "science imaging" data acquired by Mastcam (see text). These normalized flatfield images are contrast enhanced so that black is ≤ 0.85 and white is ≥ 1.05 .

2328

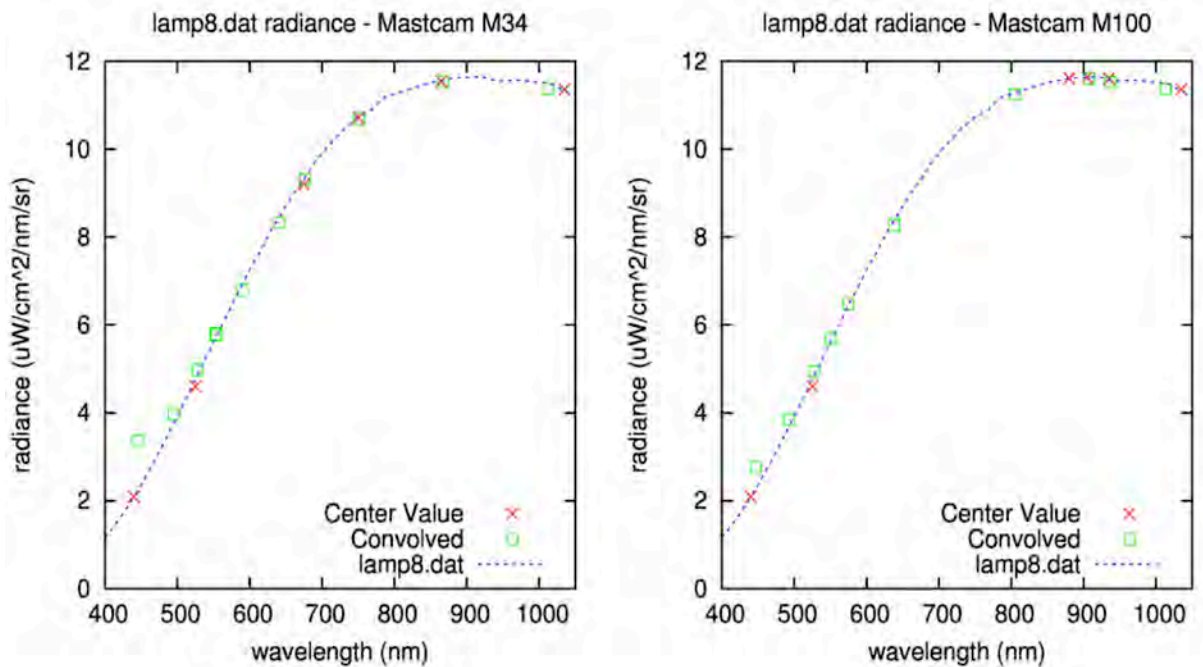


Figure 10. Estimated integrating sphere input radiances used for deriving M-34 (left) and M-100 (right) radiance calibration coefficients for each of the filters in each camera (Table 4). "Center value" estimates are used in the current tactical-timeline radiance calibration of Mastcam images. Refined estimates based on a full convolution of the Mastcam spectral response profiles derived in §3.2.4 are shown as "Convolved" (weighted) data points. "lamp8.dat" refers to the NIST-calibrated spectral radiance of the integrating sphere. Significant deviations in the fit of the weighted L2 and R2 (445 and 447 nm) data points to the input lamp spectrum result in higher relative uncertainties in the radiance calibration coefficients for those filters.

2329

2330

2331

2332

2333

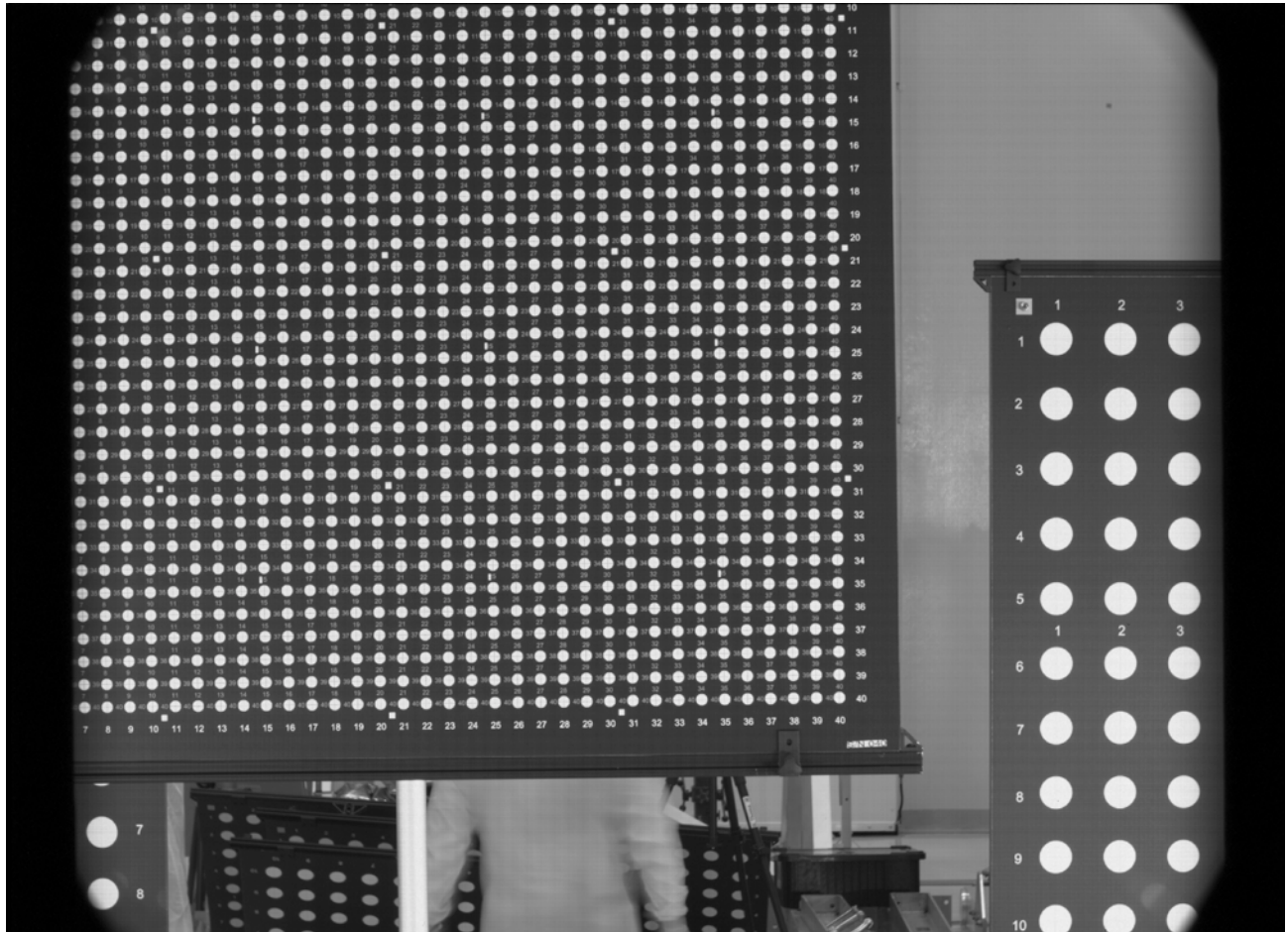


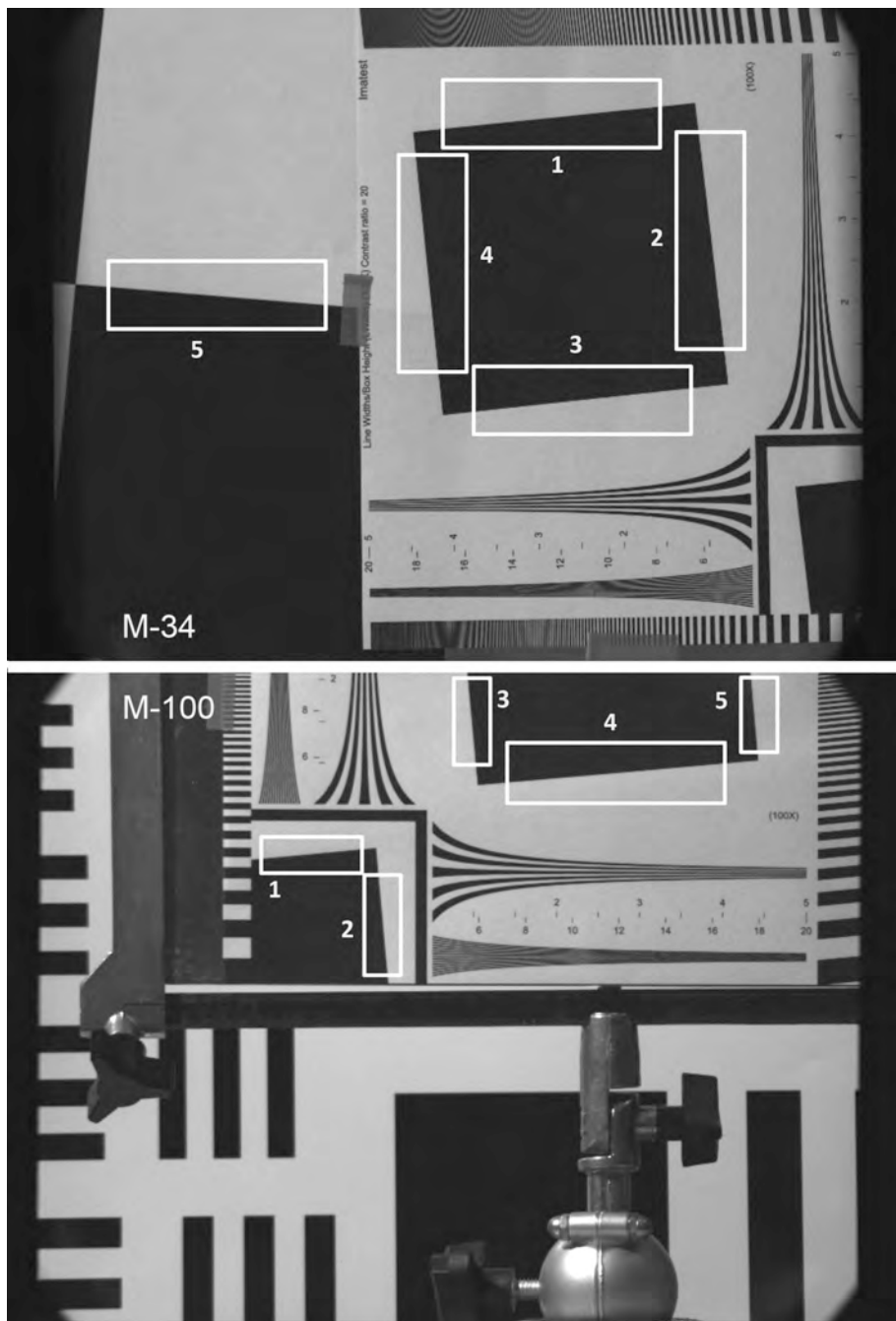
Figure 11. Example pre-flight Mastcam M-34 image of geometric calibration targets obtained during initial rover-level testing at JPL.

2334

2335

2336

2337

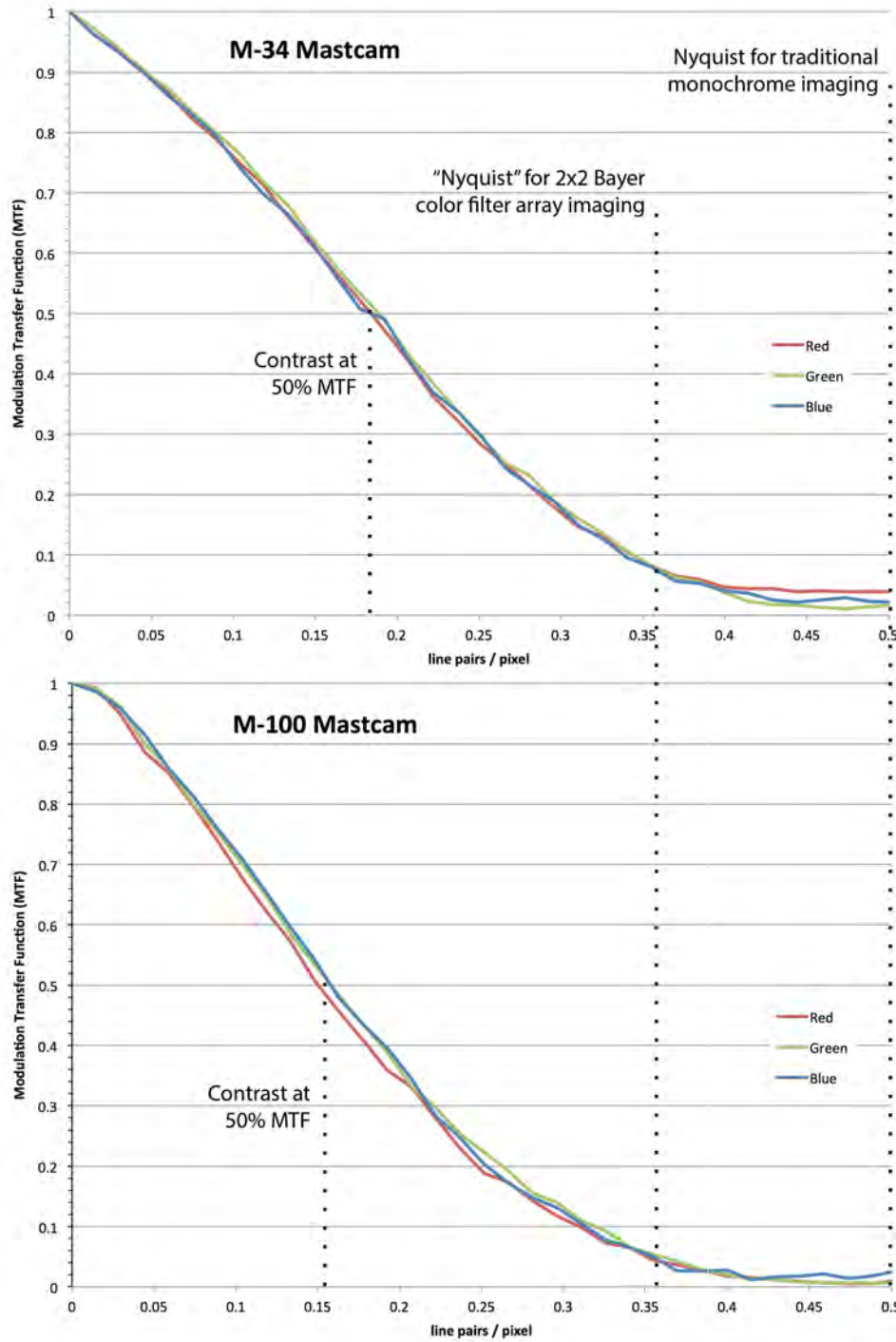


2338

2339 **Figure 12.** Example flight Mastcam 34-mm (top) and
 2340 100-mm (bottom) pre-flight calibration interpolated Green Bayer pixel
 2341 images of the "SVG Squares and Wedges pattern" target (Imatest,
 2342 2015) used to assess the MTF performance of the flight cameras.
 2343 Five regions of interest, numbered on each image, were analyzed.

2344

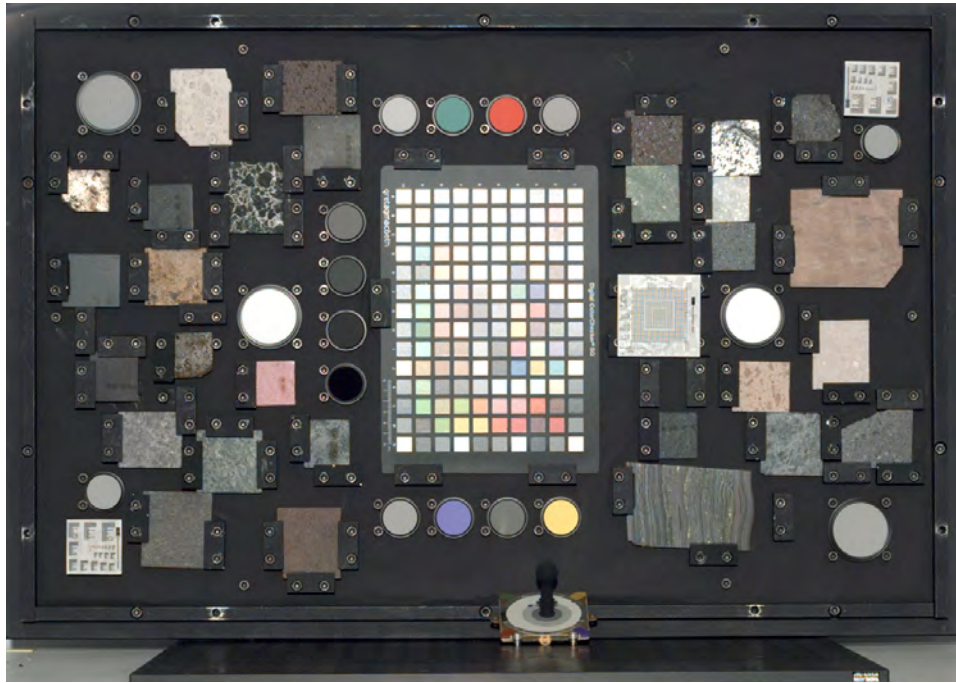
2345



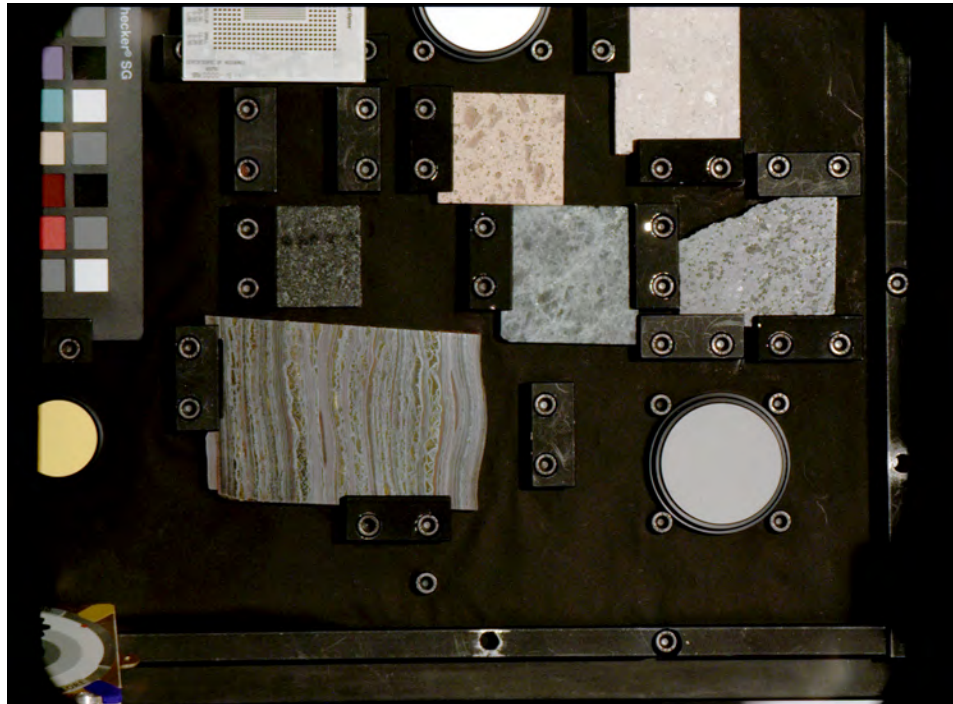
2346

2347 **Figure 13.** Modulation Transfer Function (MTF) curves for the M-34 (top) and
2348 M-100 (bottom) Mastcams, based on analyses of the resolution target images shown
2349 in Figure 12. See text for details.
2350

2351



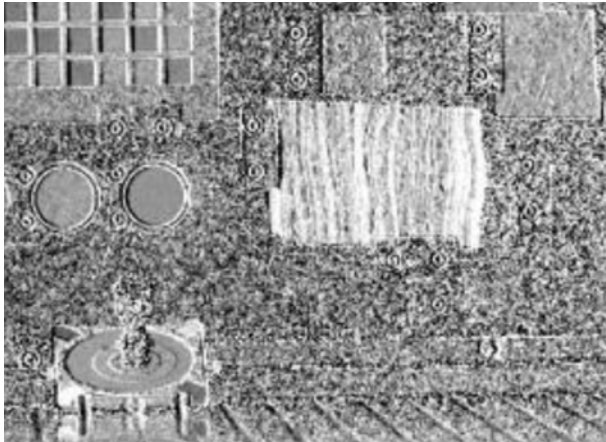
2352



2353

2354 **Figure 14.** Geometric, color/reflectance, and geologic materials target imaged under ambient pressure and
 2355 temperature conditions during MSL/Mastcam pre-flight calibration at Malin Space Science Systems, Inc., during
 2356 late September, 2009. (Top) Entire target imaged by the wide angle M-34 flight instrument; (Bottom) Lower right of
 2357 target imaged by the narrow-angle M-100 flight instrument at 3x higher resolution. Images have been white
 2358 balanced using reference reflectance standards in the scene. For scale, the gray circular target at lower right is 5 cm
 2359 in diameter. An engineering model of the Mastcam calibration target was also imaged in the foreground.

2360



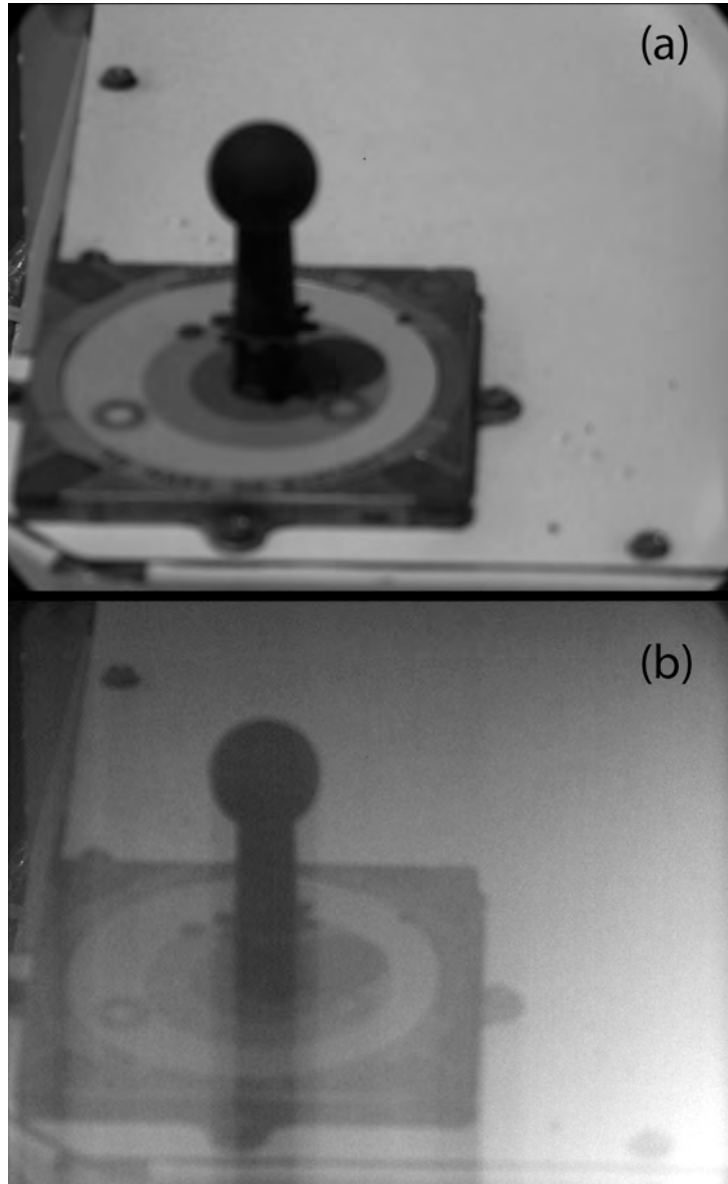
2361

2362 **Figure 15.** Band depth map at 865 nm (relative to
2363 continuum wavelengths at 751 nm and 1012 nm)
2364 generated from a portion of the Mastcam M-34 pre-flight
2365 geologic target multispectral imaging campaign (Figure
2366 14). This spectral parameter is sensitive to the presence
2367 of crystalline hematite, and indeed highlights the
2368 hematite-bearing color chip on the lower left of the
2369 Mastcam calibration target, and the hematite-bearing
2370 layers in the Banded Iron Formation geologic sample.

2371

2372

2373

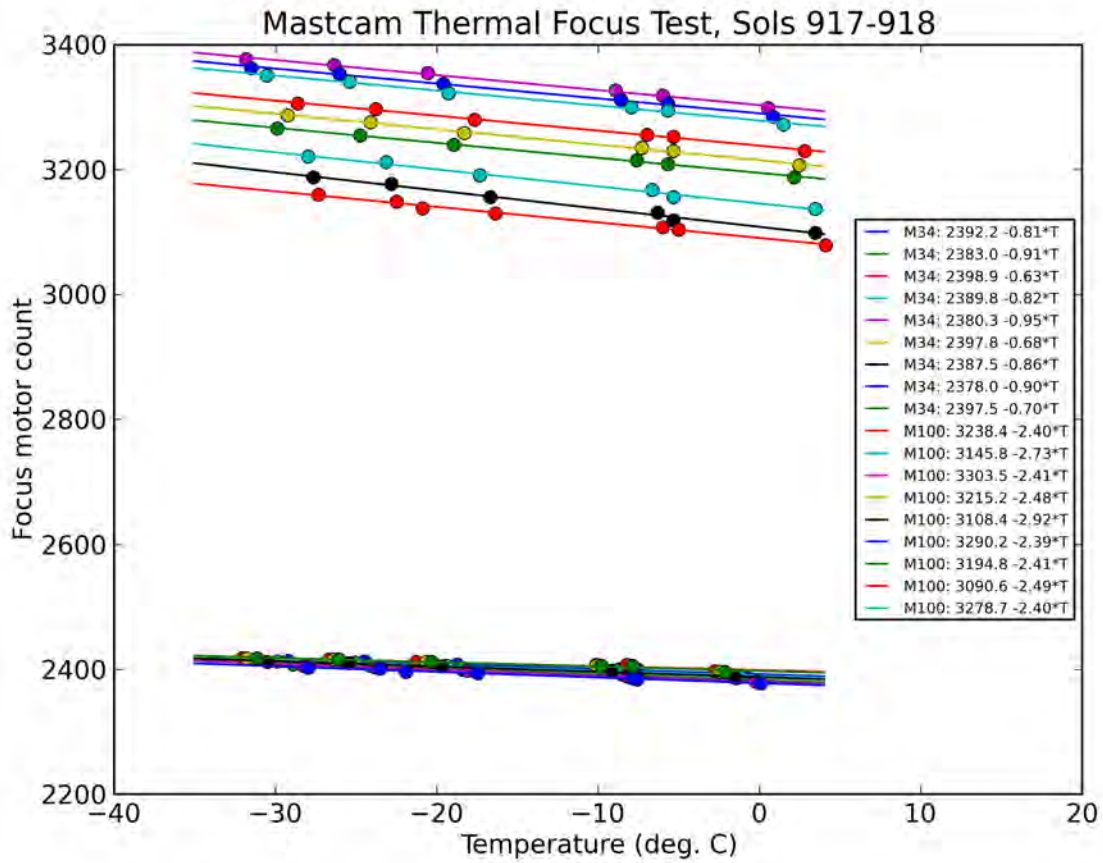


2374

2375 **Figure 16.** Example of in-flight electronic shutter smear test images acquired on *Curiosity* sol 38 in sequence
2376 mcam00169. (a) "Normal" M-100 filter R0 green Bayer filter image of the Mastcam calibration target using an
2377 exposure time of 4.3 msec; (b) "Smeared" M-100 filter R0 green Bayer filter image of the same scene acquired
2378 immediately after image (a) at a commanded exposure time of 0.0 msec. The zero-second image shows effects of
2379 both shutter smear and a "ghost image" of the original scene. See text for details.

2380

2381

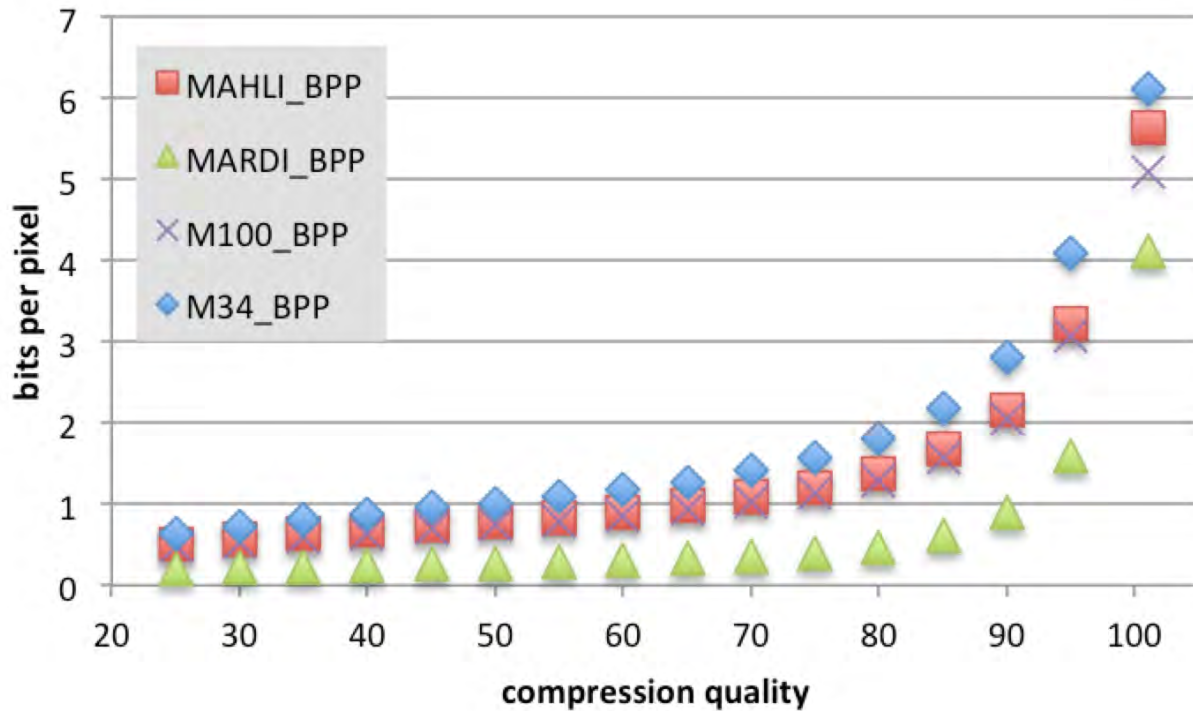


2382

2383 **Figure 17.** Dependence of focus motor count on Mastcam focal plane array temperature for the M-34 and M-100
 2384 Mastcams, based on six in-flight mosaic sequences acquired on Mars on *Curiosity* sols 917 and 918.

2385

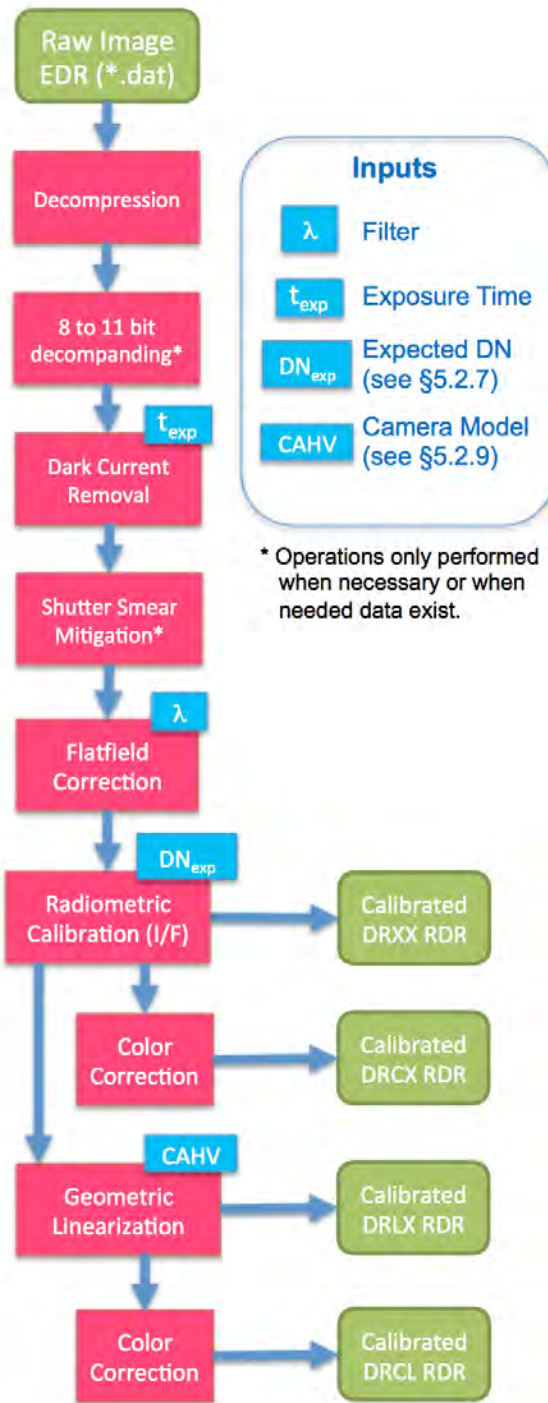
2386



2387

2388 **Figure 18.** (a) Average compression performance of the Mastcam JPEG compression algorithm (Malin *et*
 2389 *al.*, 2013) as a function of JPEG quality factor, for hundreds of representative Mars images from the four
 2390 color cameras on the *Curiosity* rover. "Bits per pixel" on the y-axis is relative to the original downlinked
 2391 8-bit companded data. Lower y-axis values mean more compressible images (*e.g.*, 4 bits per pixel is a
 2392 compression factor of 2:1; 1 bit per pixel is a compression factor of 8:1). Values at quality factor 101
 2393 correspond to losslessly-compressed images. While the difference in downlinked bits is large between
 2394 losslessly-compressed images and those that are JPEG compressed to high quality factors, the difference
 2395 in image quality is often imperceptible to the human eye (however, see also Figure 29).

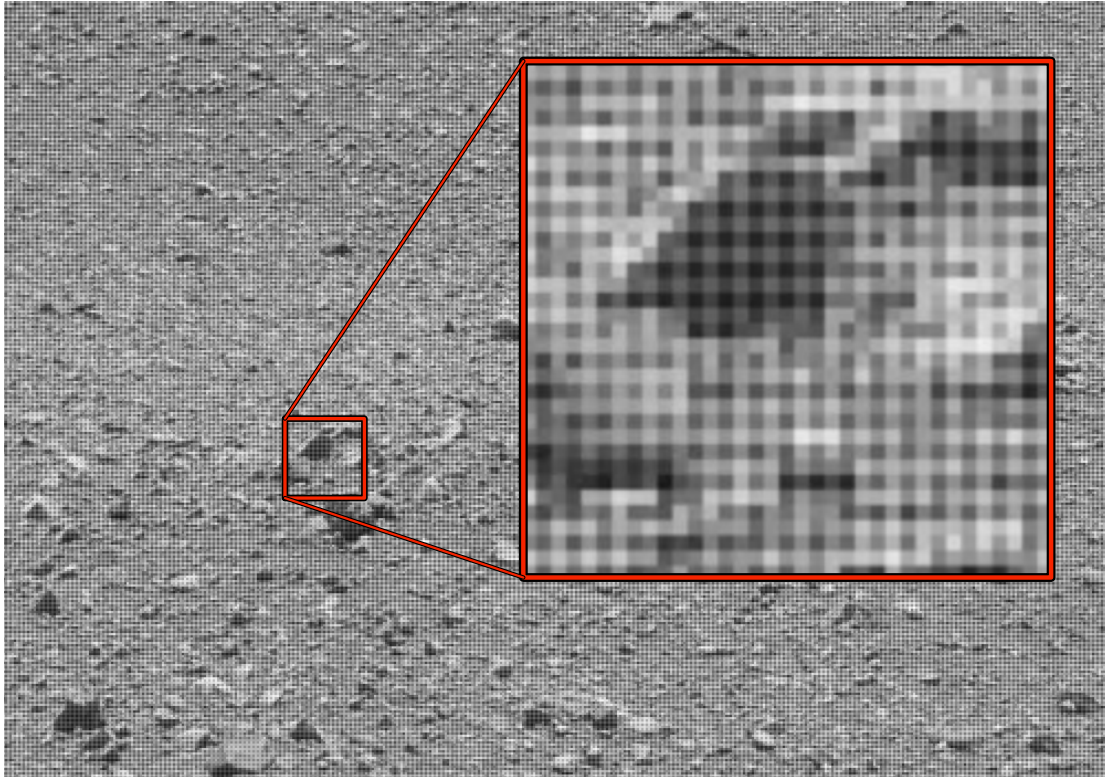
2396



2397

2398 **Figure 19.** Flow chart of MSL/Mastcam tactical data calibration steps, for initial data sets being archived in the PDS.

2399



2400

2401 **Figure 20.** Raw Mastcam image downlinked from Mars, exhibiting apparent high frequency noise from
 2402 the Bayer pattern (Figure 2). Inset: Magnified image to show the Bayer pattern more clearly.

2403

2404

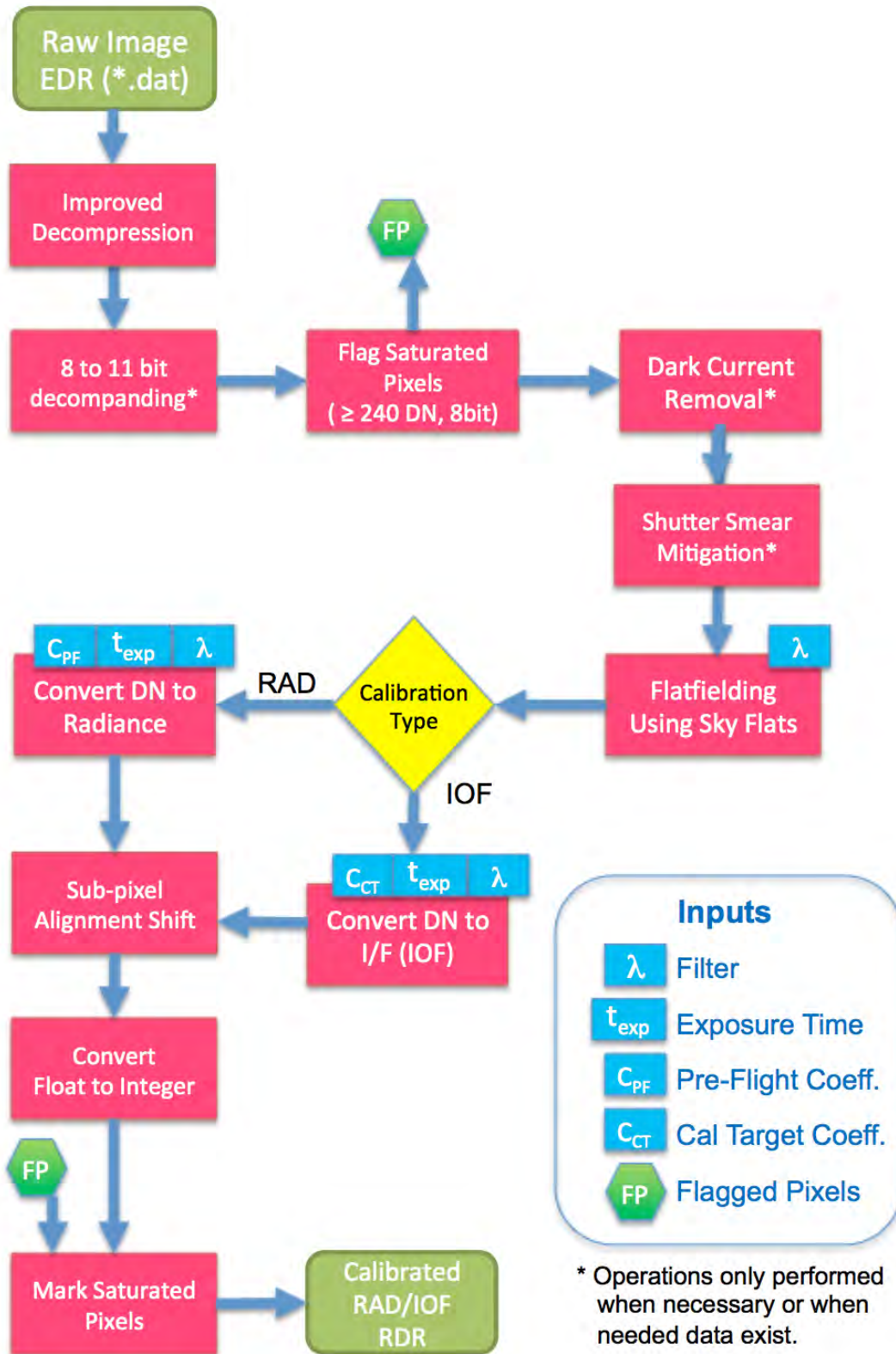
2405

Pixels (Columns) at the Beginning of Each Mastcam Full-width 1648 Pixel Row																								
0	1	2	3	4	5	6	7	8	9	10	11	12	13	14	15	16	17	18	19	20	21	22	23	
		isolation					dark pixels																	
invalid ADC pipeline pixel from previous line																								
dark pixels from the previous line																								
JPEG MCU 0								JPEG MCU 1								JPEG MCU 2								

2406

2407 **Figure 21.** Layout of the first 24 columns of full-width Mastcam images, showing the details of the first 23
 2408 masked (dark) pixels in columns 0-22, and the first photo-active pixel (column 23). The JPEG
 2409 compressor's Minimum Coded Units (MCUs) are also indicated. See text for details, and see also Figure 2.

2410



2411

2412

Figure 22. Flow chart describing enhanced MSL/Mastcam data calibration steps.

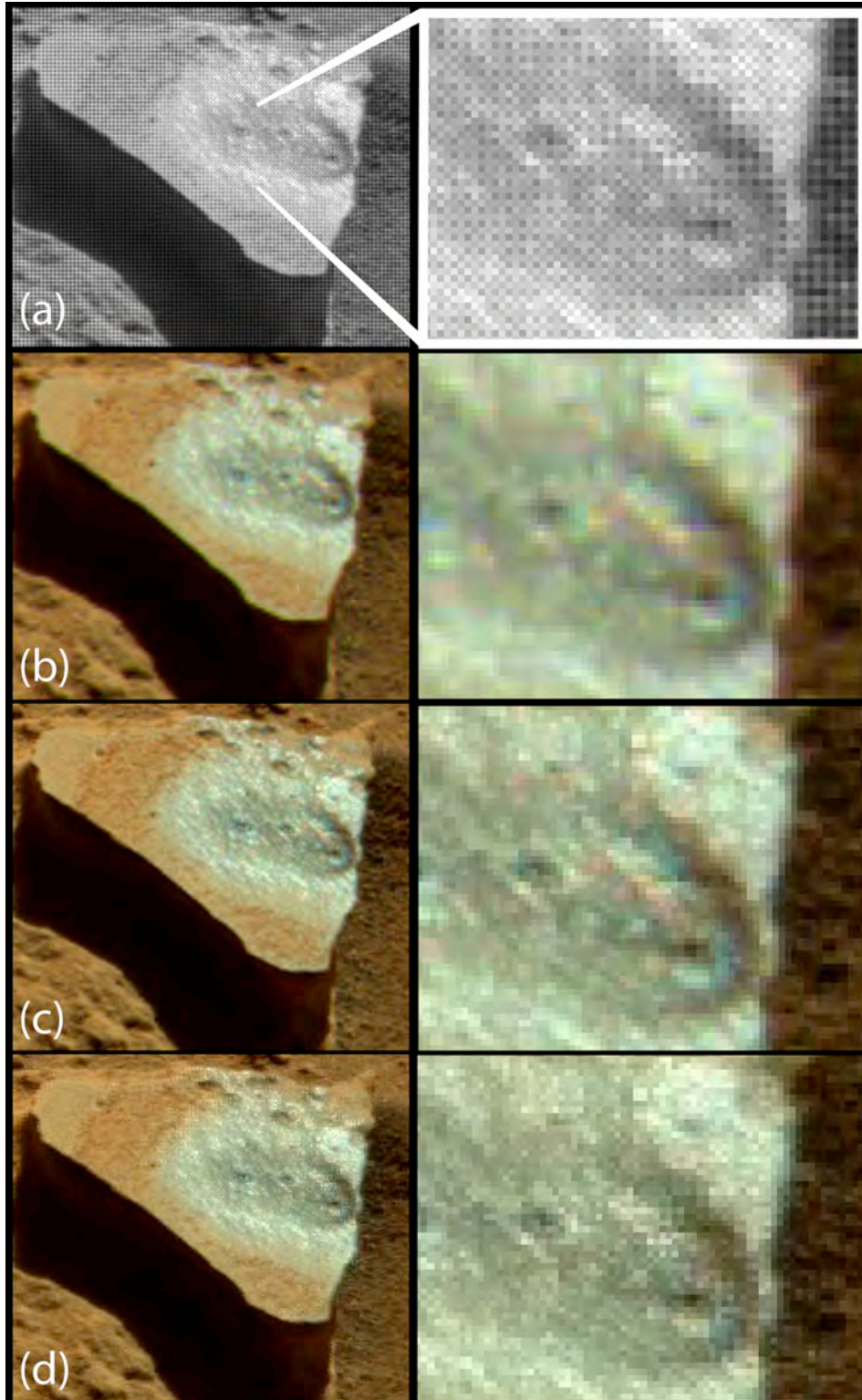
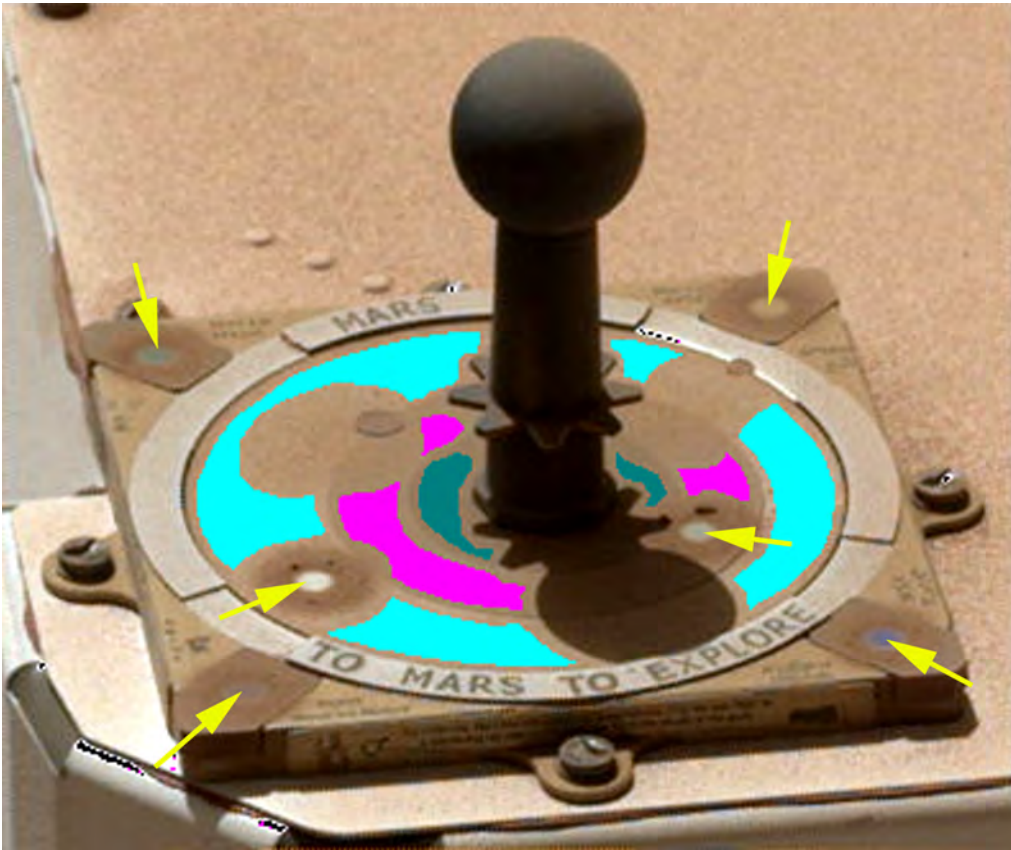


Figure 23. Comparison of (a) raw MSL Mastcam image showing the original Bayer filter pattern, versus application of (b) bilinear interpolation; (c) default Improved Linear Interpolation (ILI), or Malvar-He-Cutler; and (d) Directional Linear Minimum Mean Square-Error Estimation (DLMMSE), or Zhang-Wu, demosaicing algorithms. Portion of Mastcam M-100 image 0620MR0026570000401488C00_DXXX, with zoomed insets on the right.

2414



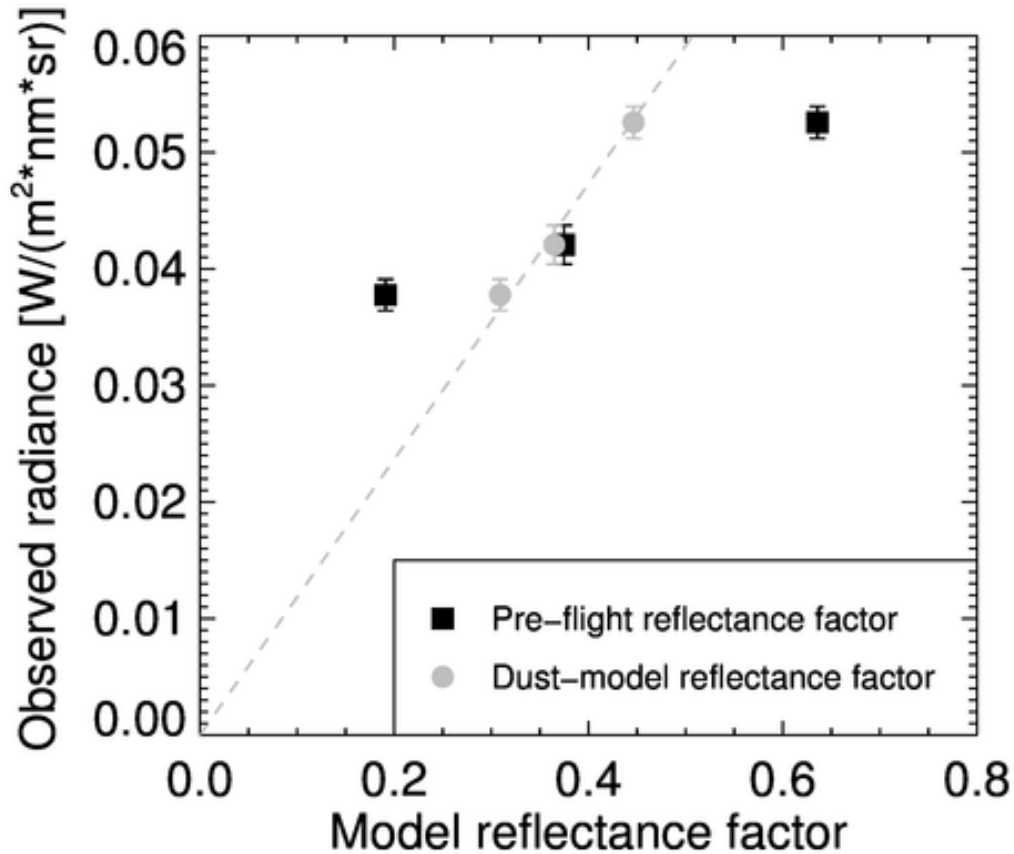
2415

2416 **Figure 24:** Image of the Mastcam's dusty calibration target acquired around noon local time on sol 514 of the
2417 mission (16 January 2014). The image was acquired through the standard Bayer RGB bands of the Mastcam's L0
2418 filter. The effect of the 6 sweep magnets is apparent with rings of strong dust accumulation around small spots of
2419 reduced dust cover (arrows). Drawn on top of the image are selected ROIs from the three grayscale rings away from
2420 the magnets and other regions of thicker concentrations of dust on the rings. Turquoise: White ring, Light purple:
2421 Gray ring, Teal: Black ring. Image ID: 0514ML0020230030202937D01.

2422

2423

2424



2425

2426

2427

2428

2429

2430

2431

2432

2433

2434

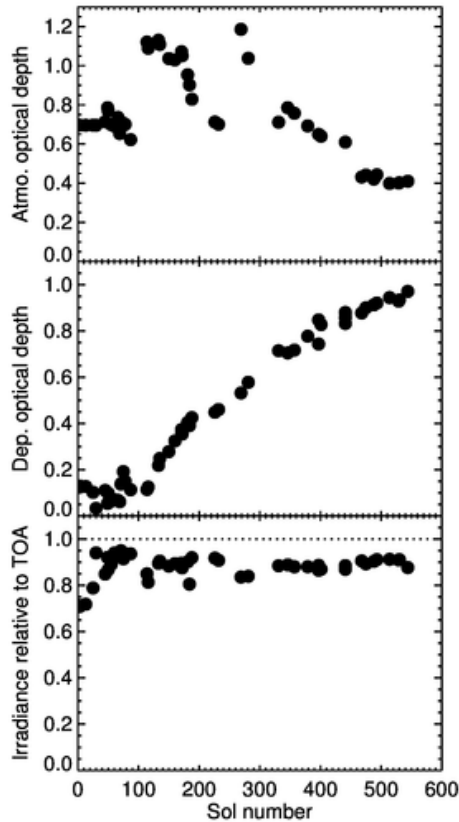
2435

2436

2437

Figure 25: Radiance-reflectance plot for calibration target image acquired through the Mastcam's L3 (751 nm) filter on sol 514 as part of the same sequence as the image in Figure 24. The data points show observed radiances from the black, gray, and white region calibration target ROI's, as shown in Figure 24. The error bars are a simple standard deviation of all pixels within the ROI. Black squares show the three calibrated radiances plotted at the abscissa values of the clean caltarget reflectances that were determined pre-flight. Those points do not fit a line that would go through zero radiance at zero reflectance, and so clearly the reflectances of the ROI's have changed (the cal target has become dusty). The gray circles are the same three observed radiances, but plotted as a function of the reflectances derived from our cal target dust correction model.. The gray points fall approximately on a straight line through the origin, telling us that the dust model is indeed working properly. The slope of this line is a measure of the incoming irradiance.

2438



2439

2440

Figure 26: Time evolution of quantities derived by the dust model for all Mastcam calibration target images in the L3 (751 nm) filter and with the sun at least 45° above the horizon. The first 600 sols of the mission are shown.

2441

The middle plot shows the derived extinction optical depth, τ_{cal} , of dust deposited on the caltarget. There is some noise in the early part of the mission but after that the plot shows a smooth increase in dust cover, with a slightly

2442

lower rate towards the later period. For comparison the top plot shows atmospheric optical depths as derived from observations of the sun by the Mastcams L7 (880 nm) solar filter. The atmospheric dust load was lower at the later

2443

period consistent with the observed lower deposition rate. The bottom plot shows model derived solar irradiance

2444

relative to the known Top Of Atmosphere (TOA) value. Apart from some noise early on the derived values are

2445

stable around 0.9. The noise in the beginning of the mission is probably because of the influence of dust deposited

2446

on the caltarget during landing. This material is likely to have had different color properties than the airfall dust.

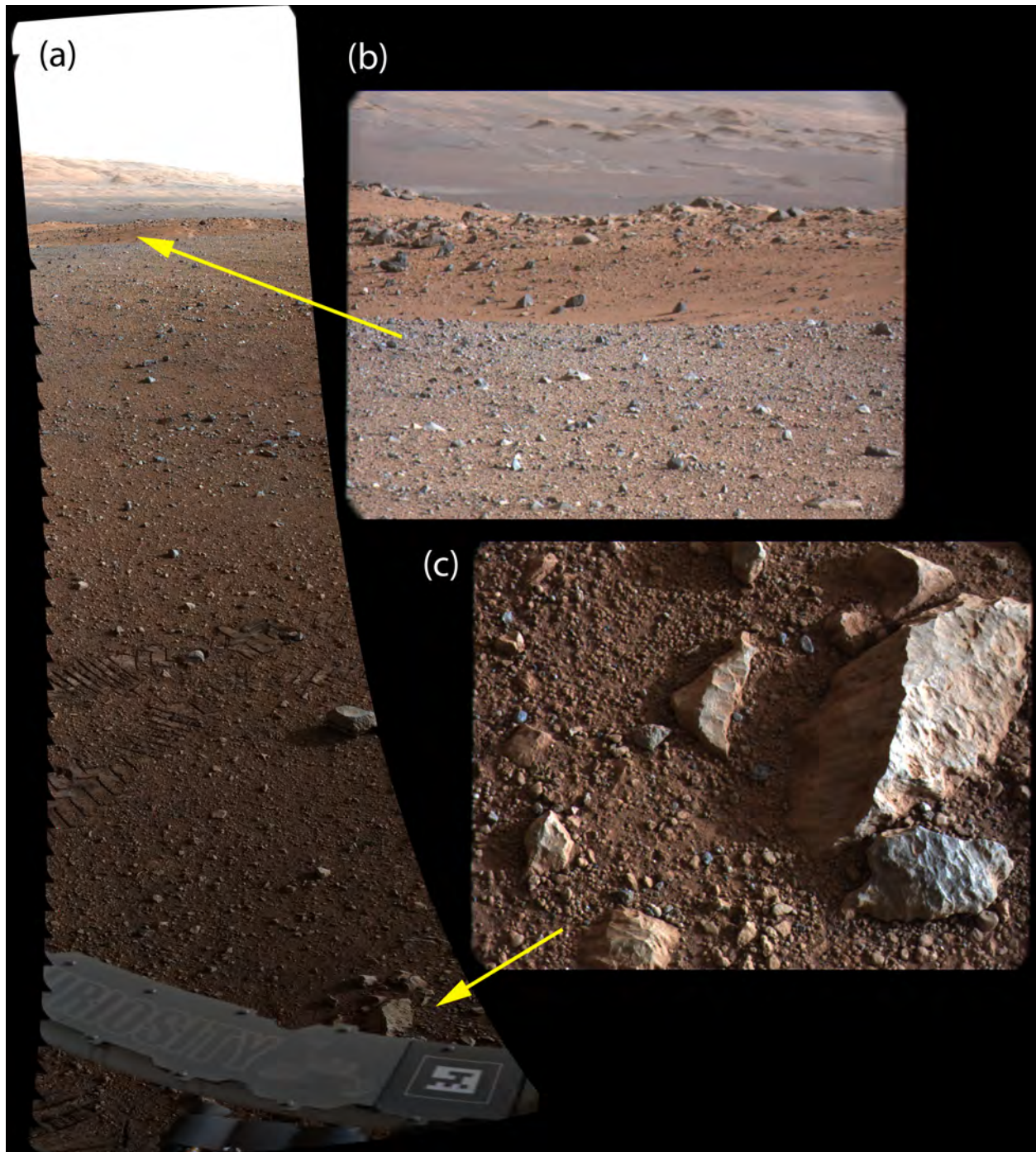
2447

2448

2449

2450

2451

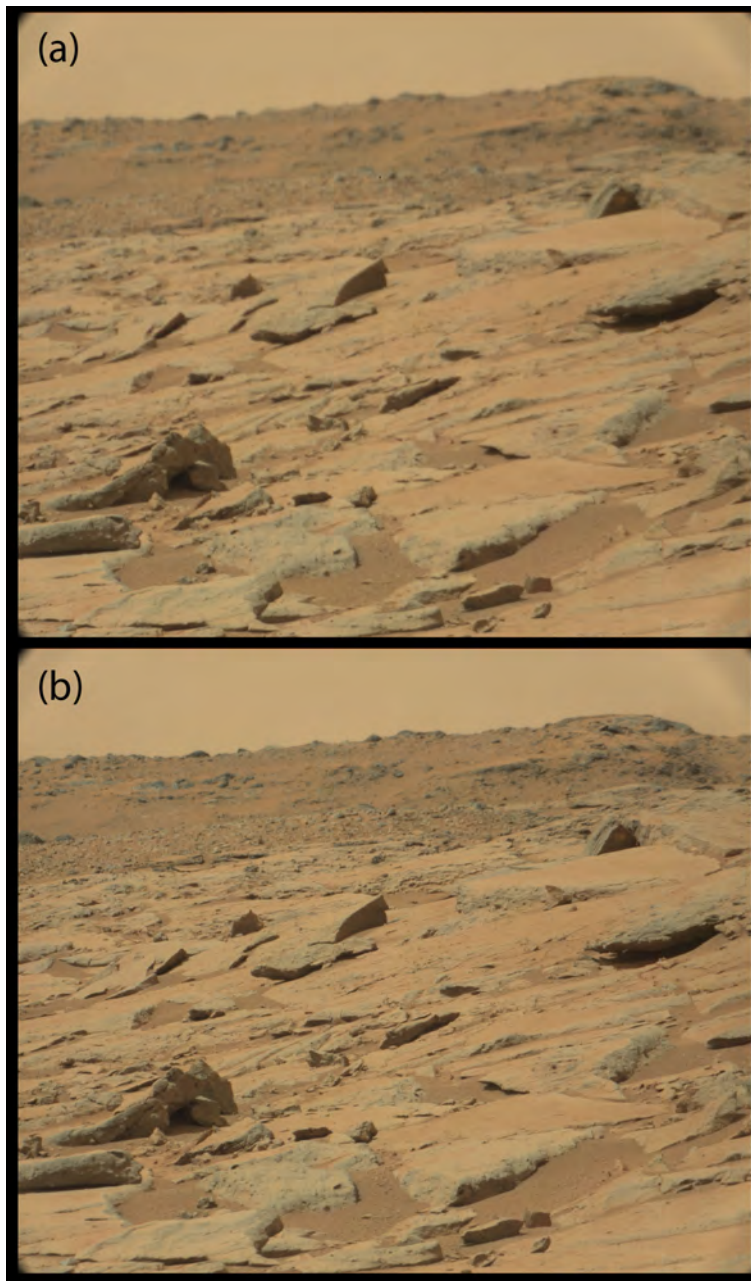


2452

2453 **Figure 27:** Images from the special 1-column x 34-row focus test mosaic acquired with the Mastcams on *Curiosity*
 2454 sol 17. (a) Mosaic of 34 M-34 images acquired in the test, each acquired with 75% overlap relative to the previous
 2455 one; (b) Example of one of the M-100 images from the mosaic with nearer, middle, and far ridges in the same scene;
 2456 (c) Example of another M-100 image from the mosaic with near-field targets at a variety of distances.

2457

2458

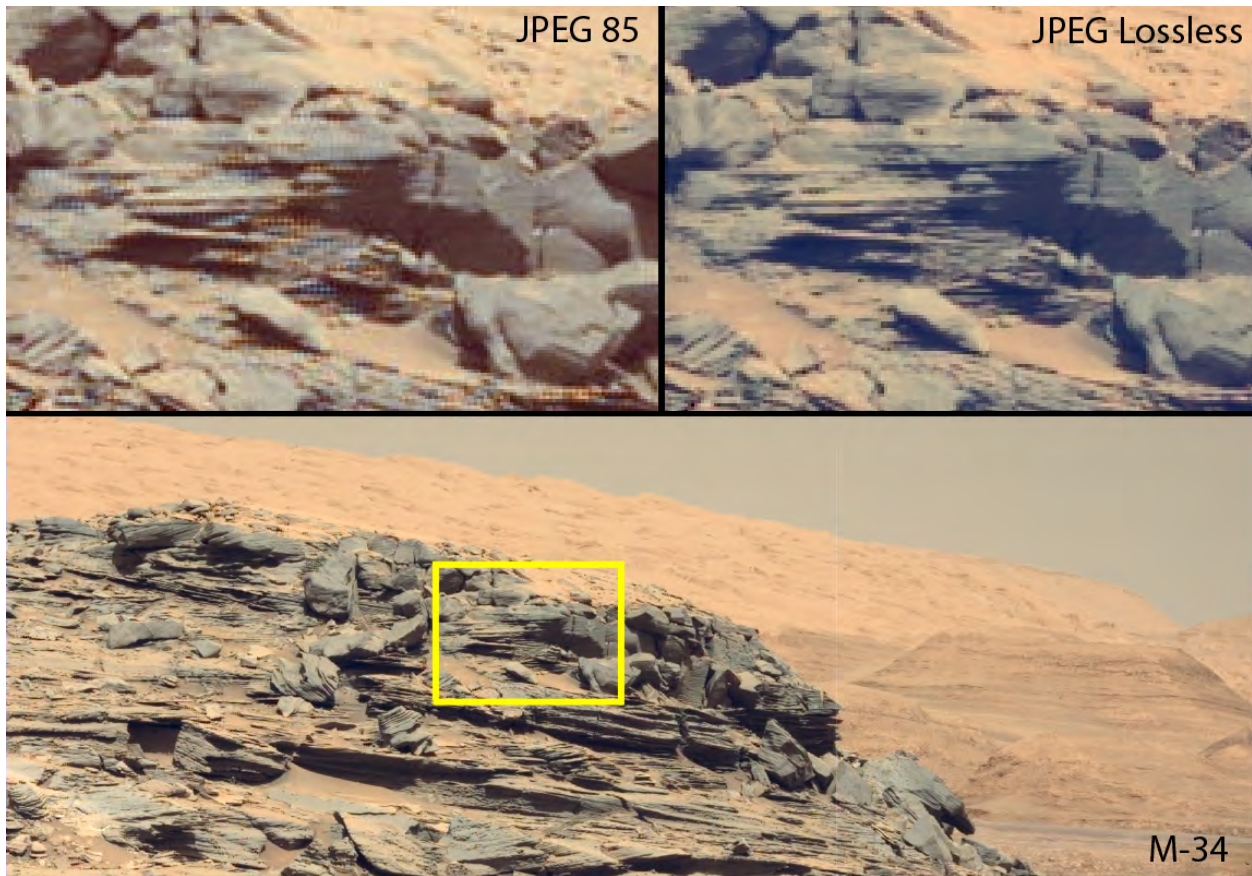


2459

2460 **Figure 28:** Example results from a special 8-image "z-stack" M-100 image test conducted on *Curiosity* sol 193 with
2461 sequence mcam01026. (a) One of the 8 images acquired of the scene, with focus set for the foreground. (b) The
2462 resulting focus-merged z-stack image calculated automatically in Mastcam flight software. Note the dramatic
2463 removal of depth-of-field effects, especially for the far ridge.

2464

2465



2466

2467 **Figure 29.** Mastcam M-34 image of finely-layered outcrop rocks acquired on *Curiosity* sol 1155 and
2468 sequence mcam05219. The upper left inset shows a zoomed-in view of some of the layers in the
2469 originally-downlinked JPEG quality factor 85 image. JPEG artifacts introduce blockiness and color
2470 banding that prevents a detailed assessment of the orientations and spacings of the layers. At upper right
2471 is an example of the same scene after re-downlinking the onboard image losslessly. While the "cost" of
2472 the image was about 2.6 times more downlinked bits than the JPEG 85 version (*e.g.*, Figure 18), the
2473 lossless image does not suffer from JPEG artifacts that interfere with fine-scale geologic interpretation.

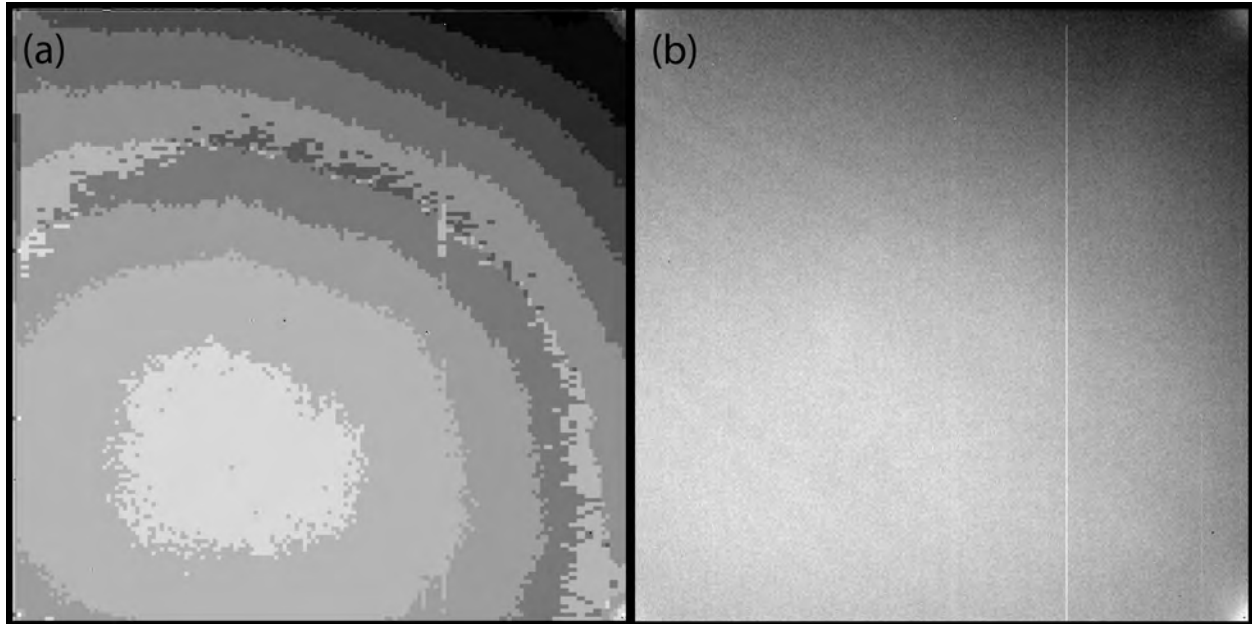
2474

2475

2476

2477

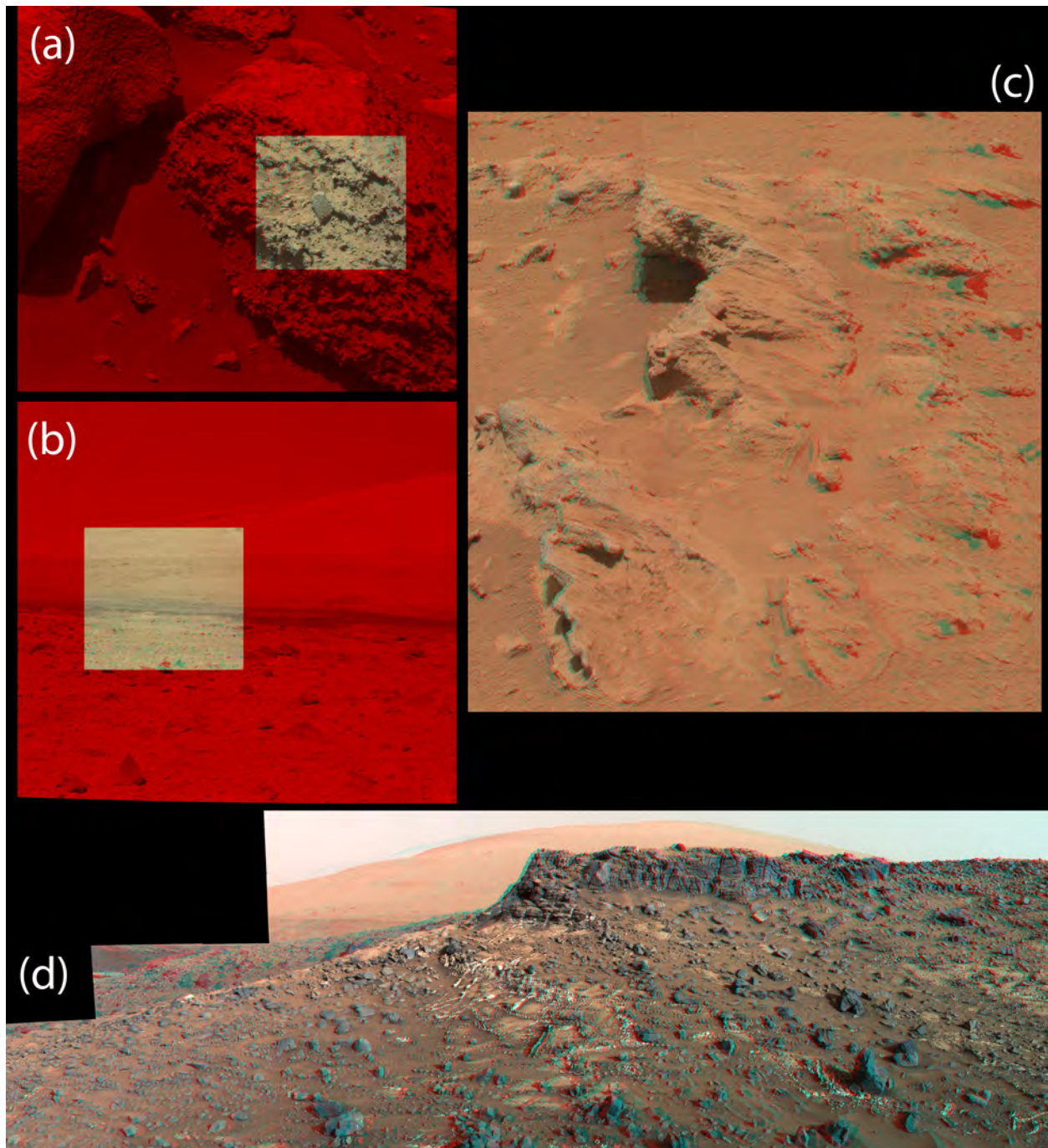
2478



2479

2480 **Figure 30:** Example comparing very heavy Mastcam JPEG compression to lossless compression, for a relatively
2481 uniform scene, from sky images taken on *Curiosity* sol 943 in Mastcam sequence macam04146. (a) Highly-
2482 compressed image of the sky downlinked at JPEG quality factor 35. (b) Losslessly-compressed view of the same
2483 scene, downlinked later at a "cost" of ~15.5 times as many bits as (a). The white vertical line is the result of the
2484 readout of a cosmic ray strike on the detector within some of the top-most rows of the image.

2485



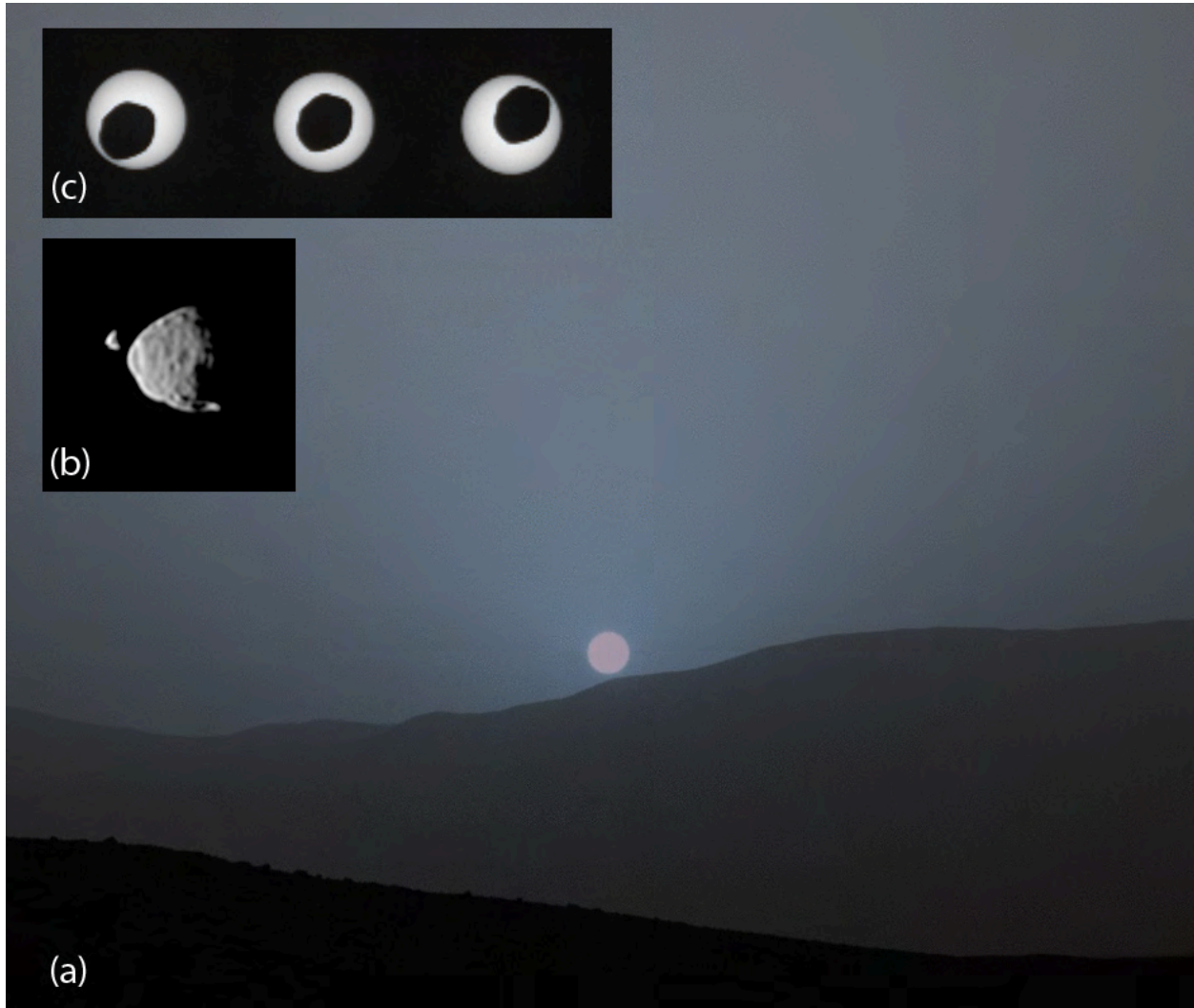
2486

2487 **Figure 31:** Example near-field and far-field stereo image results from Mastcam imaging. (a) Simultaneous stereo
 2488 acquisition of M-34 (red) and M-100 (color anaglyph) from sequence mcam06894, on sol 1408, of the Tumba target
 2489 at a distance of ~2.1 m. Note M-100 placement in the center right of M-34 frame. (b) Same for simultaneous stereo
 2490 acquisition of M-34 and M-100 from sequence mcam01985 on sol 505, including midfield targets at a distance of
 2491 ~20 m to the base of Mount Sharp at a distance of several km. Note M-100 placement in the center left of M-34
 2492 frame. (c) Color red-blue stereo anaglyph of the conglomerate target Hottah acquired on sol 39 using Mastcam
 2493 sequences mcam00177 (M-100 data) and mcam00178 (M-34 data). (d) Color stereo mosaic of the vein-rich ridge
 2494 known as Salsberry Peak, with a second ridge and Mt. Sharp in the background, acquired on sol 938 using Mastcam
 2495 sequence mcam04119. Use standard red-blue stereo glasses to view the 3-dimensional nature of these scenes.

2496

2497

2498



2499

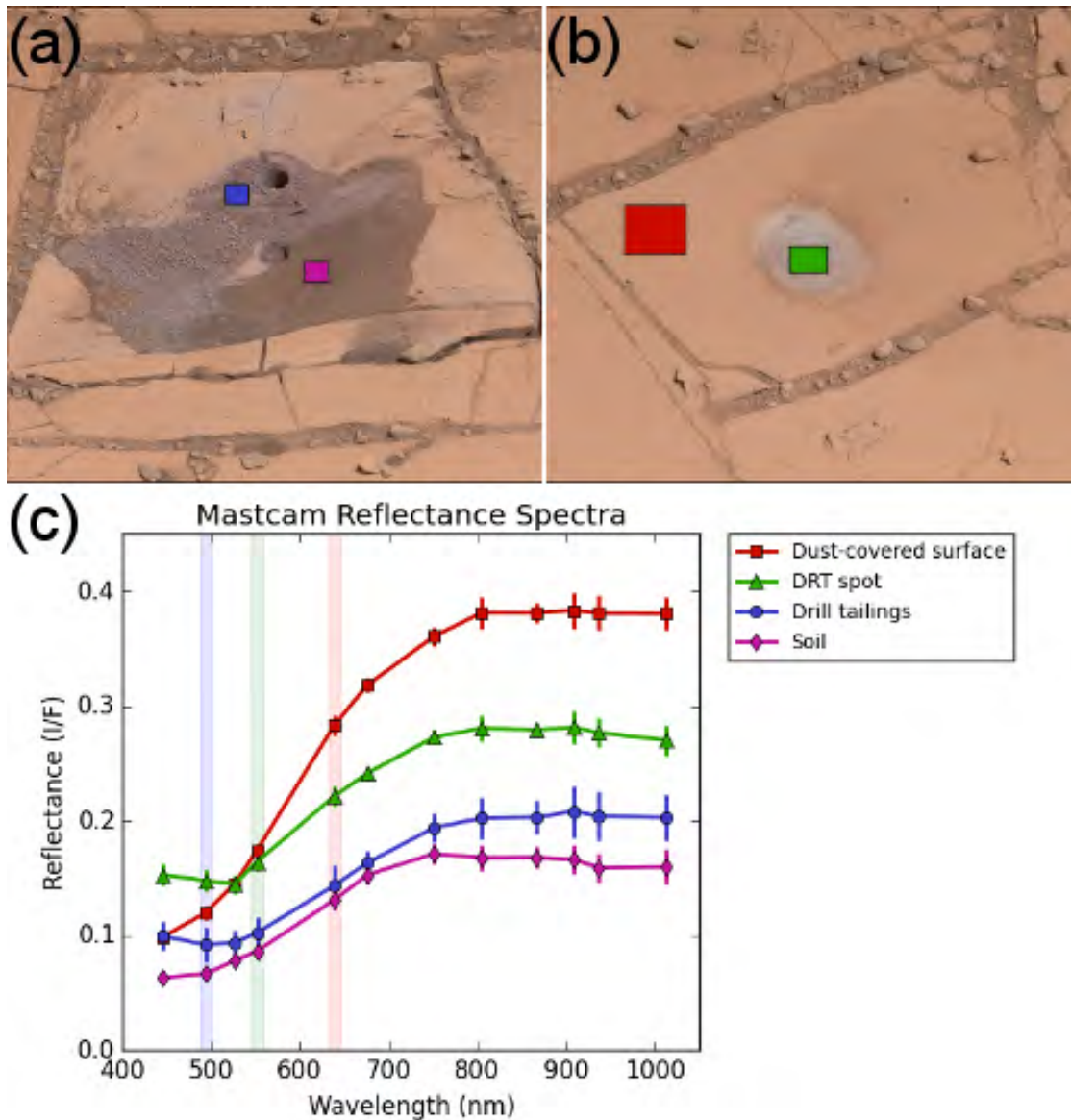
2500 **Figure 32.** Examples of MSL/Mastcam daytime, twilight, and nighttime imaging for atmospheric science and
2501 astronomical observation goals. (a) White-balanced M-34 filter 0 RGB composite image of a Martian sunset,
2502 acquired at twilight on sol 956 (April 15, 2015; NASA, 2015); (b) M-100 Mastcam filter 0 grayscale image of an
2503 occultation of Deimos by Phobos, observed on sol 350 (July 31, 2013; NASA, 2013b); (c) M-100 Mastcam filter 7
2504 time-lapse views of Phobos passing across the solar disk, observed on sol 369 (August 20, 2013; NASA, 2013a).

2505

2506

2507

2508



2509

2510

2511

2512

2513

2514

2515

2516

2517

Figure 33: M-100 Bayer broadband RGB color composites of two pointings from a multispectral sequence acquired on sol 762 at the Confidence Hills drill location, targeting (a) the full and mini drill holes and tailings and (b) a nearby surface brushed by the DRT. The colored boxes are the regions from which the spectra shown in matching colors in the plot (c) are derived. The spectra are plotted as the mean I/F value as a function of filter band center wavelength, with bars showing the standard deviation of the pixels within each ROI. Spectra from the two cameras have been scaled together and averaged at overlapping filters. Colored stripes show the positions of the broadband Bayer values.